PHASE TRANSFORMATIONS IN RUBIDIUM NITRATE AND ITS

SOLID SOLUTIONS WITH CESIUM AND POTASSIUM NITRATES

A THESIS

submitted to the

INDIAN INSTITUTE OF TECHNOLOGY, KANPUR

in partial fulfilment of the requirements

for the degree of

DOCTOR OF PHILOSOPHY

by

PREM PRAKASH SALHOTRA

DEPARTMENT OF PHYSICS

INDIAN INSTITUTE OF TECHNOLOGY, KANPUR, INDIA

NOVEMBER, 1967

Thesis
541.363
Sa 32

Certified that the work presented in this thesis has been carried out by Mr. P.P. Salhotra under our joint supervision and has not been submitted elsewhere for a degree.

P. Venkateswarlu
Professor
Department of Physics
Indian Institute of Technology
Kanpur, INDIA

E.C. Subbarao
Professor
Department of Metallurgical
                Engg.
Indian Institute of Technology
Kanpur, INDIA

ACKNOWLEDGEMENT

TABLE OF CONTENTS

TABLE OF CONTENTS (Continued)

TABLE OF CONTENTS (Continued)

. . . .

LIST OF TABLES

LIST OF TABLES (Continued)

LIST OF TABLES (Continued)

LIST OF TABLES (Continued)

LIST OF FIGURES

LIST OF FIGURES (Continued)

LIST OF FIGURES (Continued)

LIST OF FIGURES (Continued)

PREFACE

Rubidium Nitrate ($RbNO_3$) exists in four crystalline phases as follows:

$$IV \xrightarrow{164^{\circ}C} III \xrightarrow{219^{\circ}C} II \xrightarrow{285^{\circ}C} I$$

| Trigonal | Cubic | Hexagonal or Tetragonal | Cubic |

Phase transformations in Rubidium Nitrate and its solid solutions with Cesium Nitrate and Potassium Nitrate are the subject of this thesis

The thesis contains five chapters and seven appendices.

Chapter 1 reviews the relevant literature

Statement of the problem is given in Chapter 2.

The experimental techniques employed in the present investigation are: (ac) electrical conductivity, differential thermal analysis (DTA), linear and axial thermal expansion, X-ray diffraction, and infrared absorption These are described in Chapter 3

The results of the investigation are compiled in Chapter 4. The transformation temperatures, in $RbNO_3$ and its solid solutions, are marked by discontinuous changes in electrical conductivity and lattice parameters Temperature hysteresis, in

the transformation regions, is observed by all the present

experiments. A systematic study of the phases IV, III, II and I

of $RbNO_3$ is presented. Phase I, which was not clearly detected

before by electrical methods, is detected unambiguously by

electrical conductivity, dilatometric, and infrared absorption

studies. It was also confirmed by X-ray diffraction and differen-

tial thermal analysis. The following data are tabulated.

1. Conductivity experiment: activation energy of conduction in

different phases of $RbNO_3$, 2. Differential Thermal Analysis:

thermal activation energy, and heats of transformations,

3. Dilatometric experiment: percent changes in length at the

phase changes and coefficients of linear thermal expansion in

the stable phases, 4. X-ray studies: Coefficients of thermal

expansion in stable phases, and percent volume and axial changes

at the phase transitions. Potassium Nitrate is observed to go

into solid solutions in Rubidium Nitrate to an extent of $\sim$ 5 mole

percent and Cesium Nitrate to an extent of $\sim$ 25 mole percent at

room temperature. Partial substitution of Cesium ion (radii of

Cs^+ and Rb^+ ions are $1.68A^\circ$ and $1.48A^\circ$ respectively) for

Rubidium ion in $RbNO_3$ shifts the transition temperature III $\rightleftharpoons$ II

markedly to higher temperatures while substitution of Potassium

ion (radius of K^+ is $1.33 A^0$) depresses it, more during cooling than during heating. The transition temperatures IV $\rightleftharpoons$ III and II $\rightleftharpoons$ I are not much affected. The (composition-temperature) phase-diagram of the solid solution series $K_xRb_{1-x}NO_3$ and $Cs_xRb_{1-x}NO_3$ on the Rubidium rich side, are plotted from the conductivity data. These diagrams compare well with those of Kentzicer. The results of X-ray diffraction studies—lattice parameters as a function of temperature, detection of phase changes, and co-existence of phases III and II in the transition region III $\rightleftharpoons$ II,—are described. Infra-red absorption spectra of $RbNO_3$ in the temperature range, room temperature to near its melting point, is studied in the frequency range $700cm^{-1}$ to $5000cm^{-1}$. The spectra are presented in the range 700 to $1200cm^{-1}$, as this covers the fundamental frequencies of the NO_3^- ion. While no spectrum was observed in phase II, the spectra observed in all other phases were essentially due to the NO_3 groups. Infra-red spectra of solid solutions at room temperature are also presented.

The results described above are synthesized in Chapter 5. The experimental results of Chapter 4, taken together with the available data in the literature, make it possible to suggest an

atomistic approach for understanding the phase transformations in RbNO$_3$. Infra-red absorption spectra in different phases of RbNO$_3$ are discussed in terms of the disordering of NO$_3$ groups. The absence of spectra in phase II has been associated with the ordering of NO$_3$ groups. The increase in electrical conductivity at IV$\rightarrow$III transformation is associated partly with the orientational disordering of the NO$_3^-$ ions and partly with the positional randomization of Rb$^+$ ions. The decrease in conductivity at III$\rightarrow$II transition has been interpreted as due to the ordering of the NO$_3^-$ ions. The gradual disordering of the NO$_3^-$ ions at II$\rightarrow$I transition has been considered responsible for this gradual order-disorder transformation. Orientational effects are proposed to explain the difference in results, obtained from dilatometric measurement of bulk expansion and X-ray measurement of axial expansion, after III$\rightarrow$II transformation. The shifting of transformation temperatures, by the partial ionic substitutions in solid solutions, is explained on the basis of thermal activation energy values obtained from DTA and the similarity of phases IV and III of RbNO$_3$ with II and I of CsNO$_3$ and phase II of RbNO$_3$ with I of KNO$_3$. Thermal hysteresis is explained on the basis of co-existence of phases in the transformation regions. Phase II of RbNO$_3$ is found to have a hexagonal symmetry rather than tetra-

gonal. A possible structure for phase II is proposed and the cation positions are indicated. The lattice relationships are proposed for the different phases of $RbNO_3$.

Appendices A, B, and C give the derivation of the expressions used for the calculations of heats of transition, thermal energies of activation in DTA experiment and magnification in the dilatometric experiment respectively. Appendices D, E, F and G list the data obtained from electrical conductivity measurements, DTA, dilatometric and X-ray studies respectively.

INTRODUCTION

Alkali metal nitrates except $LiNO_3$ exhibit polymorphic transformations. Phase transformations in alkali nitrates have been reviewed by Cleaver et al[1,2] and McLaren[3]. This thesis describes the phase transformations in Rubidium Nitrate and its solid solutions with Cesium Nitrate and Potassium Nitrate.

1.1 Crystal Growth

Needle shaped crystals of $RbNO_3$ with triangular cross-section were grown from an aqueous solution at room temperature by Brown and McLaren[4]. Kennedy[5] grew crystals of $RbNO_3$ from the melt.

$RbNO_3$ was purified by zone-melting method by Sue et al[6].

1.2 Phase Transformations

X-ray diffraction patterns of $RbNO_3$ do not show any structural changes between liquid nitrogen temperature and room temperature[7]. Above room temperature $RbNO_3$ has the following four crystalline forms[8,9].

$$IV \xrightarrow{164°C} III \xrightarrow{219°C} II \xrightarrow{291°C} I$$

Trigonal   Cubic   hexagonal   Cubic
(or tetragonal)
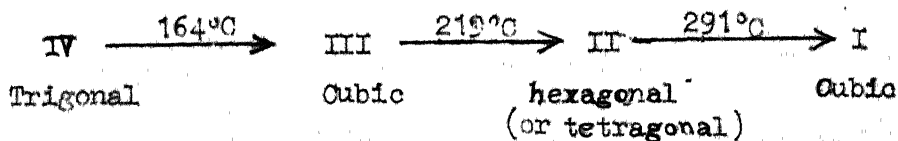
Form IV crystallizes from aqueous solution at room temperature as needles with triangular cross section. X-ray photographs[4] show that IV is trigonal with a = 10.48 A° and c = 7.45A°. The needle axis corresponds to the c – axis and the sides of the triangular cross-section are parallel to the a – axis. The space group is $P3_1 12$ or $P3_2 12$ (i.e. D_3^4 or D_3^6).

Form III is cubic[4,10] with a = 4.36 A° and Z = 1. Korhonen[11] on the basis of x-ray powder photographs at 190°C. suggests that the true unit cell of $RbNO_3$ is cubic with a = 8.74A°. Korhonen[11] gave the space group as T_h^6 – Pa3 while Finbak and Hassel[10] suggested O_h^1 – Pm3m. The atomic positions are : eight Rubidium ions at cell corners, cell center, cell face centers and cell edge centers; eight Nitrogen ions on cell body diagonals at uuu with u = 0.285, and twenty-four oxygen ions at xyz etc with x = y = 0.278 and z = 0.399 (fig 1.1). NO_3^- was assumed to be symmetrical with N-O = 1.22 A°. Finbak and Hassel[10] suggested that NO_3^- ions are in free rotation in form III, whereas Korhonen[11] believes that NO_3^- ion disorder is similar to that suggested by Fischmeister[12] in KNO_3.
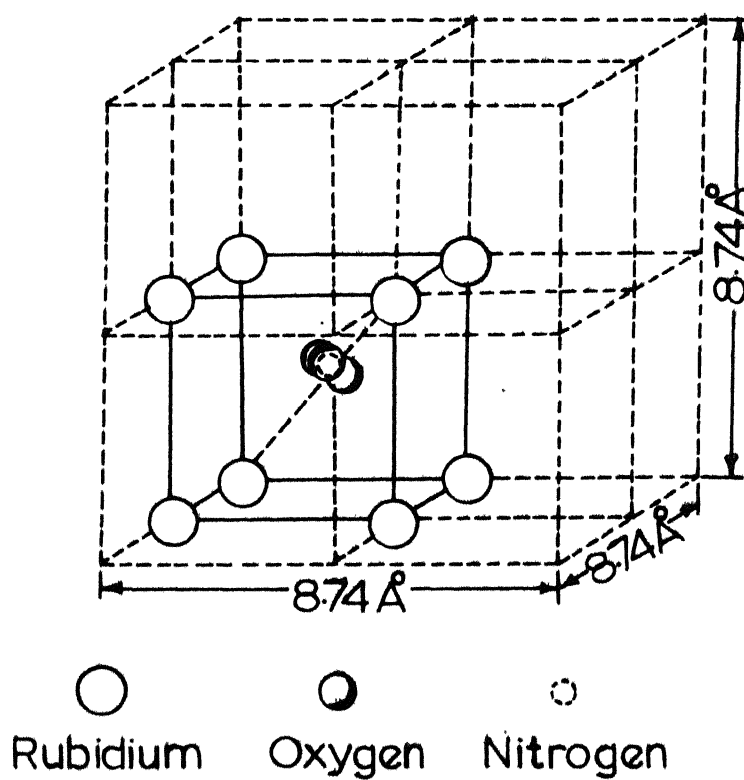
FIG. 1.1 Unit cell of form III of Rubidium Nitrate with
atomic positions in 1/8 th of the unit cell
(constructed after ref. 11).

X-ray photographs of single crystals heated through IV → III transformation, show that the trigonal $[00.1]$ of IV transforms to cubic triad $[111]$ of III[4,13,14] with the trigonal $[10.1]$ direction becoming the cubic edge $[100]$[4]. The structural relationship[4] between phases IV and III is shown in fig. 1.2.

After III → IV transition, any one of the four equivalent cube diagonals can become the trigonal c – axis. Therefore in the transformation cycle IV → III → IV, the crystals may come back to form IV in any one of the four orientations. For a needle crystal of triangular cross-section, it is possible to calculate[4] the angle between the needle axis and the crystallographic c – axis corresponding to each of the four possible orientations. These angles are 0°, 70.5°, 55° and 55° (two cube diagonals are indistinguishable). All these orientations were observed by Brown and McLaren[4] under the microscope.

On the basis of powder photographs Brown and McLaren[4] found several possible cells for form II : the most probable being tetragonal with a = 6.19A°, c = 8.74A° and Z = 4. Finbak et al[13] gave the unit cell of II as hexagonal with a = 5.48A°, c → 10.71 A°.
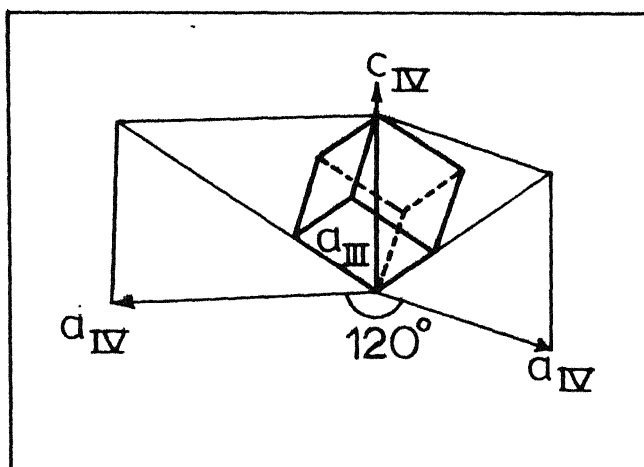
Fig. 1.2 Structural relationship between the unit cells of forms IV and III of Rubidium Nitrate (ref. 4).
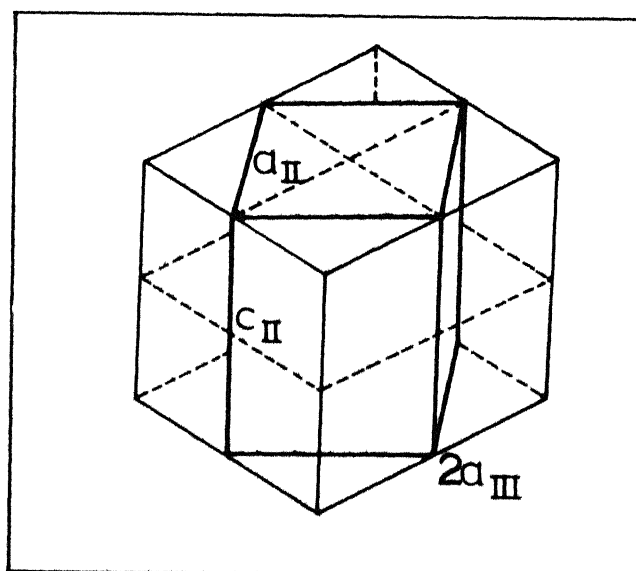
Fig. 1.3 Structural relationship between the unit cells of forms III and II of Rubidium Nitrate (ref. 4).

At III $\longrightarrow$ II transformation the crystals are observed to crack and bend and become anisotropic. Distortion of crystals increases on cooling. Due to this distortion Brown and McLaren could not study these (and II $\rightleftharpoons$ I) transformations on single crystals with x-rays. This transformation was therefore studied by powder diffractometry[4].

Although there are several possible unit cells for II, the dimensions of unit cell of III and the most probable unit cell of II show a simple relation (fig. 1.3), namely

$$\sqrt{2} \ a_{III} = 6.16 \ A°, \ a_{II} = 6.19 A°$$

$$2 \ a_{III} = 8.72 \ A°, \ c_{II} = 8.74 A°$$

This suggests that the true unit cell of II is tetragonal[4] (with a = 6.19 A°, and c = 8.74 A°). Therefore, at III $\longrightarrow$ II transformation the crystal has a choice of three possible orientations, corresponding to three mutually perpendicular directions for c_{II} - axis. The choice of orientations may be responsible for the fragmentation which occurs at this transformation[4].

X-ray powder photographs show that phase I has NaCl structure[5]. Brown and McLaren[4] on the basis of x-ray diffractometer pattern show that form I is cubic with a = 7.32 A°, Z = 4. The II $\longrightarrow$ I transformation was observed under the microscope, the crystals becoming isotropic without any extra distortion or fragmentation being evident[4].

However, no simple relation between the cell

dimensions of II and I was found. Based on the gradual changes

in x-ray reflections at II ⇌ I transformation, Kennedy[5] has

suggested an order-disorder transition in the anion arrangement

with ~~no change in the Rb⁺ positions~~. Since the temperature

of this transformation is only 20°c below the melting point,

it is possible that crystals are sufficiently plastic to withstand

a structural change in which a_{II} and c_{II} expand and contract

respectively, to become equal to $a_I^{(4)}$. Kennedy[5] has reported

that the crystal decomposes during long x-ray exposures and

therefore moving film methods could not be applied to verify the

structure of form I.

1.3 Electrical Conductance

Brown and McLaren[4] have measured the electrical

conductance of compressed powder pellets of $RbNO_3$ as a function

of temperature. DC methods were employed for temperatures upto

about 250°c and a frequency of 1 KC/S for measurements above

250°c. The results of these measurements, shown in fig 1.4,

indicate the following : (i) at IV → III transformation conductance

increases by a factor of 100. A corresponding decrease occurs

during the reverse transformation. This behaviour is repeatable.
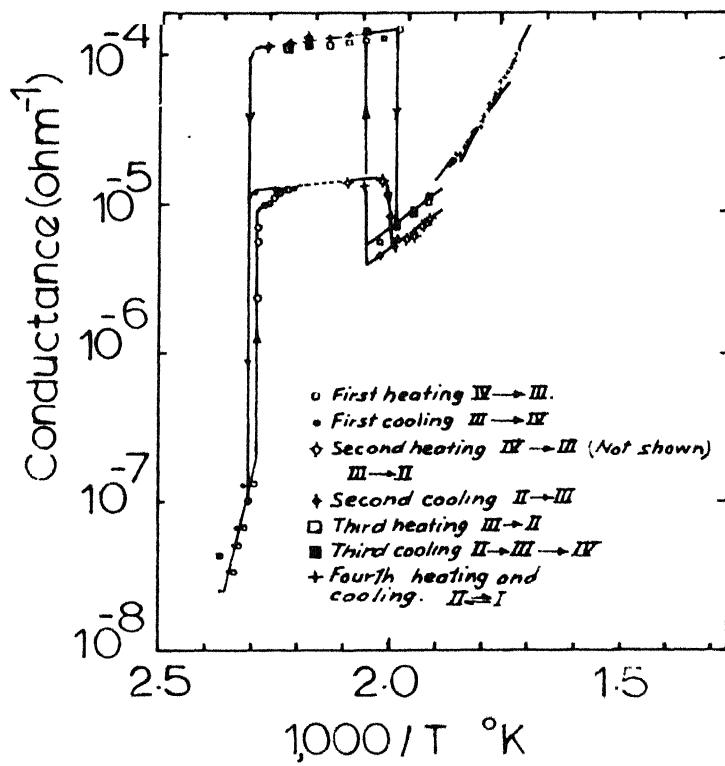
Fig. 1.4 The electrical conductance of Rubidium
Nitrate as a function of temperature
(ref. 4).
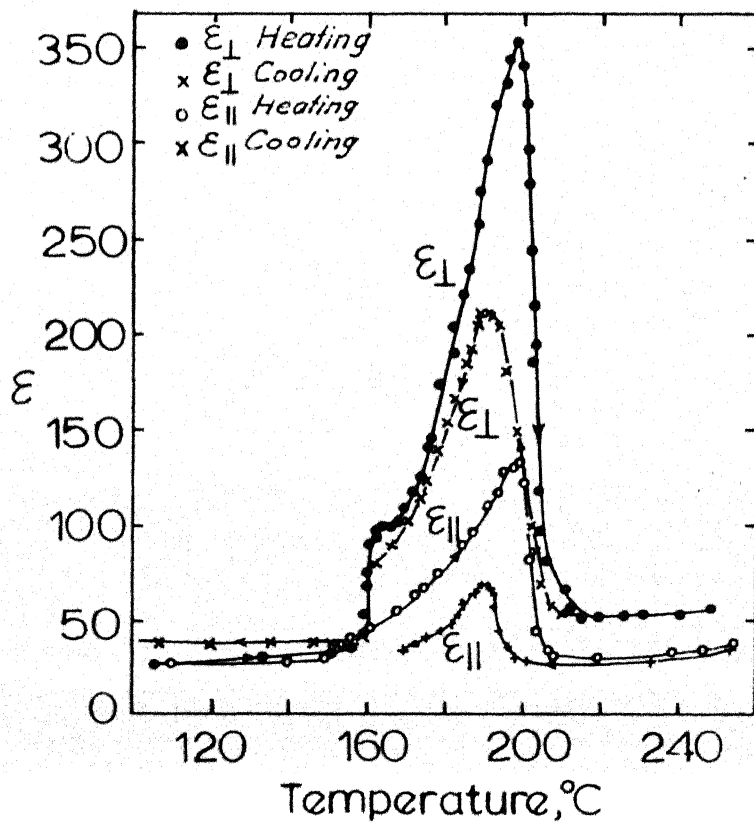
Fig. 1.5 Temperature dependence of $\epsilon_{\parallel}$ and
$\epsilon_{\perp}$ of Rubidium Nitrate (rising and
falling temperature) (ref. 26).

(ii) The first III $\longrightarrow$ II transformation leads to a decrease

in conductance by a factor of 3 whereas an increase by a

factor of 30 takes place at the reverse transformation. On

repeating the III $\rightleftharpoons$ II cycle the conductance changes by a

factor of 30 both on heating and cooling. (iii) On further

cooling, the conductance decreases by a factor of 1000 at

III $\longrightarrow$ IV transition to its original value. On reheating the

sample, the conductance increases by a factor of 1000 at

IV $\longrightarrow$ III transition and decreases by a factor of 30 at the

III $\longrightarrow$ II transformation. This behaviour $\left[\text{(i) to (iii)}\right]$

was confirmed on a second sample[4], and (iv)   the II $\rightleftharpoons$ I

transition involves only a change of slope in the graph of log

(conductance) against reciprocal absolute temperature.

The conductance changes at II $\rightleftharpoons$ I transformations

were interpreted by Brown and McLaren[4] as an evidence that these

transformations do not involve any sudden change in positional

randomization of the ions.

It is evident from fig 1.4 that when the transformation

involves an increase in crystallographic symmetry, the electrical

conductance increases, and vice versa[4]. This has also been

observed in KNO_3, $TlNO_3$, $CsNO_3$ and NH_4NO_3. Brown and McLaren[15]

have shown by proton magnetic resonance that the increase in

conductance at II$\longrightarrow$I transformation in NH_4NO_3, is due to

positional randomization of the NH_4^+ ions. There is evidence

that a similar situation exists in $TlNO_3$[16]. It was, therefore,

suggested by Brown and McLaren[4] that the increase in

conductance at IV$\longrightarrow$III transformation is due to some positional

randomization of the Rb$^+$ ions, and that the decrease at III$\longrightarrow$II

transformation corresponds to an ordering process.

After the first II$\longrightarrow$III transition a permanent

increase in conductance of phase III over its original value

was noted[4] (fig. 1.4). This remained unexplained and is now

explained in Chapter 5.

After IV$\longrightarrow$III transformation, Kennedy[17] has

observed changes in x-ray reflections of phase III on annealing

it for more than 20 hours. These changes are parallelled by

changes of 20 to 40% in ionic conductivity.

The transport properties of the fused alkali

nitrates have been studied by a number of investigators[18-23]

using radio tracers. The results pertinent to this study are

summarized in table 1.1.

Table 1.1   Transport Properties in Fused Alkali Nitrates.

Species	Diffusion Coefficient, $DX10^5 (cm^2/sec)$	Ionic mobility, $ux10^4 (cm^2/v.sec)$	Transport Number
NO_3^- in KNO_3		2.45 ± 0.1 [22]	
NO_3^- in $RbNO_3$		2.38 ± 0.08 [22]	
NO_3^- in $CsNO$		2.38 ± 0.06 [22]	
K^+ in $RbNO_3$	2.14 ± 0.12 [22] 2.52 ± 0.10 [23]	2.33 ± 0.05 [22]	
Rb^+ in $RbNO_3$	2.24 ± 0.05 [22] 2.51 ± 0.08 [23]	2.26 ± 0.036 [22]	0.56 ± 0.03 [19] ; 0.38 [20] ; 0.59 ± 0.04 [21]
Cs^+ in $RbNO_3$	$2.29 + 0.07$ [22]	2.24 ± 0.036 [22]	
K^+ in KNO_3	3.21 ± 0.20 [22]	3.12 ± 0.05 [22]	0.59 ± 0.02 [21]
Cs^+ in $CsNO_3$	2.29 ± 0.07 [22]	2.30 ± 0.025 [22]	$0.50 + 0.04$ [19]; 0.40 [20] ; 0.59 ± 0.07 [21]

22   Values of u and D recorded here are obtained from the plots of u or D vs cationic radii for alkali nitrates. These values were measured at 450°C.

The logaritham of viscosity (η) of molten alkali

nitrates was found to vary linearly with the reciprocal of absolute

temperature[24]. For these materials, $\sigma^n \eta = $ constant where σ

is the electrical conductivity and n represents the ratio of activation

energies for viscous flow and electrical conduction.

1.4 Dielectric Properties

Dantsiger [25, 26] and Fesenko [26] have measured

the dielectric constants parallel ($\epsilon_{\parallel}$) and perpendicular ($\epsilon_{\perp}$)

to the trigonal axis for $RbNO_3$ at a frequency of IMc/s as a function

of temperature. Both the dielectric constants have an anomalous

behaviour, particularly $\epsilon_{\perp}$ (fig 1.5, p.8). It is evident from

fig 1.5 that there is a discontinuity in $\epsilon_{\perp}$ at IV $\rightarrow$ III

transition and a sharp peak in $\epsilon_{\perp}$ at the III $\rightarrow$ II transition.

The changes in $\epsilon_{\perp}$ were compared with those in

conductivity at the phase transitions as shown below.

Transition	Dielectric constant $\epsilon_{\perp}$	Electrical conductivity
IV $\rightarrow$ III	Increases by a factor of 3	Increases by a factor of 100
III $\rightarrow$ II	Increases by a factor of 10	Decreases by a factor of 30

The above comparative study and the fact that

above III $\rightarrow$ II transition $\epsilon_{\perp}$ falls nearly to its initial

value (fig 1.5) show that the behaviour of $\epsilon_{\perp}$ does not follow

that of conductivity.

On the basis of crystallographic criterion for

spontaneous polarisation Zhelndev and Sonin [27] (and on the

dielectric and dilatometric measurements, Dantsiger [25]) proposed

$RbNO_3$ as a probable ferroelectric. However, the space group

symmetry of $RbNO_3$ crystals was found not to obey the more precise crystal physical criterion[28, 29]. Protsenko et al[30] were also unable to find any ferroelectric properties in single crystals of $RbNO_3$. On the basis of the study of the dielectric properties of (i) crystals and (ii) cooled melt of $RbNO_3$ Dantsiger and Fesenko[26, 31] have found and confirmed the antiferroelectric properties for phases II and IV. In comparison with the ferroelectric properties of KNO_3[32] Dantsiger and Fesenko[26] associate the antiferroelectric behaviour of phase II in $RbNO_3$ with rotation (about the principal axis) and antiparallel displacement of NO_3 groups within any one domain.

Finbak and Hassel[33] report that phase IV of $RbNO_3$ is pyroelectric.

1 5 Thermal Expansion

Using a quartz dilatometer Dantsiger[25,26] and Fesenko[26] have measured the coefficients of thermal expansion for the directions parallel and perpendicular to the three fold axis ($\ell_{||}$ and $\ell_{\perp}$) of $RbNO_3$. Fig. 1.6 shows $\frac{\ell - \ell_0}{\ell_0}$ for these two directions as a function of temperature (ℓ_0 is the length at $20^{\circ}c$). It is evident that the coefficients for $\ell_{||}$ and $\ell_{\perp}$ are positive for phase IV. On the other hand, the coefficients are negative for phase III, especially for $\ell_{\perp}$ at IV $\longrightarrow$ III, and III $\longrightarrow$ II transition points.
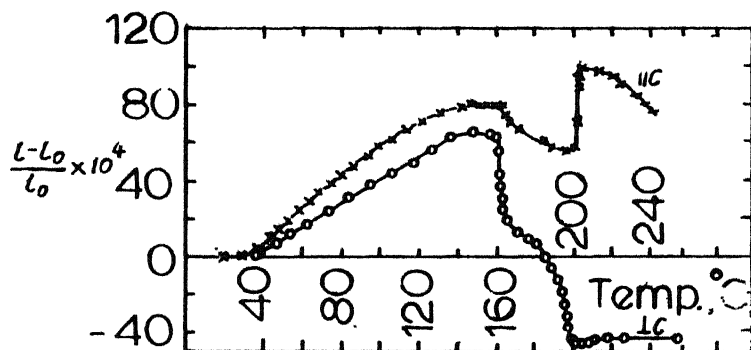
Fig. 1.6 Thermal expansion as a function of
temperature for two directions of Rubidium Nitrate (ref. 26).
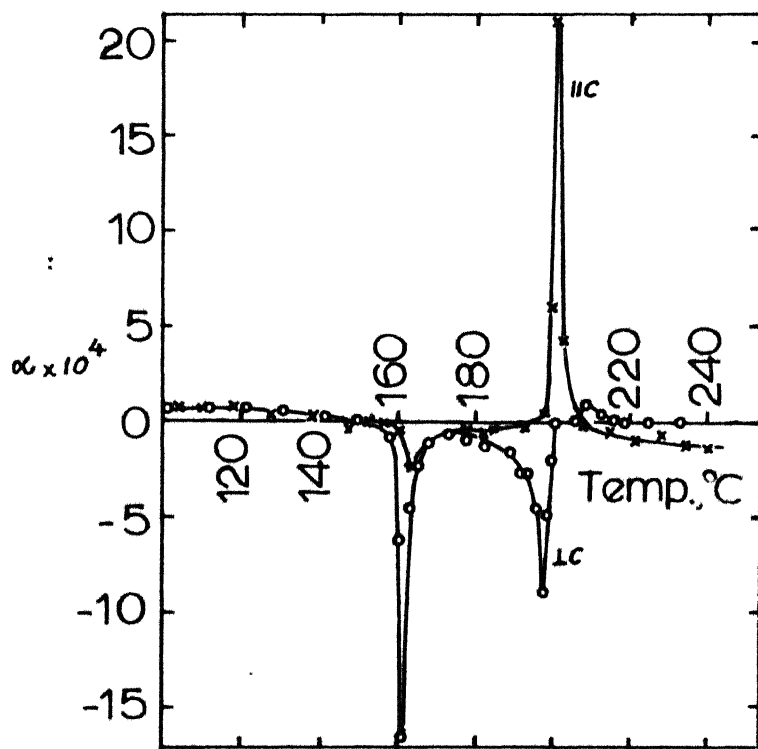
Fig. 1.7 Coefficients of thermal expansion of
Rubidium Nitrate as functions of temperature (ref. 26).

There is a stepwise expansion along $\ell_{||}$ at III $\rightarrow$ II transition.

Fig. 1.7 shows the coefficients $\alpha_{||}$ and $\alpha_{\perp}$ as a function of temperature. The transition points stand out as sharp peaks.

Kennedy[17] has reported, on the basis of single crystal x-ray diffractometry, that the coefficient of thermal expansion for phase III is positive (Table 1.2). Table 1.2 lists thermal data for stable phases and table 1.3 gives the volume changes at the phase transitions of $RbNO_3$. The density and molar volume of fused alkali nitrates including $RbNO_3$ were determined by Protsenko et al[18]. The density was found to vary linearly with temperature.

Recently Rapoport[34] has investigated IV $\rightleftharpoons$ III transformation in $RbNO_3$ upto 40 Kilobars (Kb). DTA signals were obtained with no hysteresis upon cooling. Bridgman[35] found new polymorphs in $RbNO_3$ above 17 kb. Some similarities in the phase diagrams of $RbNO_3$, $CsNO_3$ and $TlNO_3$ were pointed out in the early work of Bridgman[36]. Recently Rapoport and Kennedy[37] have suggested that the phase diagrams of KNO_3 above 15 kb, $RbNO_3$ above 2 kb and $CsNO_3$ are qualitatively similar and that the corresponding phases are isostructural. The isoelectronic solids

TABLE 1.2 Thermal data for PbNO₃ (ref. 2)

Crystal structure	Temperature range(°C)	Molar volume (c.c.)	Density(gm/c.c) observed[38]	Density(gm/c.c) calculated[4]	Volume thermal expansion coeff. $\gamma \times 10^6 (°C)^{-1}$	$\alpha_c \times 10^6$ $(°C)^{-1}$	$\alpha_a \times 10^6$ $(°C)^{-1}$	Specific heat c_p ** (cal/g)[44]
Trigonal	20 to 162	47.2	3.11 (room temp.)	3.11 (room temp.)	210	101.5*	97.1*	$0.1567+2.76\times10^{-4}t\pm$ 0.0009(50-160°C)
Cubic	162 to 220	49.6	–	2.96 (at 180°C)	340		85.0*	$0.1864+4.73\times10^{-4}t\pm$ 0.0022(160-220°C)
Hexa-gonal	220 to 281	56.9	–	2.92 (at 220°C)	–	–	–	$0.2445+1.12\times10^{-4}t\pm$ 0.001(220-281°C)
Cubic	281 to 310	59.0	–	2.50 (at 295°C)	–	–	–	0.2650
Melt	312 to above	59.33***	–	–	405³	–	–	$0.2143+1.37\times10^{-5}t\pm$ 0.0016(310-350°C)

*** Molar volume before melting is 59.47 c.c and after melting is 59.33 c.c.[39]

** In the last column the temperature range ('t) is given in brackets. Phase I exists over such a narrow range that there is no significant change from the value given.

* These expansion coefficients were obtained from an X-ray study of single crystals.[17]

TABLE 1.3 Thermodynamic Parameters of Phase transitions of RbNO$_3$ [44,45,47].

Transition	ΔV c.c/mole		Heat of transition (cal/mole)			Entropy of transition (ΔS) (cal/mole deg)		ΔS=R ln N cal/mole deg. **
	ref. 2	ref.47	ref.45	ref.44	ref.47	ref. 44	ref. 45	ref. 49
IV→III	(+2.4)*	+2.52	932±1.5%	923±1.5%	950±15%	2.15±1.5%	2.11	2.11 2.18(3)
III→II	(+5.0)*	+6.00	767±2.0%	774±1.5%	650±15%	1.53±2.0%	1.57	2.11+1.57 = 3.68 3.56(6)
II→I	(+0.5)*	+3.12	230±6.5%		300±15%	0.42±6.5%	-	3.68+0.42 = 4.10 4.13(8)
I→liquid	-(6.14)(35)@ -(0.36)(42)		1109±1.5%			1.90±1.5%		-	-

* Dilatometric values for RbNO$_3$ show discrepancies (cf refs 2 and 13)

** ΔS, at the phase transitions, is regarded to configurational entropy. It is assumed that configurational entropy of phase IV is zero. These values of ΔS in this column are values of entropy of phases IV, III, II and I. A value close to these with a definite value of N, written in the bracket, is also recorded later in ref. 42.

@ Value of ΔV observed in reference 35, at I→liquid was improved later in ref. 42.

$RbNO_3$ and $SrCO_3$ allow interesting comparison of corresponding crystal structures and phase diagrams[34].

The melting points and the volumes of fusion of alkali nitrates including $RbNO_3$ were determined, at pressures upto 10 kb, by Owens[43]. There is a striking similarity in the melting curves of $CsNO_3$, $RbNO_3$ above 2 kb and KNO_3 (phase VI)[35] which again suggests that the corresponding solid phases are isostructural

1.6 Specific Heat, Heats of Transitions, Entropy and Free-Energy.

Mustajoki[44] has determined the specific heats of various phases of $RbNO_3$ with a Moser calorimeter using both heating and cooling curves. These are tabulated in table 1.2

Heats of transition and entropy of transition as determined by Mustajoki[44] and Arell and Varteva[45] are summarized in table 1.3.

Gordon and Campbell[46] have studied the crystalline transitions and fusion of alkali nitrates including $RbNO_3$ by differential thermal analysis (DTA). Rao and Rao[47] have also recently examined the phase transformations of alkali nitrates by DTA. The values of heats of transition and of volume changes, from the DTA study[47] seem to be in reasonable agreement with the calorimetric values[44,45] except that the changes in volume at II $\longrightarrow$ I

Vasil'ev and Vasil'eva[48] have expressed the available data on entropy of the crystal lattice of nitrates by the relation

$$\Delta S_{latt} = \alpha \sum n$$

where n is the number of ions forming the compounds and α is a constant. The values of entropies of transition, in the nitrates of Na^+, K^+, Rb^+, Cs^+, Ag^+, and Tl^+ have been considered in terms of the orientational disorder of NO_3^- ion[49]. The data on these nitrates have been discussed in terms of the structural relations for the transitions.

Free energy of the lattice is calculated by the relation

$$\Delta F_{latt} = U - T\Delta S_{latt.}$$

where U is the lattice energy.

Lattice energies and free energies of $RbNO_3$ were calculated by Ladd and Lee[50].

1.7 Infrared Absorption

Infrared absorption spectra of metal nitrates including $RbNO_3$, in the range 5000 cm^{-1} to 700 cm^{-1} at room temperature has been tabulated by Vranty[51].

Infrared absorption spectra of single crystals of inorganic nitrates including $RbNO_3$ between room temperature and liquid helium temperature were obtained by Schroeder, Weir and Lippincott[7]. Diffuse absorption between 1400cm^{-1} and 700 cm^{-1}

was observed at room temperature. At liquid helium temperature, this was resolved into a large number of bands which are not attributable to fundamental frequencies (ν_1, ν_2, ν_3, and ν_4) or combinations of fundamental frequencies of the NO_3^- ion. Almost all of these bands were interpret ed as summation bands of fundamental frequencies with successive levels of a librating oscillator The libration is considered to represent a planar torsional oscillation of the anion about the trigonal axis. The librating frequency depends in part on the crystal structure and decreases with increasing cation mass The librating frequency as determined from successive bands was reasonably constant. In $RbNO_3$ two modes were observed one at 25 cm^{-1} and the other at 30 cm^{-1}. Band limits observed in the spectra were interpreted as representing rotational energy barriers. The barrier heights were 146 cm^{-1} and 175 cm^{-1}.

Greenberg and Hallgren[52] have observed the infrared spectra of $LiNO_3$, $NaNO_3$, KNO_3, $RbNO_3$ and $CsNO_3$ at room temperature, at $25^{\circ}c$ above and at $25^{\circ}c$ below the melting points of these nitrates They have reported that the spectra of alkali metal nitrates consist almost exclusively of the frequencies to be associated with the NO_3 group and are not materially altered in going from solid to liquid state The shift in observed frequencies

with cation size is as follows. With increasing cation size, ν_4, ν_1 and ν_3 frequencies show a general shift to lower values while ν_2 moves to higher frequencies. Also it has been observed[52] that the fundamental frequencies shift to lower values as the temperature is raised. No uniform change with temperature was detected for the combination and overtone bands.

Myasnikova and Yatsenko[53] have recently examined the infrared spectra of cooled melt of $RbNO_3$ at IV $\longrightarrow$ III transformation. The band frequency corresponding to the internal vibration ν_3 of NO_3^- ion is found to be shifted by about 12 cm^{-1} on passing from phase IV to III.

The contribution of internal vibration ν_3 of NO_3^- ion in $RbNO_3$, to the change in dielectric constant is found to be very small. Therefore the structure vibrations seem to play an important role in giving rise to anomalously large dielectric constants at the phase transition. Shifting of other bands can be explained similarly.

1.8 Solid Solutions.

The systems of interest in the present study are the solid solutions $K_xRb_{1-x}NO_3$ and $Cs_xRb_{1-x}NO_3$. Hence a literature study of these is described in this section.

1.8.1 $K_x Rb_{1-x} NO_3$ system

The series $K_x Rb_{1-x} NO_3$ is said to form a solid solution for the whole range of concentration [54,55]. Kawabe et al [56,57] have studied the dielectric properties of the $K_x Rb_{1-x} NO_3$ mixed crystals on the Potassium rich side. They have also investigated the temperature dependence of the lattice parameters of $K_{0.77} Rb_{0.23} NO_3$ [57] by high temperature x-ray powder diffractometry. At room temperature the x-ray powder diffraction patterns of these mixed crystals show that the lattice parameters vary linearly with concentration. A mixing limit was found [56] at x = 0.44 to 0.48.

Dantsiger [58] has investigated the phase diagram of $K_x Rb_{1-x} NO_3$ system. The Rubidium rich side was studied by dielectric measurements as a function of temperature while the Potassium rich side was investigated by oscillographic measurements only.

The transition III $\longrightarrow$ II during cooling was observed upto 3 - 5 % KNO_3, while in warming it was observed upto 10 - 15 % KNO_3 [58]. However, the doping lowers the transition temperature and reduces the peak value of ϵ. In addition the transition becomes increasingly smeared out. The transition IV $\longrightarrow$ III does not disappear at all. At first it is almost independent of the composition and then, beginning with 10 - 15 % KNO_3 the temperature of the transition decreases [58]. The transition points are shown in fig 1.8. The symbols II, III and IV in the diagram on the
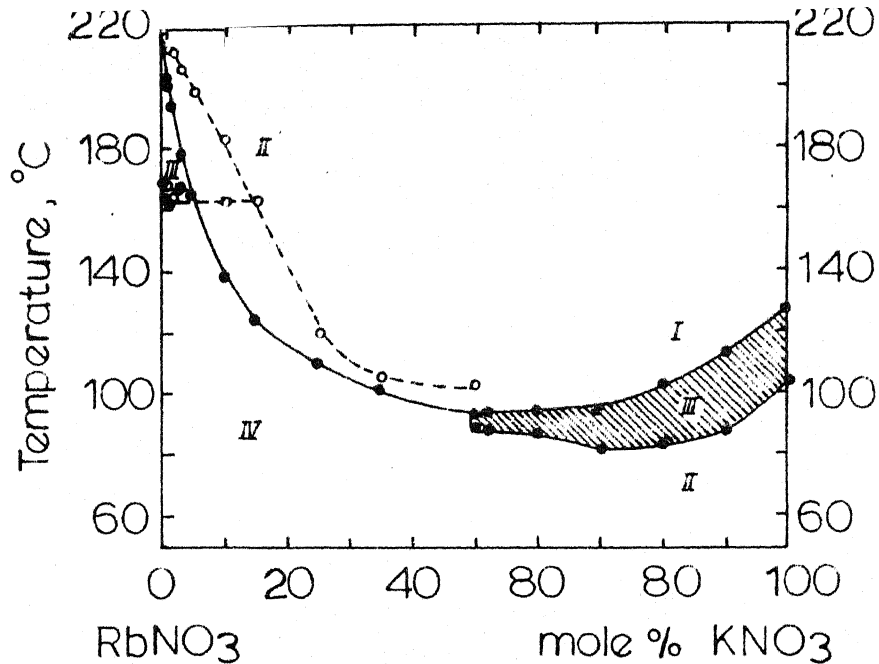
Fig. 1.8 Phase diagram of the $K_x Rb_{1-x} NO_3$ system. The solid curve corresponds to cooling and the dashed one to heating (ref. 58).
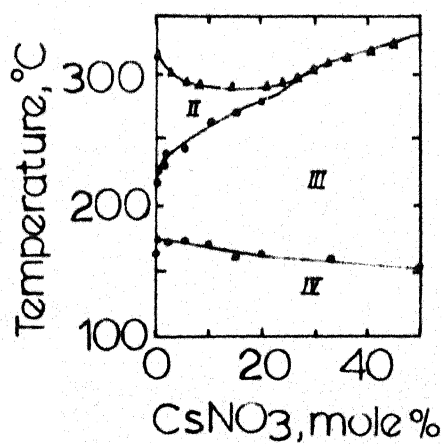
Fig. 1.9 Phase diagram of the system $Cs_x Rb_{1-x} NO_3$ (ref. 61).

RbNO$_3$ side denote the different phases of RbNO$_3$. As was noted above[31] phase IV of RbNO$_3$ has antiferroelectric properties. The reasons for this inference were the abrupt jumps in ε at the IV $\rightleftharpoons$ III transition, the effects of a dc bias field on this transition and the double hysteresis loops observed in phase IV in strong fields.

In all the investigated solid solutions the anomaly of ε at IV $\rightarrow$ III transition temperature persists and double dielectric hysteresis loops are observed in phase IV. Hence it is reasonable to infer the existence of antiferroelectricity in the low temperature phase of the investigated solid solutions[58], just as in the case of pure RbNO$_3$.

Investigation of compositions with a high KNO$_3$ content[58,59] revealed a ferroelectric region (shaded in the diagram of fig 1.8) In this region there are observed ordinary dielectric hysteresis loops. The symbols I, II and III in the phase diagram on the side of KNO$_3$ denote the different phases of KNO$_3$ as identified by Sawada et al[32]. On the KNO$_3$ rich side the phase diagram proposed by Dantsiger (Fig. 1.8) is in reasonable agreement with that of Kawabe et al[56,57].

1.8.2 $Cs_xRb_{1-x}NO_3$ System.

This system forms a continuous series of solid solutions.[55,60]

Dantsiger[61] has made (i) dielectric measurements

as a function of temperature at a frequency of 1 Mc/S and (ii)

oscillographic measurements with the usual Sawyer - Tower

circuit on the cooled melts of this system. It was observed

from the dielectric data that as x increases, the transition

temperature III $\rightleftharpoons$ II in $RbNO_3$ shifts to higher temperatures.

Fig. 1.9 shows the phase diagram of this system,

based on the dielectric measurements [61]. The numbers II, III and

IV denote the phases of $RbNO_3$. The highest temperature phase I

could not be observed during these measurements since the lower

boundary of this phase was close to the melting point[61]. The

upper curve (fig 1.9) mearked by triangles, was plotted from

the crystallization temperatures given by Blidin[60].

It is also noted that[61] (i) transition temperature

III $\rightleftharpoons$ II is present throughout the range $0 < x < 0.5-0.20$,

(ii) Curie-Weiss law is followed both below and above this

transition temperature and (iii) no hystereis loop is observed

in phase II of the compositions. On the basis of these

observations it is concluded that phase II of the solid solutions

is antiferroelectric. The possibility that the phase IV of these

compositions is also antiferroelectric (like the phase IV in $RbNO_3$) is considered. However, the dielectric anomalies in these compositions at IV $\rightleftharpoons$ III transition, are less pronounced than in pure $RbNO_3$. Dantsiger[61] has proposed that the antiferroelectric properties in phase II of the solid solutions as well as in $RbNO_3$ occur as a result of ordering of the NO_3 groups above the transition temperature.

It can be noted, from section 1.8.1 and the present one, that as x increases the transition temperature III $\rightleftharpoons$ II moves to higher temperatures in $Cs_x Rb_{1-x} NO_3$ system and in the opposite direction in $K_x Rb_{1-x} NO_3$ system. Dantsiger[61] has explained this shifting of transition temperature on the basis of the difference in the radii of the cations that do the replacing in the solid solutions. The radii of Rb^+, Cs^+, and K^+ are respectively 1.48, 1.69, and 1.33 A^o. When Cs^+ (larger size) replaces Rb^+, the lattice constant increases. (According to x-ray data, the lattice constant of $CsNO_3$ in cubic phase is larger than the lattice constant of $RbNO_3$[10]). This results in a reduction of the internal field, and, hence in a reduction in the stability and narrowing of the phase II. Replacing Rb^+ ion by K^+ ion, which has smaller size, produces the opposite effect.

Chapter 2

STATEMENT OF THE PROBLEM

Nitrates show a rich variety of structural trans-
formations, indicating that diverse arrangements with practically
the same free energy can be arrived at by comparatively small
shifts of the cations and the anions. As already seen in
chapter I phase transformations in $RbNO_3$ and their solid
solutions have been the subject of several investigations.

However, a clear understanding of the transformations
in $RbNO_3$ does not seem to be available. Due to this reason it
is difficult to find proper explanations for the electrical
conductivity and thermal expansion changes during the
transformations. Whereas phase I has been detected by x-ray
diffraction[4,5], differential thermal analysis[8,47] and dilatometry[2,13]
the same has not been confirmed by electrical conductivity,
and infra-red absorption studies. Differences in conductivity
changes, at phase transformation II $\rightleftharpoons$ III and III $\rightleftharpoons$ IV,
observed on recycling in $RbNO_3$ have remained unexplained. It
is, therefore, thought worthwhile to study the whole spectrum
of properties in all phases of $RbNO_3$ and synthesize the results
for a better understanding of the phase transformations in
$RbNO_3$ and its solid solutions and propose a suitable model for
these transformations.

Hence a detailed study of the phase transformations

in $RbNO_3$ has been undertaken by means of (ac) electrical
conductivity, differential thermal analysis, dilatometry, high
temperature X-ray examination and infra-red absorption.
Thermal hysteresis at the transformations and co-existence
of phases in the transformation regions are also investigated.
Disordering of the NO_3 group in various phases is examined.
The study is extended to cover the influence of substitution
of K^+ (ionic radius = 1.33 A^0) and Cs^+ (ionic radius = 1.68 A^0)
for Rb^+ (ionic radius = 1.48 A^0) in $RbNO_3$ on the phase
transitions.

Chapter 3

EXPERIMENTAL TECHNIQUES

3.1 Sample Preparation:

$RbNO_3$ and $CsNO_3$ were obtained from Penn Rare Metals Inc., Revere, Penna (USA) The purity claimed by the manufacturer is 99·8 and 99.9% respectively KNO_3, of Analar quality, was obtained from the British Drug House

$RbNO_3$ in powdered form, as supplied, was the starting material for investigations on $RbNO_3$ Solid solutions were prepared by heating $RbNO_3$ with a known molar % of $CsNO_3$ or KNO_3 in a platinum crucible to a temperature of about $20^\circ C$ above the melting point of the material This temperature was maintained constant for half-an-hour to allow for thorough mixing and formation of a solid solution. homogeneity of the solid solutions was confirmed by X-ray diffraction methods The solid solutions so formed were crushed to a powder

DTA and X-ray measurements were made on powdered samples. The powders were melted and poured into a platinum foil tube to make rods of about 1.5 cm length and 4 mm diameter

for dilatometric measurements. The fine powder was pressed at 4.22×10^5 gm / cm^2 pressure into thin 1.2 cm diameter transparent pellets for infra-red work.

3.2 Conductivity Measurements

Powdered specimen of RbNO$_3$ or its solid solutions was melted in a platinum crucible. A glass cover (fig 3.1) was lowered to dip the platinum foil acting as one of the electrodes, into the melt Te crucible acted as the other electrode. The melt was cooled and was ready for measurements.

This procedure permits a rapid investigation of different compositions. A technique similar to the present one was first employed in the work of Sawada et al[32] for investigating dielectric hysteresis loops of KNO$_3$. Sawada et al note that the complicated arrangement of electrodes does not allow a precise evaluation of the absolute value of the polarization. For the same reason, the conversions of conductance data to the conductivity values, taking into account only the area of the platinum foil electrode and the distance between the foil and the bottom of the crucible, may be correct to $\pm$ 10 %.

Using General Radio 1608 A impedance bridge, at a frequency of 1 KC/S, conductance was measured between 120°C and the melting point during heating and cooling the compositions. Below 120°C the conductance was too low to be reliably measured on the bridge. The (ac) electrical conductivity was measured to avoid electrolysis of the ionic salt and to avoid the voltages which may be developed due to polarization effects. The temperatures were measured with a chromel-alumel thermocouple and
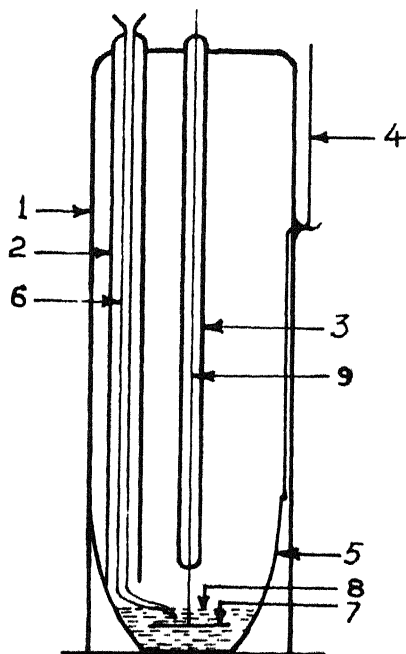
Fig. 3.1 Platinum crucible (5), containing the material (8)
under study. Platinum foil (7) and the crucible
are acting as the two electrodes. (2) and (3) are
glass tubes containing the platinum wire (9),
carrying one electrode, and the thermocouple (6).
(4) is a lead for the crucible electrode and (1) is
the pyrex glass cover.

a Rubicon potentiometer. The rates of heating and cooling during the measurements varied between 1.5 to $2^{\circ}C$ per minute. The measurements on each specimen were repeated both on heating and cooling and were found reproducible (not shown in the figures). Solid solutions cooled down to a clear solid mass upto 20 mole % of $CsNO_3$ in $RbNO_3$ while a separate small white patch was observable in the clear cooled mass of solid solutions at 25 molar % $CsNO_3$ and above. The cooled solid solutions of $K_xRb_{1-x}NO_3$ yielded a clear mass upto 2 molar % KNO_3 and a white opaque solid at 4 molar % and above.

3.3 Differential Thermal Analysis (DTA).

Gordon[62] has described the principle of Differential Thermal Analysis and various DTA instruments including that of the American Instrument Co., which was used in this investigation.

About 0.3 to 0.4 gm of the powder of $RbNO_3$ or its solid solutions (Cs, Rb)NO_3 and (K,Rb) NO_3 was packed into one of the sample holders (a hole) in the metal block of DTA apparatus, the other hole being packed to an equal volume with a reference material – quartz (SiO_2) powder. The furnace was heated at the rate of $8^{\circ}C$/ min. On reaching the maximum temperature the furnace was put off and it was allowed to cool at a natural rate For recording the differential thermogram a sensitivity of temperature differential of $0.1^{\circ}C$ per inch of the chart paper was employed. The maximum temperature to which each sample was heated was about $40^{\circ}C$ below the melting point so that the II $\rightleftharpoons$ I transformation

in $RbNO_3$ and its solid solutions was not recorded (since it was too close to the melting point).

Temperatures near the melting point of $RbNO_3$ were avoided to guard against the corrosive tendency of molten $RbNO_3$ for the Inconel sheath of the chromel alumel thermocouple used in the sample holder.

3.4 Dilatometric Measurement of Thermal Expansion

The thermal expansion of rod specimens, of $RbNO_3$ and its solid solutions, of diameter 4 mm and length 1.5 cm was measured using a fused-quartz tube dilatometer with an optical lever having a magnification of about 450 (Appendix C). The measurements were performed both on heating and cooling, the rate of temperature change being $2^{\circ}C$ / min. The measurements were continued upto a temperature of about $20^{\circ}C$ below the melting point. Beyond that temperature the sample rod begins to deform plastically.

3.5 X-Ray Diffraction Study.

X-ray diffraction methods were used for (i) establishing solid solution formation, (ii) lattice parameter study as a function of temperature, (iii) thermal hysteresis in transformation regions, and (iv) Co-existence of phases in the transformation range

3.5.1 Room Temperature Study.

Solid solution compositions in the systems $K_xRb_{1-x}NO_3$ and $Cs_xRb_{1-x}NO_3$, cooled from the liquid state, were examined at room temperature, using CuK_α radiation. General Electric XRD-6 diffractometer and a GEXRD-5 x-ray unit with a 11.4 cm

diameter Debye-Scherrer Camera were used for this study.
Reflections with $2\theta \leqslant 60^{\circ}$ were employed for lattice parameter
determinations.

3.5.2 Lattice Parameters

Powder diffractometer traces of $RbNO_3$ and its solid
solutions $(Cs, Rb)NO_3$ and $(K, Rb)NO_3$ were recorded as a
function of temperature using Tempress Research furnace with a
controller on the General Electric XRD-6 x-ray diffraction
unit. The powder sample was packed into a rectangular
depression of the platinum sample holder which was inserted in
its place in the furnace. Slits used were 1° collimator slit,
medium resolution soller slit, and 0.02° detector slit. Scanning
rate was 0.2° (2θ) per minute and recording was at 12 " (or
30.48 cm) per hour [i.e. 1° (2θ) per inch of chart paper] .
Temperature was maintained constant within $\pm 2^{\circ}C$ for half-an-
hour or more before recording the diffraction pattern.
CuK_{α} radiation was used . Lattice parameters were calculated
from reflections in the range $20^{\circ} < 2\theta < 60^{\circ}$. Maximum error in
the measurement of d values is therefore ± 0.055 %.

3.5.3 Thermal Hysteresis

Thermal hysteresis at the transformation region
was studied by two methods : dynamic and static methods.

The dynamic method described below is similar to
the one employed in the work of Wahl et al[63] and Schneer and
Whiting[64]. In this method an angular range of $2\theta = 2^{\circ}$ was
continuously scanned around the line (110) by oscillating the
diffractometer over this range during heating and around (102)

during cooling. During heating (110) vanishes in III → II transformation whereas (102) vanishes in the reverse transformation. While the diffractometer was oscillating to trace the same diffraction line the temperature was recorded as a function of time on a Moseley X-Y recorder. The heating rate was $1^\circ C$/Min and the scanning rate was $4^\circ (2\theta)$/Min. Time-temperature and 2θ-time graphs were utilized to find the 2θ vs temperature record. Height of the x-ray line during heating and cooling was plotted as a function of temperature (Fig 5.4). In the static method, the temperature was kept constant and the (110) as well as the (102) lines were recorded at each constant temperature while traversing the transformation region, continuing till (110) vanishes during heating [(102) appears before (110) vanishes] and until (102) vanishes during cooling [(110) appears before (102) vanishes]. A plot of peak height vs temperature during heating and cooling yields a hysteresis loop (Fig 5.5).

3.5.4 Coexistence of Phases.

Diffraction lines (110), characteristic of phase III, and (102), characteristic of phase II, are recorded at each constant temperature in the static method. Appearance of phase II before III vanishes and vice versa is seen through the trace of these lines (Fig 5.2)

3.6 Infrared Absorption

Thin transparent pellets of $RbNO_3$ and its solid solutions, prepared in the manner described in section 3.1, were placed between two asbestos paper rings and supported in a

pyrex glass holder (fig 3.2). The pyrex glass holder consists
of two glass tubes sliding into each other. The diameter of
the outer tube was reduced at one end so that the inner tube
cannot pass through this end. The glass holder was placed
inside in a pyrex glass double walled infrared cell (fig 3.2)
containing a cylinderical furnace. The cell was mounted on
the window of the infra-red spectrophotometer. This high
temperature infrared cell is constructed following Vranty and
Graves[65]. While the furnace was heated, the outside was
cooled by forcing air through the double-wall. The temperature
was maintained constant within $\pm 2^{o}C$ by an Electromax temperature
controller and measured by a chromel-alumel thermocouple kept
close to the sample. The spectra were recorded on a Perkin-
Elmer model 521, double beam Grating-infra-red Spectrophoto-
meter.

Figs 4.18 and 4.19 show the spectra of the transparent
pellets of $RbNO_3$ at different temperatures marked thereon and
the figs 4.18 and 4.19 that of the solid solutions $Cs_{0.10}Rb_{0.90}NO_3$
and $K_{0.02}Rb_{0.98}NO_3$ at room temperature.
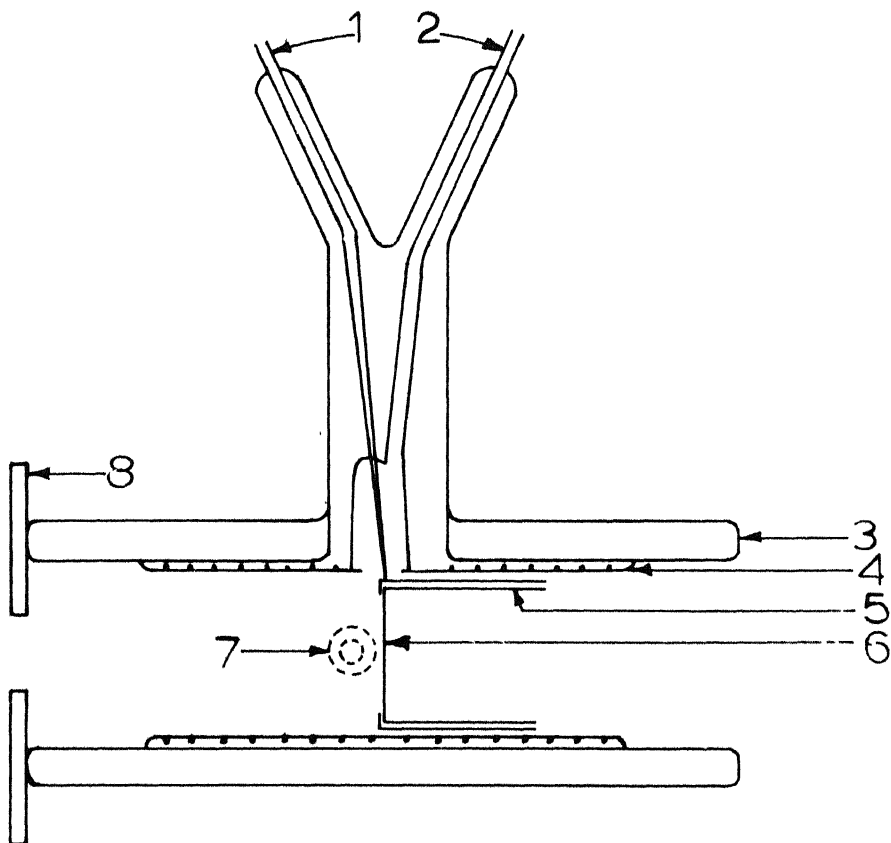
Fig. 3.2 High temperature infrared cell. (1) Chromel-alumel
thermocouple, (2) heater leads, (3) double-walled
pyrex glass cylinder, (4) Nichrome wire wound
(pyrex glass muffle) furnace, (5) Pyrex glass sample
holder, (6) sample (pellet), (7) inlet and outlet to
double-walled cylinder for air cooling and (8) a brass
strip to hold the cell onto the infrared spectrophotometer
window.

Chapter 4

RESULTS

4.1 Electrical Conductivity

4.1.1 Rubidium Nitrate

A plot of conductivity of $RbNO_3$ vs $1000/T$ (T is the absolute temperature), on a semi-log scale, in the temperature range $120°C$ to above the melting point, is shown *(also Appendix D)* as the lower most curve of figs. 4.1 and 4.2. It is evident from this curve, as pointed out by Brown and McLaren[4], that phase transformations in $RbNO_3$ are marked by discontinuities in electrical conductivity. The magnitude and the nature of the conductivity changes at the phase transitions are tabulated below.

Transition	Conductivity change
IV $\longrightarrow$ III	Sudden increase by a factor of about 1000 (corresponding decrease during the reverse transformation)
III $\longrightarrow$ II	Sudden drop by a factor of about 100 (corresponding increase during cooling).
II $\longrightarrow$ I	Gradual increase by a factor of about 3 (gradual decrease by a factor of about 25 in the reverse transformation)
I $\longrightarrow$ Liquid	Gradual increase by a factor of about 200 (gradual decrease by a factor of 35 during cooling).
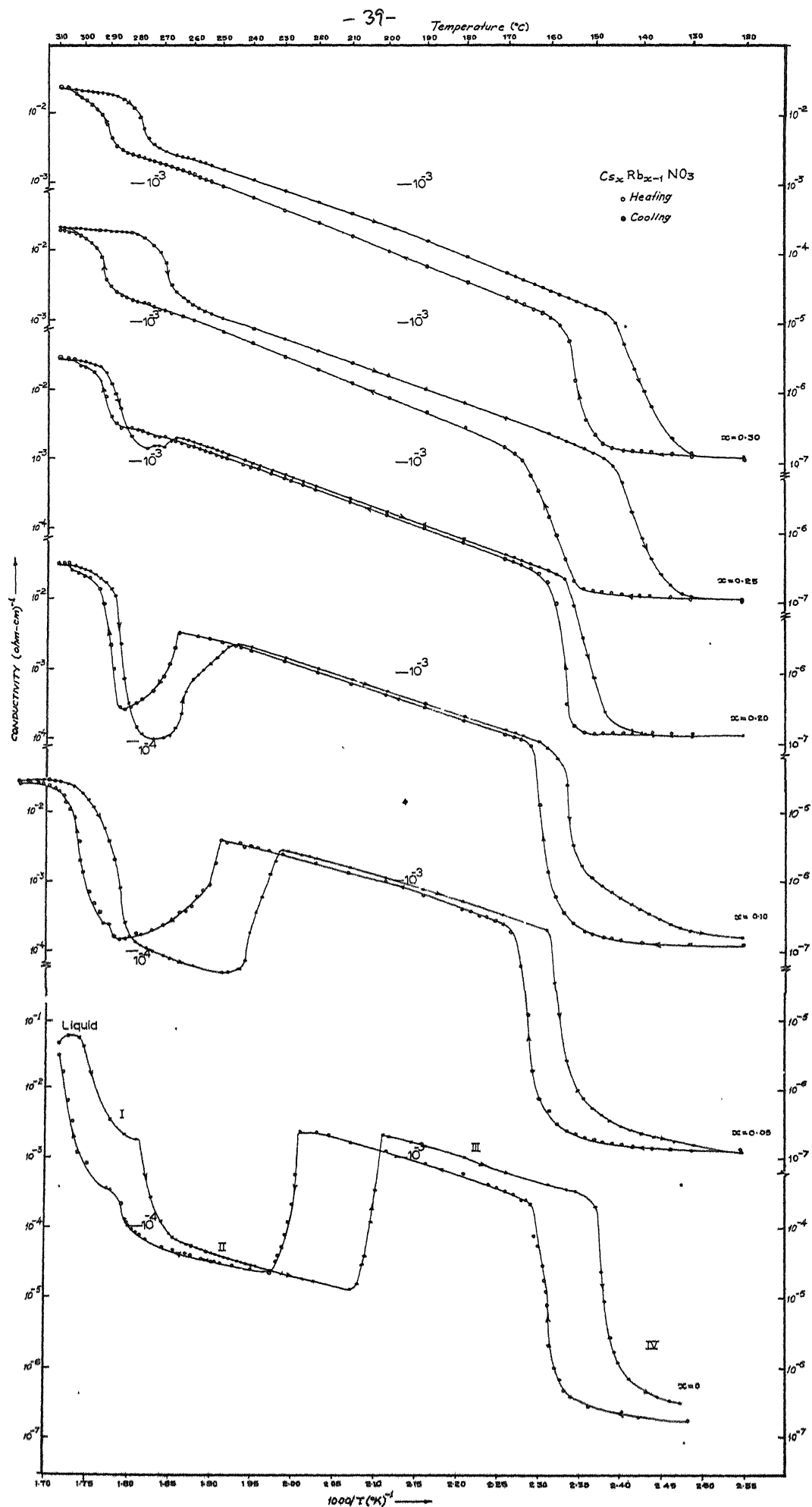
Fig. 4.1: Temperature dependence of electrical conductivity in the system $Cs_xRb_{1-x}NO_3$
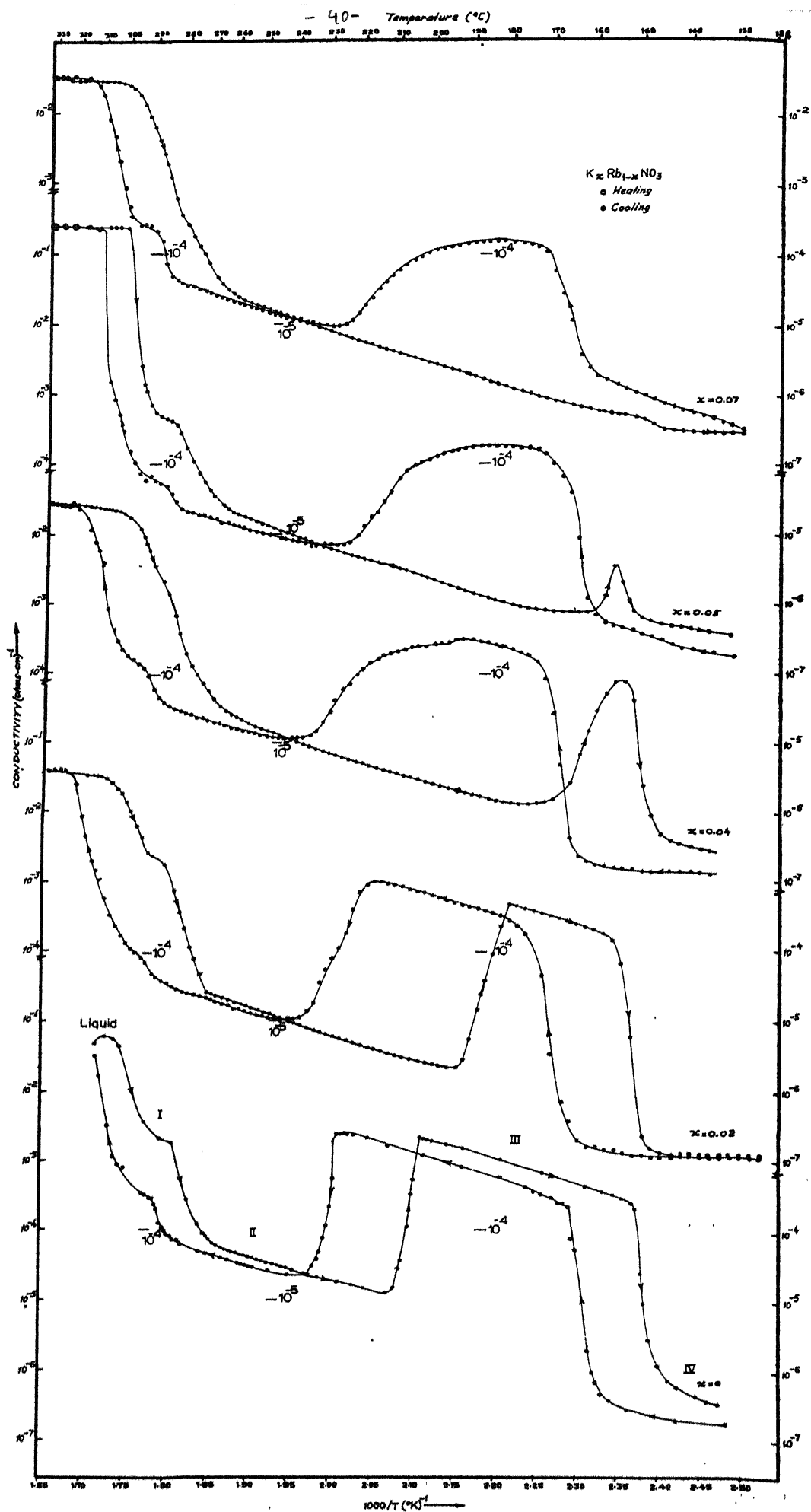
Fig. 4.2: Temperature dependence of electrical conductivity in
the system $K_x Rb_{1-x} NO_3$.

The magnitude of the conductivity changes observed at II $\longrightarrow$ I and I $\longrightarrow$ II as also at I $\rightarrow$ liquid and liquid $\longrightarrow$ I are markedly unequal. This is probably due to the gradual nature of these transitions. It is, therefore, expected that the magnitude of the steps observed in conductivity plots would be a function of the rate of temperature change. The orders of magnitude of conductivity changes observed here are in good agreement with those reported by Brown and McLaren[4] (fig. 1.4) except during the first cycling. These data confirm the observations of Brown and McLaren[4] that the higher symmetry (cubic) phases (I and III) have high electrical conductivity and low symmetry phases (trigonal IV and hexagonal II) have low conductivity.

The conductivity curve for $RbNO_3$ also shows that for each stable phase a plot of log σ vs I/T yields a straight line. This follows from the relation between the conductivity of a solid and its absolute temperature, T, i.e.

$$\sigma = Ae^{-E/kT}$$

or log $\sigma =$ log A $-$ E/kT

where A is a constant, E is the activation energy for conduction and k is the Boltzmann constant. From the slopes of these straight lines the activation energies of different phases of

$RbNO_3$ are calculated and are given below (table 4.1).

Table 4.1 Activation energy for electrical
conduction for different phases
of $RbNO_3$

Phase	Activation Energy E (ev)	
	during heating	during cooling
II	0.92	0.64
III	0.40	0.30
IV	0.88	1.03

Although no activation energy values are given by Brown and McLaren[4] a comparison, of the relative slopes of the straight line portions (fig 1.4) in different phases of $RbNO_3$, shows that the values of activation energy for the three different phases as tabulated here are of the correct relative order. It is clear from table 4.1 that the high symmetry phase (i.e. phase III) has a lower activation energy as compared to low symmetry phases (phases IV and II), as expected. Also out of the low symmetry phases, the one at lower temperature (phase IV) has a higher activation energy as compared to that at higher temperature (phase II). This is again an expected result.

The phase transformation temperatures during heating and cooling, observed from the conductivity plot for $RbNO_3$, are shown in table 4.2. The difference between these temperatures gives the temperature hysteresis at these transformations.

The transition temperatures found by the various methods of study are in reasonable agreement with each other and with those in literature. The temperature hysteresis at the III $\longrightarrow$ II transition found by static x-ray method agrees well with that reported by Calorimetric method[44]. Other methods of study give larger temperature hysteresis. This is probably due to relatively faster rates of heating and cooling. In this connection it may be noted that the fastest rates of heating and cooling are employed in the DTA study.

4.1.2 Solid Solutions in Systems $Cs_xRb_{1-x}NO_3$ and $K_xRb_{1-x}NO_3$.

In figs. 4.1 and 4.2 are plotted, on a semi-log scale, the conductivity vs reciprocal absolute temperature for $Cs_xRb_{1-x}NO_3$ and $K_xRb_{1-x}NO_3$ systems respectively. (Appendix D) Data obtained during heating and cooling are shown. The phase transition temperatures in these systems, during heating in $Cs_xRb_{1-x}NO_3$ system and during heating and cooling in $K_xRb_{1-x}NO_3$ system, are summarised in figs. 4.3 and 4.4 respectively. (also table 4.2) The general features of the phase diagram, Fig. 4.3, are reproduced by the conductivity data on cooling (not shown in the figure).

TABLE 4.2: Phase transformation temperatures during heating and cooling.

System	Value of x	DTA		Conductivity		Dilatometri		X-ray		Other methods	
		h	c	h	c	h	c	h	c	h	c
$RbNO_3$	x=0	170 164[8] 166[47]	159 153[47]	159 164[4]	145 161[4]	158	149	164[17]		161$\pm$2[2] 160[4] 160[44] 164.4[45] 161[61]	
$_xRb_{1-x}NO_3$	x=0.05	168	155	162	155	158	148			174[61]	
	x=0.10	166	152	158	154	154	144			167[61]	
	x=0.20	152	140	156	148	145	132			161[61]	
$_xRb_{1-x}NO_3$	x=0.02	170	158	167	151	156	147				
	x=0.04	163	153	166	147	155					
$RbNO_3$	X=0	231 219[8] 228[47]	213 202[47]	229 230[4]	206 218[4]	216	198	236^d 231^s	224^d 223^s	219$\pm$2[2] 220[4] 219[5] 199.8[26] 218[44] 211[44] 220[45] 217[61]	
$Rb_{1-x}NO_3$	x=0.05	250	230	252	237	240	220	250^d	240^d	245[61]	
	x=0.10	267	244	274	257	258	240	271^d	262^d	261[61]	
	x=0.20			283	269					278[61]	
$Rb_{1-x}NO_3$	x=0.02	218	196	225	185	208	178	223^d	199^d		
	x=0.04	204		214	164	190		206^s	190^s		

TABLE 4.2 (Continued)

System	Value of x	Transition temperature (°C)									
		DTA		Conductivity		Dilatometri		X-ray		Other methods	
		h	c	h	c	h	c	h	c	h	c
$RbNO_3$	x=0	$291^{(8)}$ $278^{(47)}$	$270^{(47)}$	284 $282^{(4)}$	274	269	263			$282\pm1^{(2)}$ $290^{(4)}$ $284^{(5)}$ $281^{(44)}$	
$Cs_x Rb_{1-x} NO_3$	x=0.05			288	270	264	251				
	x=0.10			292	281						
	x=0.20			292	285						
$K_x Rb_{1-x} NO_3$	x=0.02			274	263						
	x=0.04	277	274								

Symbols: h and c represent heating and cooling, d and s stand for dynamic

and static methods of X-ray investigations   Numbers in parenthesis

indicate reference numbers   DTA temperatures of the present study and

of reference 47 refer to the temperatures of the peak of the DTA curves.

Values of ref· 61 are obtained from the phase —diagram of $Cs_x Rb_{1-x} NO_3$

(figure 1.9).
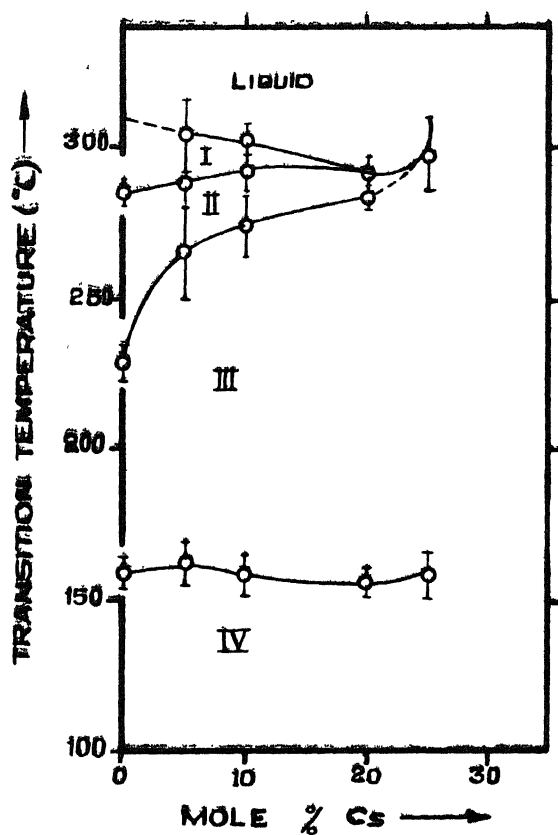
Fig. 4.3 Phase transitions in the system $Cs_xRb_{1-x}NO_3$, based on electrical conductivity data during heating.
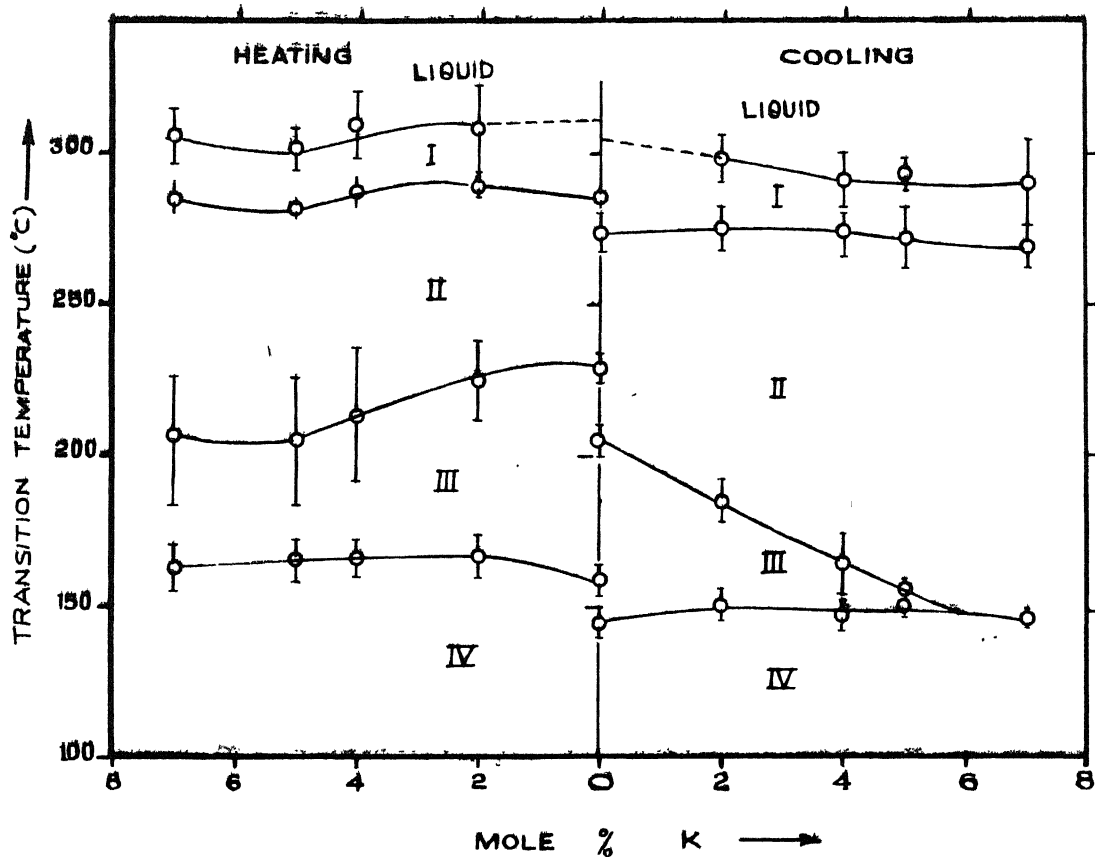
Fig. 4.4 Phase transitions in the system $K_xRb_{1-x}NO_3$, based on electrical conductivity data during heating (left) and cooling (right).

The symbols I, II, III, IV and 'liquid' in these diagrams denote the different phases of $RbNO_3$ as described in section 1.2. The temperature range of transformation is indicated by the length of the vertical line at each point on these curves (figs 4.3 and 4.4). The effect, of substitution of Cs^+ or K^+ for Rb^+ in $RbNO_3$, on the discontinuities in conductivity, conductivity of different phases and transition temperatures is given below in tabular form(referring to figs. 4.1 and 4.2)

As **x** increases	$Cs_x Rb_{1-x} NO_3$ System	$K_x Rb_{1-x} NO_3$ System
(i) Transition temperature II ⇌ III	Decreases slightly	Shifts slightly to lower temperatures
(ii) Transition temperature III ⇌ II	Marked shifts to higher temperatures – slightly more during cooling than during heating	Shift to lower temperatures is small during heating and very large during cooling
(iii) Discontinuity III ⇌ II	(a) Becomes increasingly sluggish	(a) Grows extremely sluggish — largely during heating only
	(b) Disappears between 20 and 25 mole % of $CsNO_3$	(b) Disappears during cooling at a little above 5 mole % KNO_3. Does not vanish during heating
(iv) Transition temperature II ⇌ I	Shifts slightly to low temperature side	Moves slightly to lower temperatures
(v) Discontinuity II ⇌ I	Vanishes at 10 mole % $CsNO_3$	Continues throughout the range of solid solutions

			During heating it seems to fade at ~ 2 mole % KNO_3 but becomes prominent at higher concentrations. During cooling fading is seen at ~ 4 mole % KNO_3
(vi)	Mixing limit	(a) Between 20 and 25 mole % $CsNO_3$ for phase II. (b) Probably 10 mole % $CsNO_3$ for phase I.	A little above 5 mole % KNO_3 for phase III (from conductivity data during cooling)
(vii)	Melting point	Decreases slightly till the mixing limit after which it appears to increase	Is lowered slightly till the mixing limit after which it seems to rise
(viii)	Conductivity of (a) phases III and I, and (b) phase II.	(a) Decreases and (b) Increases	Decreases in all these phases

As seen from fig. 4.1, at concentrations greater

than or equal to 25 mole % $CsNO_3$ in $Cs_xRb_{1-x}NO_3$ system, there is

a transition directly from phase III to the melting region.

The phases III, II and I have all merged with each other.

Structurally, the phases IV and III of $RbNO_3$ are probably similar

to the two crystalline phases of pure $CsNO_3$. Crystallographic[13],

thermodynamic[49] and high pressure data[36,37] also suggest a similar

possibility.

It may be noted from the cooling curves of fig. 4.2

that the region of phase II, in $K_xRb_{1-x}NO_3$ system, is getting

widened very fast with increasing x. This continues to the

point of non-existence of phase III at a little above 5 mole %

KNO$_3$ which may thus be regarded as the limit of mixing of KNO$_3$

in phase III of RbNO$_3$.

These data confirm the following observations of Dantsiger[58]

on K$_x$Rb$_{1-x}$NO$_3$ system : (i) the solubility limit during cooling is

between 3 - 5 mole % KNO$_3$, (ii) III $\rightleftharpoons$ II transition point shifts

to low temperature side and is increasingly smeared out, and

(iii) IV$\rightarrow$III transition does not disappear at all. Also it

confirms the observations of Dantsiger[61] in Cs$_x$Rb$_{1-x}$NO$_3$: (i) the

transition III $\rightleftharpoons$ II shifts to high temperature side, and (ii)

the limit of solubility lies at x $>$0.20. The phase diagram of

the present study compares well with that of Dantsiger (fig. 1.9)

who could draw this diagram only for phases II, III and IV.

4.1.3 Phase I

In the conductivity plots, Phase I which precedes

melting was quite clearly observed, delimited by discontinuous

changes in conductivity at each end (figs 4.1 and 4.2), in

contrast to the conclusions of Brown and McLaren[4] and Dantsiger[26].

Brown and McLaren detected the transition   II $\rightleftharpoons$ I in

compressed powder pellets of RbNO$_3$ as only a change of slope in

the graph of log (conductance) vs reciprocal of absolute

temperature. Dantsiger could not observe phase I in his dielectric

measurements on cooled melts of $Cs_xRb_{1-x}NO_3$ system since be

according to him the lower boundary of phase I was too close

to the melting region. The existence of phase I has been

confirmed by other measurements such as x-ray diffraction[4,5]

infrared absorption, specific heat[44], differential thermal

analysis[8] and dilatometry[2].

4.2 Thermodynamic Parameters by Differential Thermal Analysis

The differential thermograms i.e. a plot of ΔT

(temperature difference between the sample and reference material)

vs temperature of reference, obtained both on heating and

cooling are shown in fig 4.5 for $Cs_xRb_{1-x}NO_3$ system and in fig

4.6 for $K_xRb_{1-x}NO_3$ system. From figs. 4.5 and 4.6 it can be

seen that as x increases : (i) Transformation temperature IV $\rightleftharpoons$ III

is shifting slowly to low temperature side (ii) Transformation

temperature III $\rightleftharpoons$ II is shifting markedly towards high

temperature direction in $Cs_xRb_{1-x}NO_3$ system and in the

opposite direction in $K_xRb_{1-x}NO_3$ system. In the latter system

shifts are more pronounced during cooling than during heating.

(iii) II $\rightleftharpoons$ I is shifting slowly to low temperature side.

As seen in section 4.1.2 the transformation III $\rightleftharpoons$ II grows

sluggish with increasing concentrations of $CsNO_3$ and KNO_3.

It is evident from figs 4.5 and 4.6 that this slow nature of

the transformations except for $x = 0.04$ in fig 4.6 is not detected
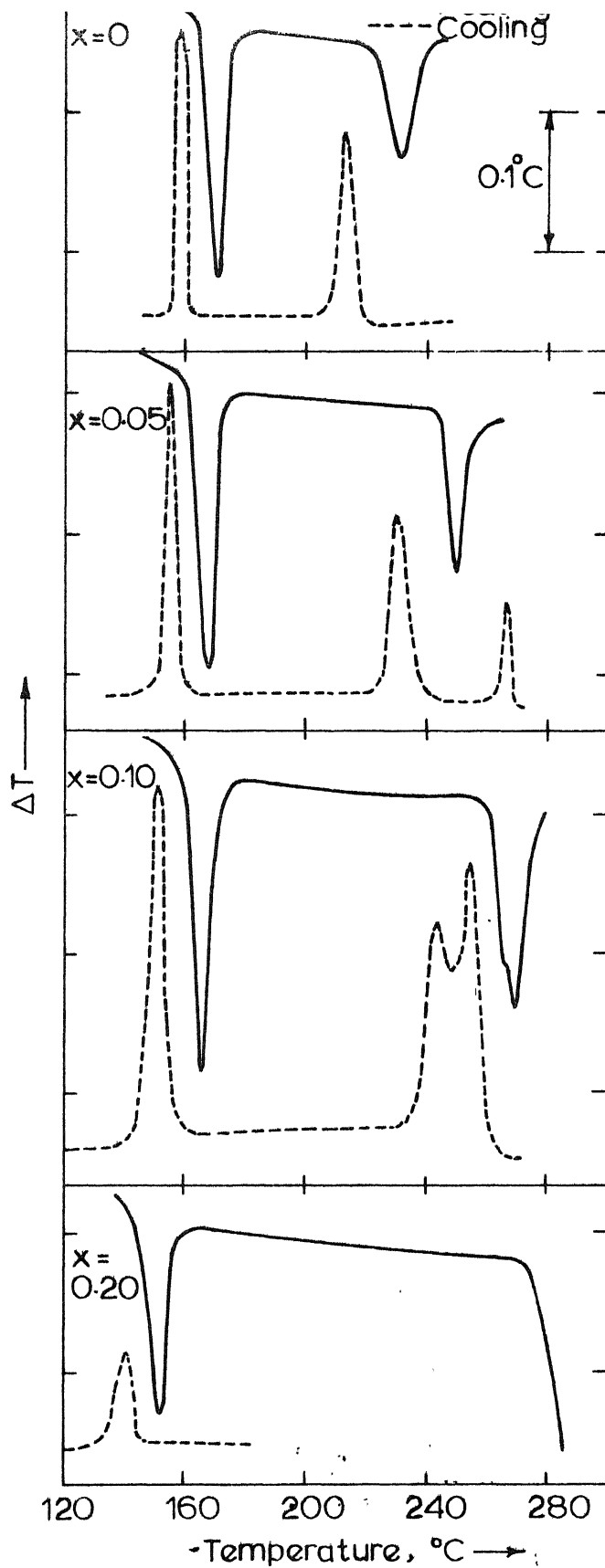
Fig. 4.5 Differential thermograms of $Cs_xRb_{1-x}NO_3$ system.
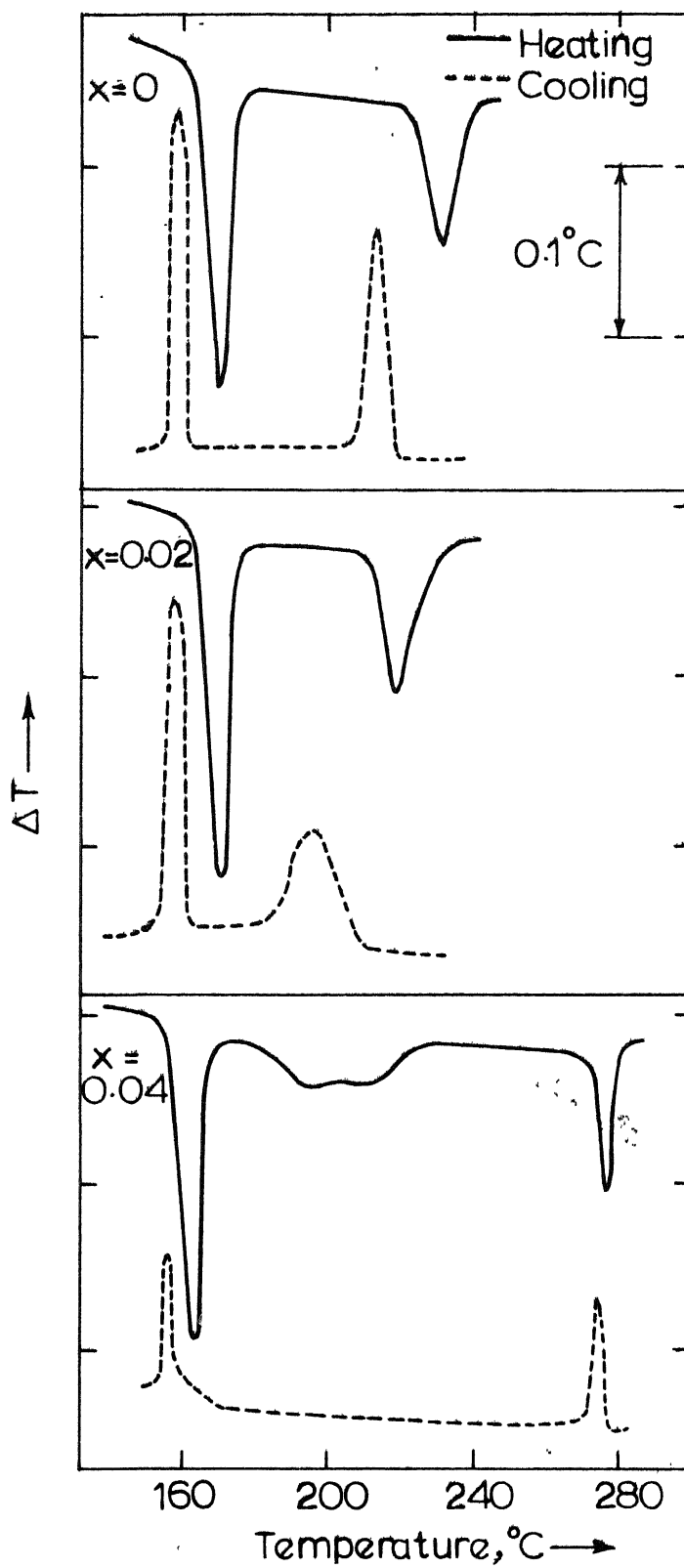
Fig. 4.6 Differential thermograms of $K_xRb_{1-x}NO_3$ system.

by differential thermal analysis. A somewhat similar conclusion

was reached earlier by Rao and Rao[47]. It is also seen from

figs 4.5 and 4.6 that transformation III $\rightleftharpoons$ II vanishes at

$x = 0.20$ in $Cs_x Rb_{1-x} NO_3$ system and II $\longrightarrow$ III at $x = 0.04$ in

$K_x Rb_{1-x} NO_3$ system. These conclusions, from the DTA data, confirm

those derived from the conductivity data.

Heats of transition are calculated from the peak

areas in DTA curves using the formula (Appendix A)

$$\triangle H = H \frac{m1}{m2} \frac{A_2 M_2}{A_1 M_1}$$

· where H represents the heat of transformation of a standard

material ($RbNO_3$ in this case); A_1, A_2 are the areas of the

respective peaks for standard and sample, m_1, m_2 are the masses

of the standard & sample materials and M_1, M_2 their respective

molecular weights. The molecular weights are the weighted mean

of the molecular weights of the host and the dopant in the ratio

of their composition in the solid solutions. The calculated

values for the heats of transition are tabulated (Table 4.3).

The value of heat of transition given by Mustajoki[44] (i.e. 932

cals/mole for IV $\longrightarrow$ III transformation in $RbNO_3$) has been assumed

for the calculations of $\triangle H$ for the solid solutions.

Table 4.3 Heats of transitions ($\triangle$H) and thermal energies of activation (E_a) from DTA curves.

Material	Transition IV $\rightarrow$ III $\triangle$H Cal/mole	E_a Kcal/mole	Transition III $\rightarrow$ II $\triangle$H Cal/mole	E_a Kcal/mole
RbNO$_3$ Literature values	932[44];923[45];950[47]	165[47]	767[44];774[45];650[47]	50[47]
Present study	–	166	610	104
$Cs_{0.05}Rb_{0.95}NO_3$	1165	110	573	175
$Cs_{0.10}Rb_{0.90}NO_3$	1022	97	372	136
$Cs_{0.20}Rb_{0.80}NO_3$	795	107	–	–
$K_{0.02}Rb_{0.98}NO_3$	1262	108	681	72
$K_{0.04}Rb_{0.96}NO_3$	885	128	717	60

The energy required for a transformation (i.e. the energy of activation Ea) can also be calculated from the DTA curves using the method of Borchardt and Daniels[64]. For this purpose the rate constant k of a reaction given by [64]

$$k = \frac{\Delta T}{A - a}$$

is determined. Here A represents the total area under the DTA curve (peak), 'a' and 'ΔT' are shown in fig. 4.7. The log k vs I/T plots are called the activation energy plots. These are shown in figs 4.8 and 4.9 for IV $\rightarrow$ III and III $\rightarrow$ II transformations in RbNO$_3$, $Cs_xRb_{1-x}NO_3$ and $K_xRb_{1-x}NO_3$ systems.
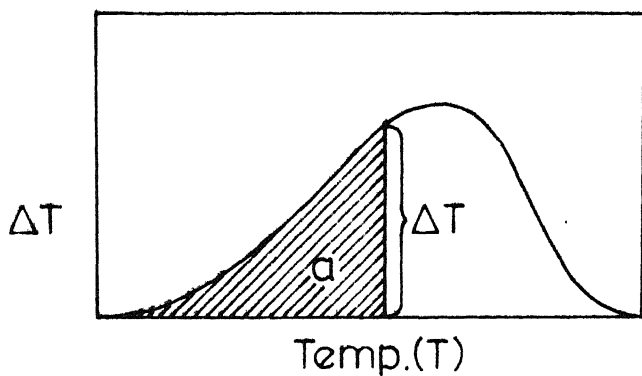
Fig. 4.7 Schematic DTA curve showing the
quantities in the rate equation k = ΔT/A-a
(ref. 64). k is the rate constant and A is
the area under the curve.
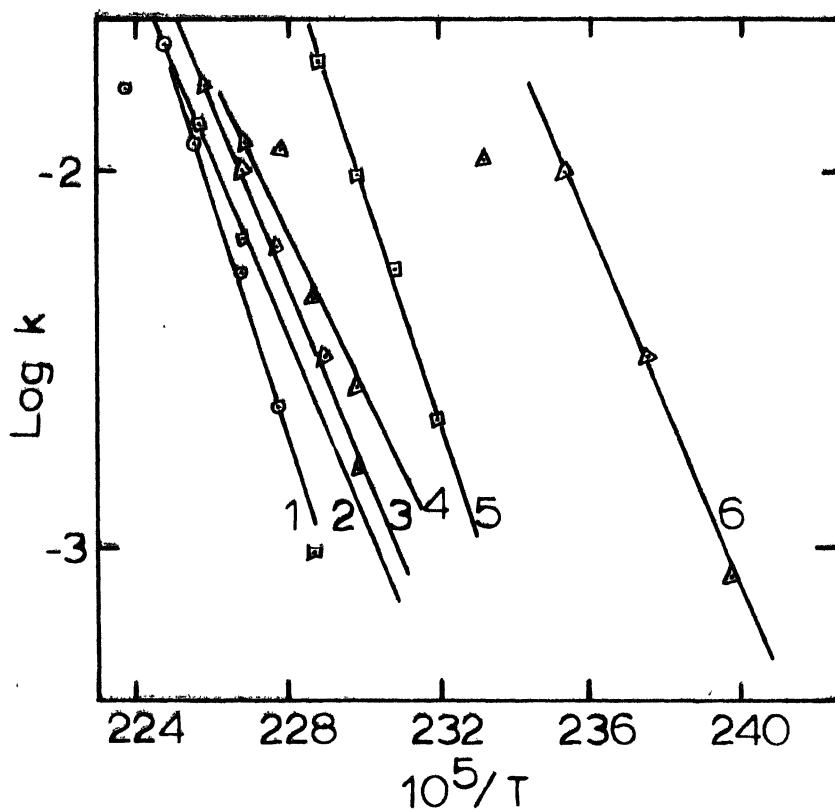
Fig. 4.8 Activation energy plots for IV $\rightleftarrows$ III transformation
Graph '1' is for $RbNO_3$; 3, 4, 6 for $Cs_x Rb_{1-x} NO_3$
(x = 0.05, 0.10, 0.20) and 2, 5 for $K_x Rb_{1-x} NO_3$
(x = 0.02, 0.04).
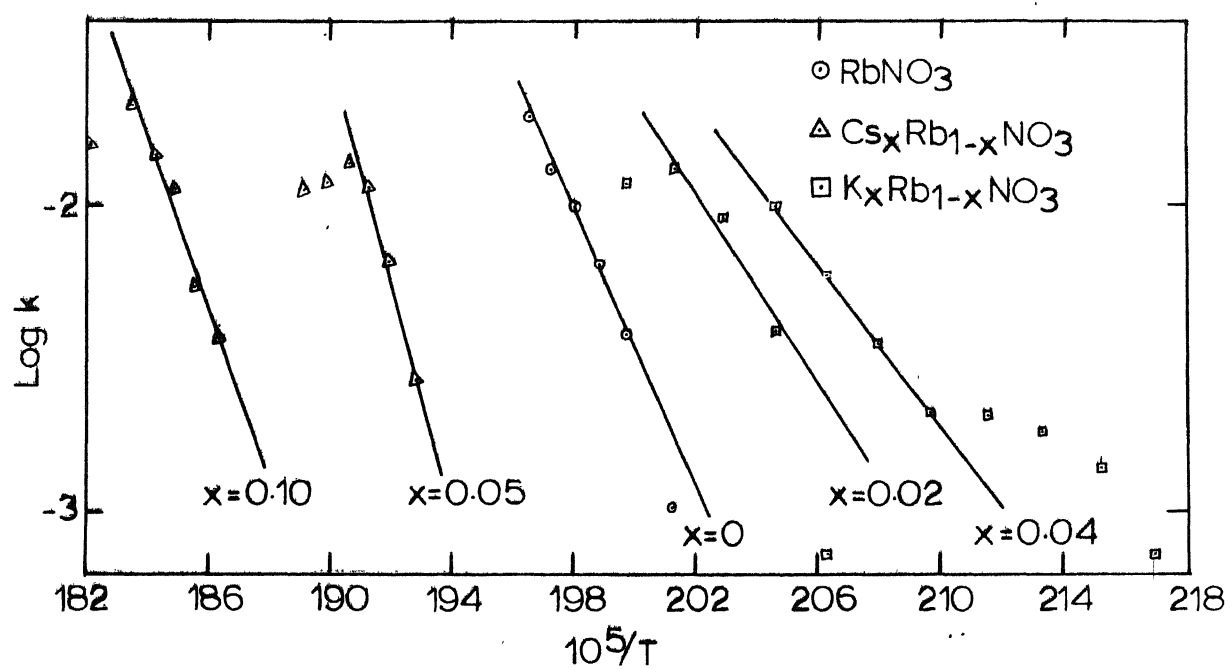
Fig. 4.9 Activation energy plots for III ⇌ II transformation.

From the slope of these straight line plots[*] E_a is calculated

using the formula (Appendix B)

$$E_a = 2.303 \ R \times (\text{slope of activation energy plot}).$$

where R is the gas constant. Ea values thus obtained are

listed in table 4 3.

According to Rao and Rao[47] the H and Ea values

obtainable from the DTA study have an uncertainty of $\pm$ 15 %.

The values of activation energies E_a for IV $\rightarrow$ III

transformation, and heats of transition $\triangle$H, for III $\rightarrow$ II

---

* According to Rao et al[65] there is a considerable

controversy regarding the evaluation of k, the first order

rate constant, and Ea from the DTA curves. Inspite of the

controversy it may be reasonable to compare values of E_a in a

related series of systems. Further, obtaining good linear plots

of log k vs I/T serves as a satisfactory criterion for obtaining

meaningful values of Ea[47].

transformation in the case of $RbNO_3$ are in reasonable agreement

with those of Rao and Rao[47] (Section 1.6). The activation

energy value for III $\longrightarrow$ II transformation

in $RbNO_3$ as determined here, does not agree with

that of Rao and Rao[47]. The larger value for activation energy

observed here is consistent with the reconstructive nature of

transition at III $\longrightarrow$ II, as reported by Kennedy[5].

The value of ΔH at the IV $\rightleftharpoons$ III transition seems

to decrease with solid solution formation. It may be recalled

that this transition temperature is affected only slightly by

ionic substitution. On the other hand, at the III $\rightleftharpoons$ II

transition, which is affected markedly by ionic substitution ΔH

decreases and E_a increases on replacing Rb^+ by Cs^+. Replacement

of Rb^+ by K^+ has an opposite effect.

4.3 Thermal Expansion Measurement by a Dilatometer

Figs 4.10 and 4.11 show the plot of $\frac{\Delta l}{l}$ vs (Appendix F)

temperature for the $Cs_xRb_{1-x}NO_3$ and $K_xRb_{1-x}NO_3$ systems. The

coefficients of linear thermal expansion (on heating) vs

temperature are shown in figs 4.12 and 4.13. From figs 4.10 and

4.11 it can be seen that, (i) the anomalous thermal expansion at
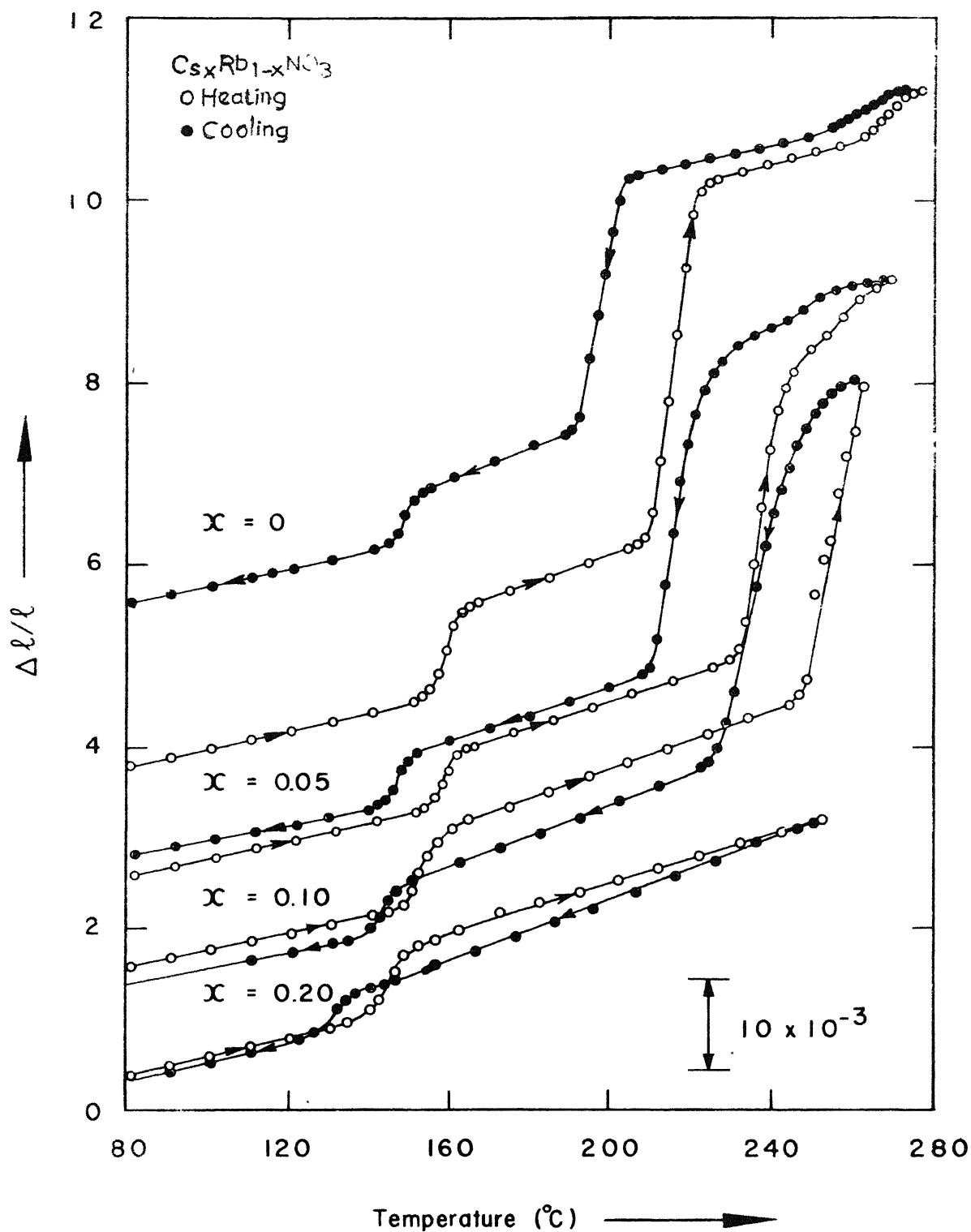
Fig. 4.10 Thermal expansion as a function of temperature for the $Cs_xRb_{1-x}NO_3$ system.
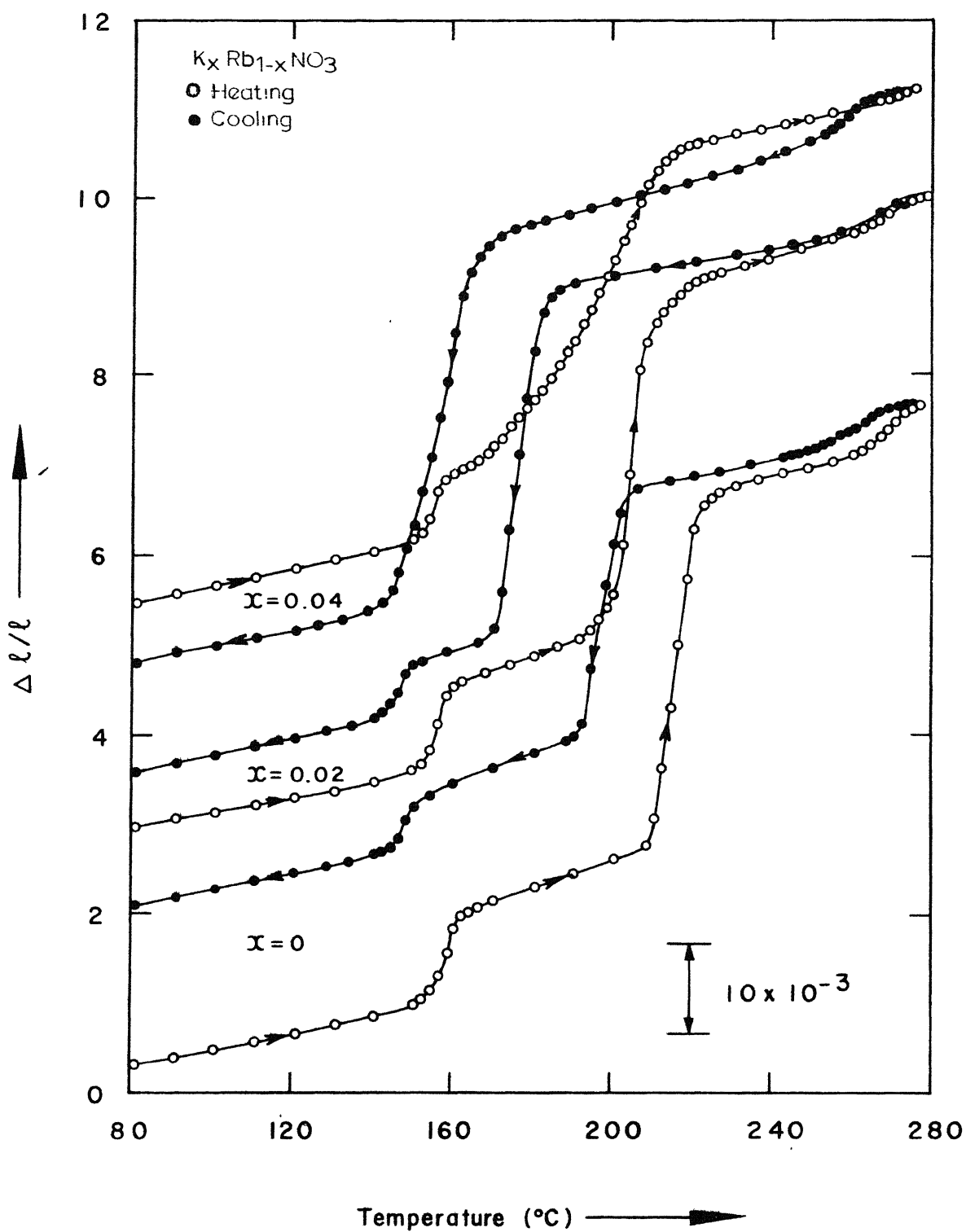
Fig. 4.11 Thermal expansion as a function of temperature for the $K_xRb_{1-x}NO_3$ system.
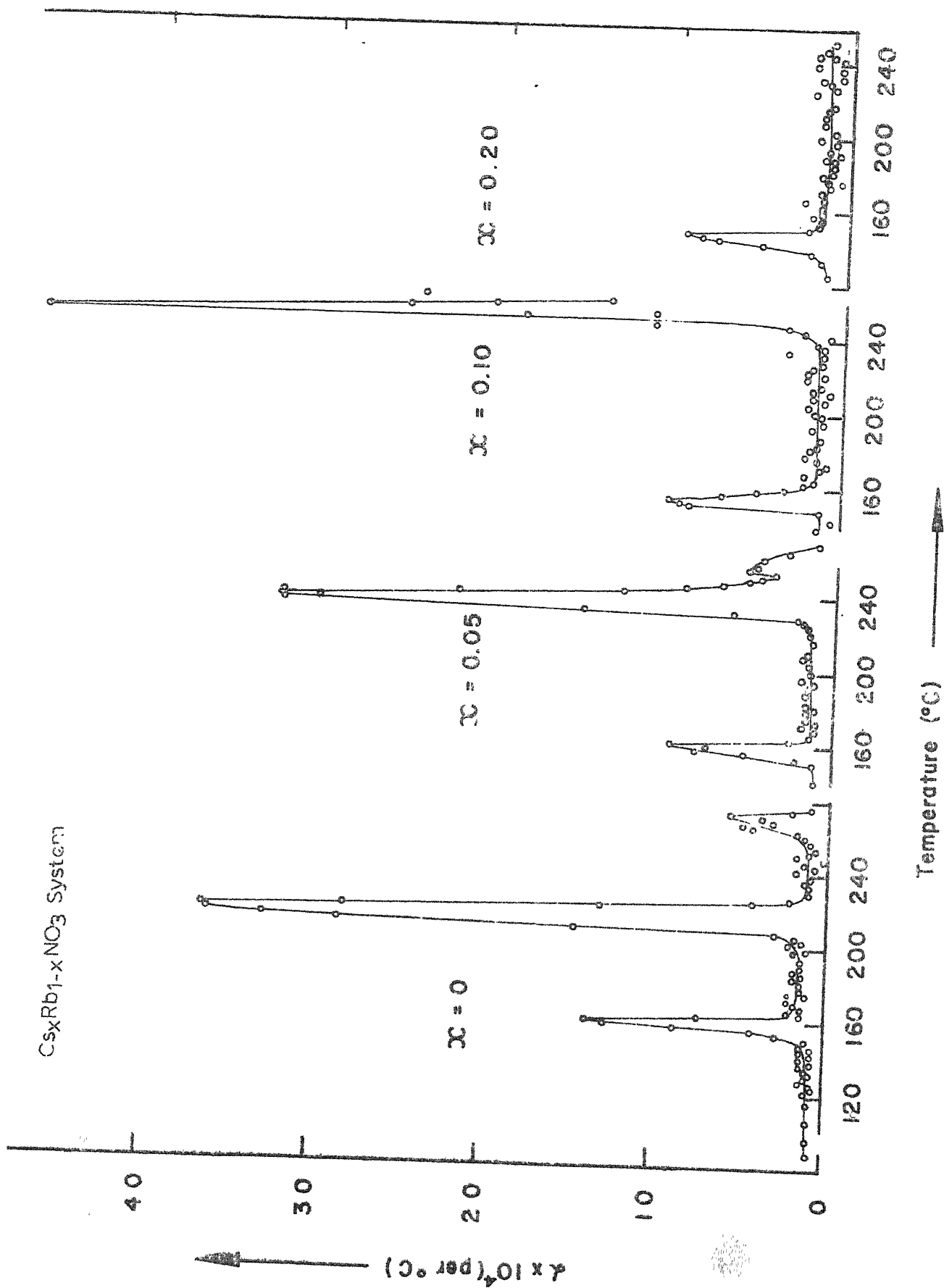
Fig. 4.12: Coefficients of linear thermal expansion as a function of temperature for $Cs_xRb_{1-x}NO_3$ system.

$K_x Rb_{1-x} NO_3$ System

$x = 0$

$x = 0.02$

$x = 0.04$

$d \times 10^7 (\text{per} \,^\circ C)$

Temperature ($^\circ$C)
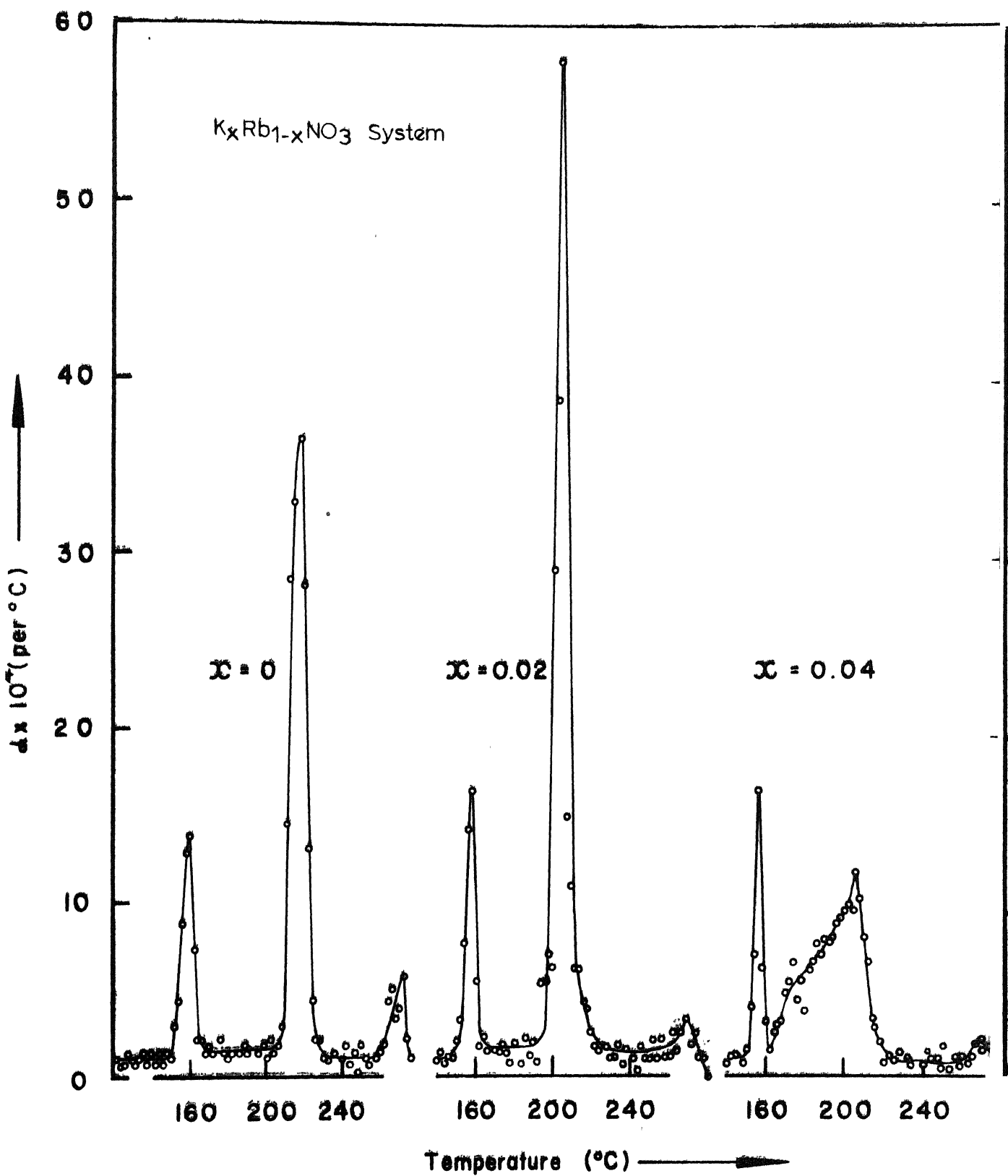
III ⟶ II transition is larger than that at the IV ⟶ III, which in turn is larger than that at the II ⟶ I phase change (table 5.2) (ii) with increasing Cs^+ or K^+ concentration, the anomalous expansions, at IV ⟶ III and III ⟶ II phase changes, decrease during heating and increase during cooling, (iii) IV ⟶ III transition temperature decreases slightly with increasing Cs^+ or K^+ concentrations, transition temperature III ⇌ II shifts substantially to high temperature side in $Cs_xRb_{1-x}NO_3$ system and in the opposite direction in $K_xRb_{1-x}NO_3$ system, (iv) transition III ⇌ II is increasingly getting smeared out with increasing Cs^+ or K^+ concentrations, (v) high temperature end of phase II stays nearly constant in both $(Cs, Rb)NO_3$ and $(K, Rb)NO_3$ systems; its low temperature end shifts with concentration to higher temperatures in $(Cs, Rb)NO_3$ system and in the opposite direction in $(K, Rb)NO_3$ system. Hence in fig 4.10 phase II is getting squeezed out and in fig 4.11 it gets widened. Phase III is gradually vanishing with concentration in $(K, Rb)NO_3$ system — faster during cooling than during heating. It is getting widened in $(Cs, Rb)NO_3$ system with concentration and (vi) the temperature at which the material becomes plastic decreases with concentration of Cs^+ or K^+. It is probably due to the lowering of the melting point.

These conclusions are in confirmity with those in sections 4.1 and 4.2.

4.4 Thermal Expansion Study by X-ray Diffraction.

The plots of lattice parameters as a function of temperature in the range $25 - 300^{\circ}C$ are shown in figs 4.14 to 4.17 for $RbNO_3$ and its solid solutions. (Appendix G) The lattice parameter data of $RbNO_3$ given in fig 4.14 are replotted in fig 4.15 where the reduced lattice parameters represent one formula unit of $RbNO_3$ in each phase. Thus, $\frac{a_{IV}}{\sqrt{6}}$ and $\frac{c_{IV}}{\sqrt{3}}$ are plotted in place of a_{IV} and c_{IV}, the hexagonal lattice parameters of phase IV, and $\frac{a_{II}}{\sqrt[4]{2}}$ and $\frac{c_{II}}{\sqrt{6}}$ in place of the hexagonal parameters a_{II} and c_{II} of phase II. The interrelationships between the unit cells of different phases are discussed in section 5.1.3.

It can be seen from fig 4.14 that c and a in phase IV, a in phase III and c in phase II expand with temperature whereas a in phase II contracts with temperature. Fig 4.15 shows that in phase IV, $\frac{a_{IV}}{\sqrt{6}}$ expands while $\frac{c_{IV}}{\sqrt{3}}$ contracts near the transformation temperature to become equal to a_{III} which expands with temperature. a_{III} represents the lattice constant of phase III. In phase II, $\frac{a_{II}}{\sqrt[4]{2}}$ contracts with temperature, whereas $\frac{c_{II}}{\sqrt{6}}$ expands.
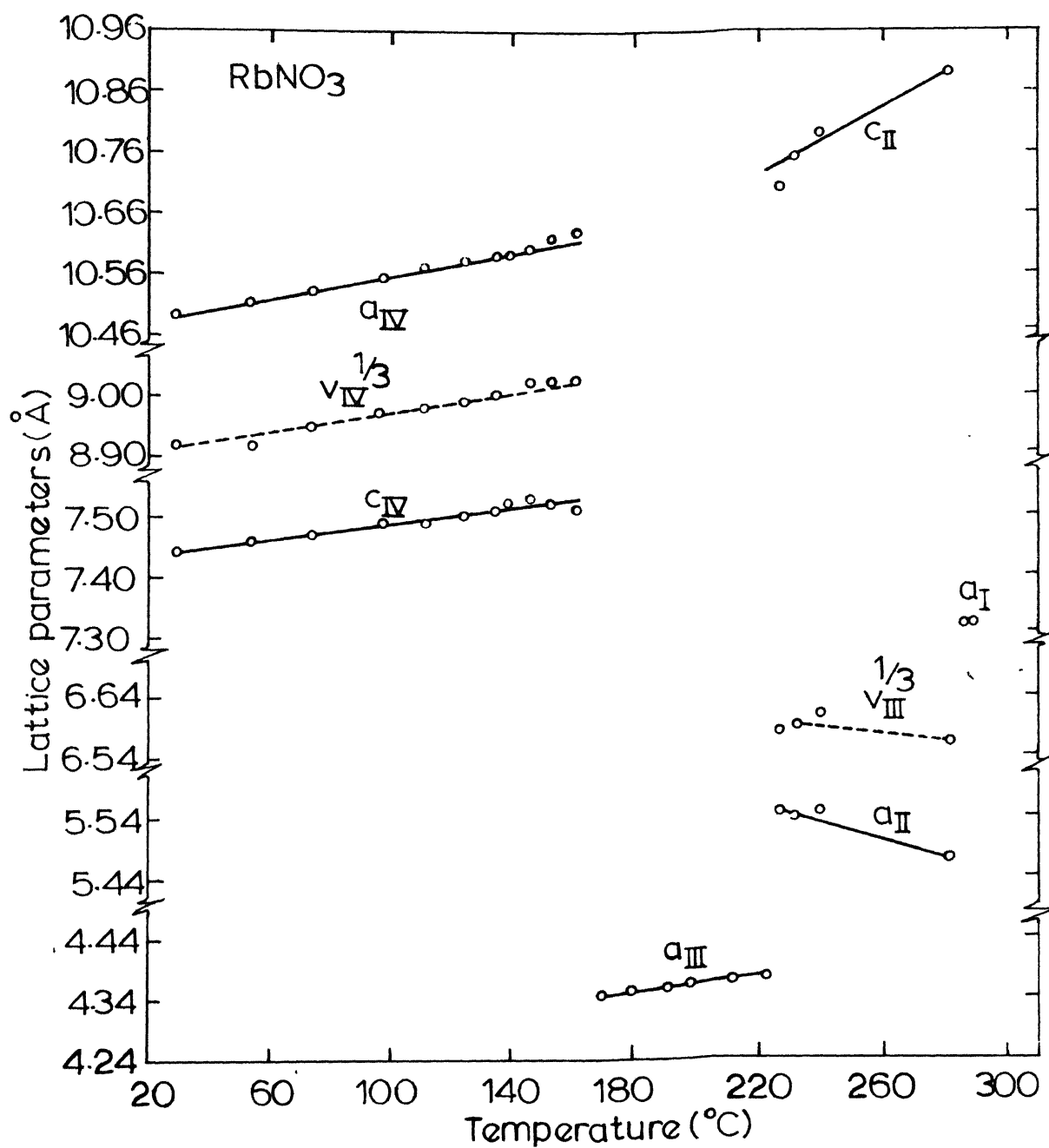
Fig. 4.14: Variation of lattice parameters of the four solid
phases of $RbNO_3$ with temperature.
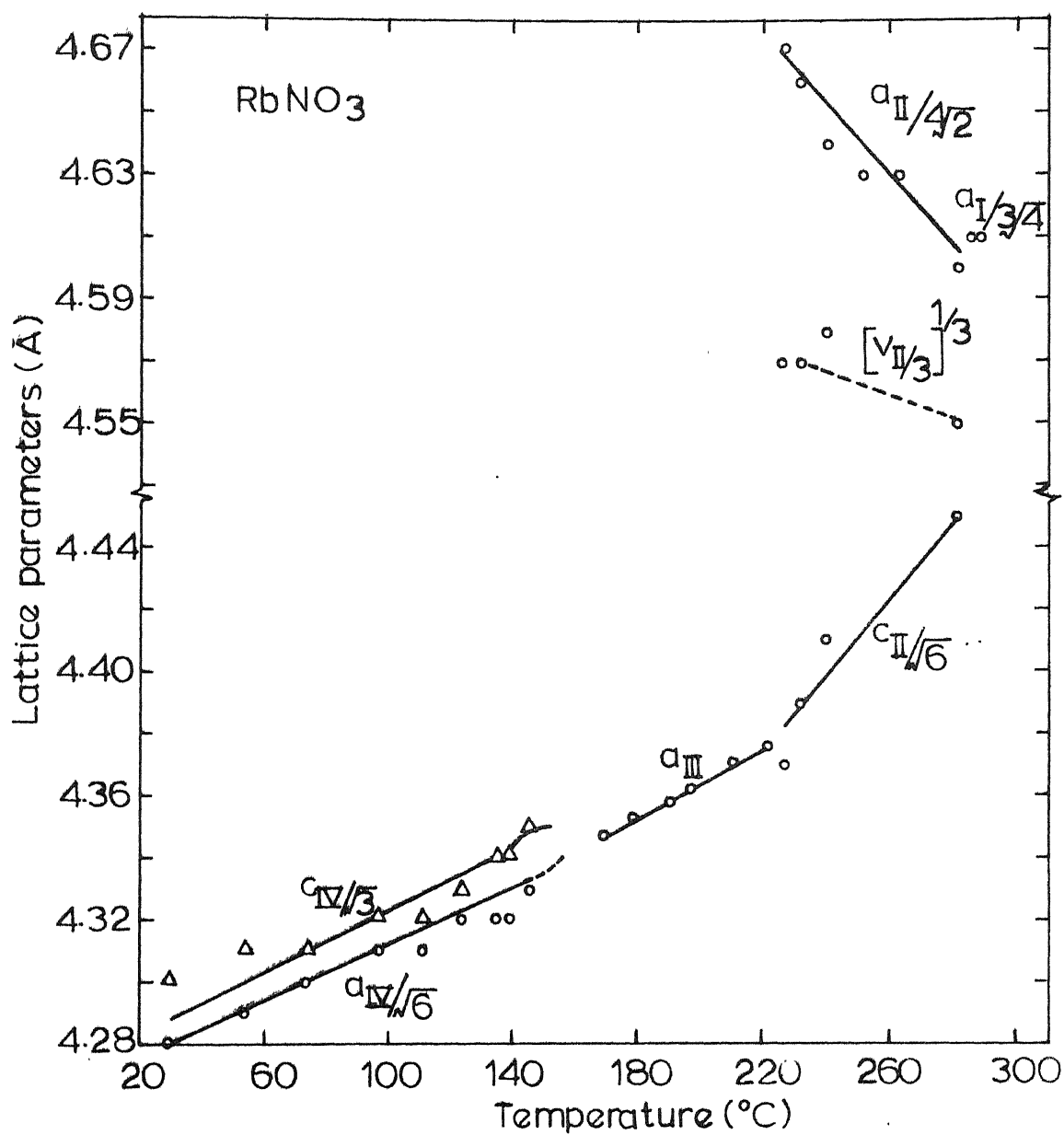
4.15 Temperature dependence of reduced lattice parameters of $RbNO_3$. The lattice parameters of each phase are reduced to include one formula weight of $RbNO_3$.

Table 4.4 compares the lattice parameter values of different authors with those found in the present study.

Table 4.4 Lattice parameters of different phases of $RbNO_3$ as studied by different authors

Phase	Type of study	Authors	Lattice parameters	No. of formula units per unit cell	Lattice parameters of present study
IV	Single crystal	Brown & McLaren[4]	Trigonal: a = 10.51Å c = 7.43Å	9	a = 10.51Å c = 7.43Å
-do-	-do-	Pauling & Sherman[88]	Hexagonal: a = 10.45Å c = 7.38Å	-do-	
III	-do-	Brown & McLaren[4]	Cubic: a = 4.36Å	1	a = 4.36Å *
-do-	Powder photograph	U.Korhonen[11]	Cubic a = 8.74Å	4	
II	Powder diffractometry	Brown & McLaren[4]	Tetragonal: a=6.19 Å c=8.74 Å	4	
-do-	-do-	-do-	Hexagonal: a = 5.48Å c =10.71Å	3	a = 5.51Å c = 10.74 Å
I	Powder diffractometry	Brown & McLaren[4]	Cubic: a = 7.32 Å	4	a = 7.30 Å

* This value of lattice constant does not exclude the possibility of the cell of double this size, proposed by Korhonen[11] since the nitrogens and oxygens do not contribute much to the X-ray reflections and hence not identified here.

The variations of reduced lattice parameters with temperature for $Cs_{0.05}Rb_{0.95}NO_3$ and $K_{0.04}Rb_{0.96}NO_3$ are shown in figs 4.16 and 4.17 respectively. The data are similar to those recorded for $RbNO_3$. A widening of the temperature range of stability of phase III with the addition of Cs^+ and a narrowing of this range with the addition of K^+ is quite apparent from these figures The lattice parameters are observed to vary non-linearly in the close vicinity of the phase transformations (see e.g. the II $\longrightarrow$ I transformation in $K_{0.04}Rb_{0.96}NO_3$ in fig. 4.17).

The thermal expansion behaviour of phase IV of $RbNO_3$ (fig 4.14) is in confirmity with the dilatometric results of Dantsiger and Fesenko[26] (fig 1.6) who find that single crystals of $RbNO_3$, in phase IV, expand both along the trigonal axis as well as in a direction perpendicular to it (section 1.5). However, in contrast to the contraction along both the axes of phase IV at IV $\longrightarrow$ III transformation and also in phase III reported by Dantsiger and Fesenko[26], the present results indicate that one of the axes of phase IV expands and the other contracts at IV $\longrightarrow$ III transformation and the unit cell edge expands in phase III. These results confirm those of Kennedy[17] who carried out X-ray diffraction study of single crystals of $RbNO_3$. Due to the disruptive nature of the III $\longrightarrow$ II transformation the axial length changes recorded by Dantsiger and
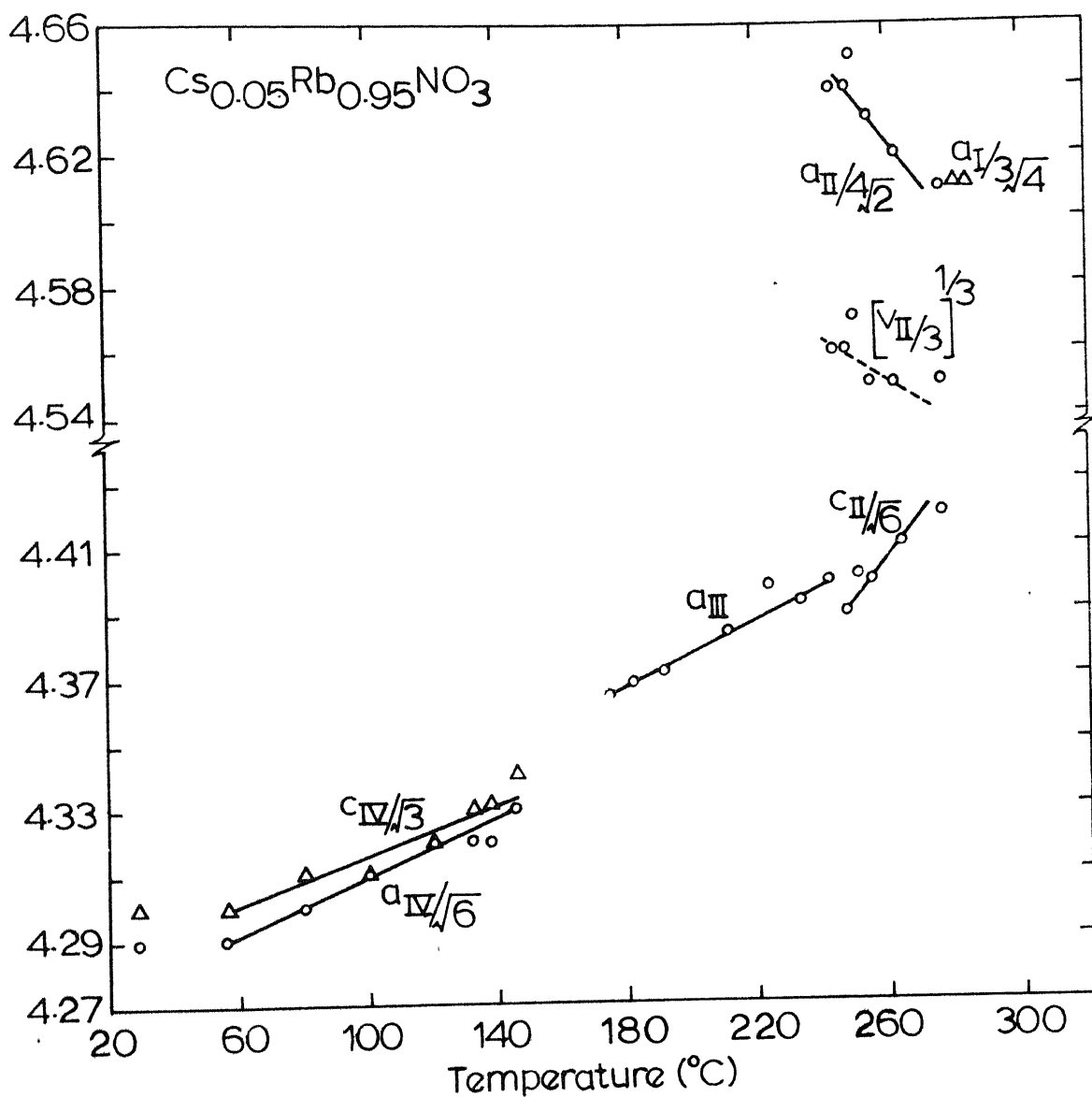
Fig. 4.16: Temperature dependence of reduced lattice parameters of $Cs_{0.05}Rb_{0.95}NO_3$. The lattice parameter of each phase are reduced to include one formula weight.
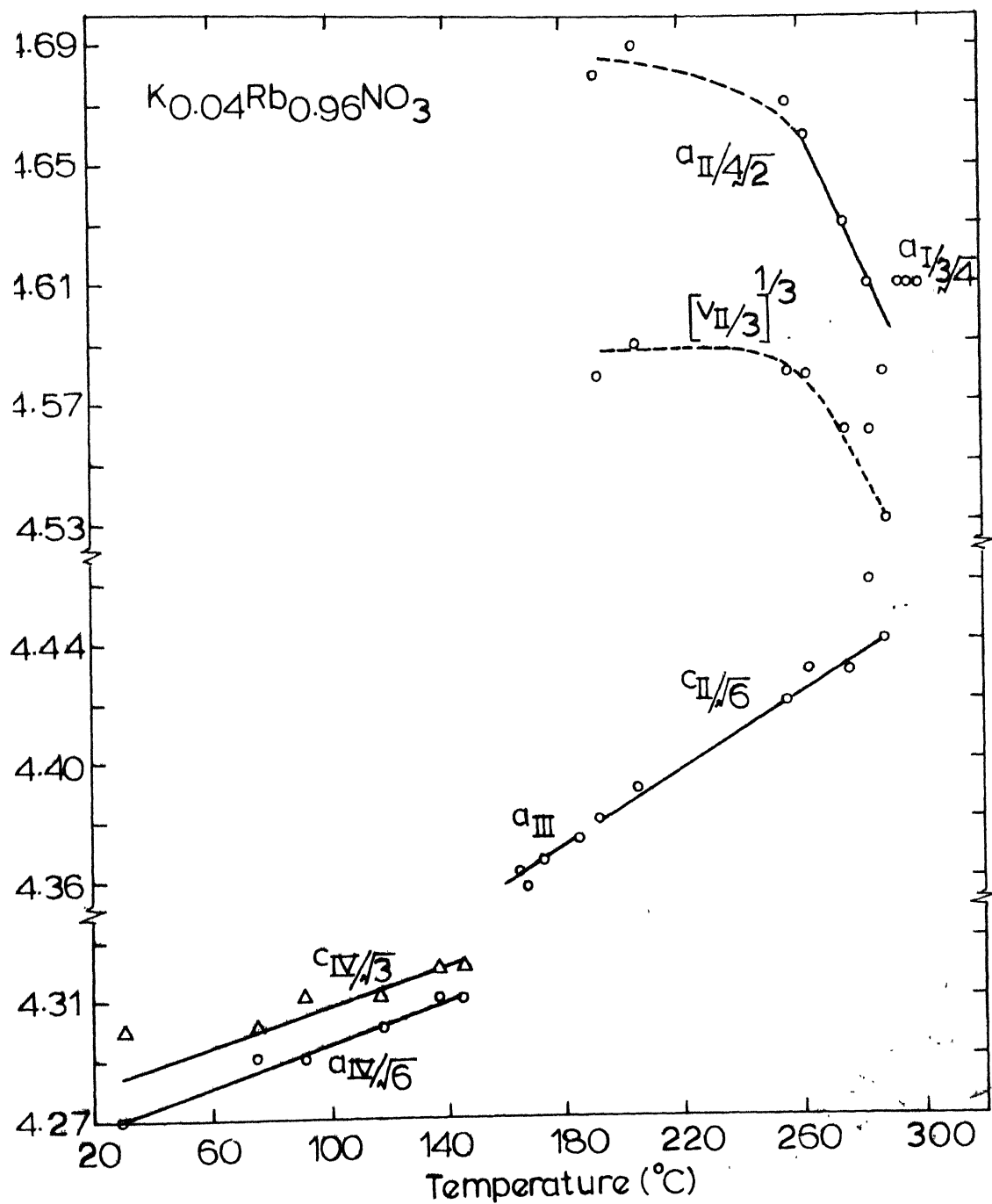
Fig. 4.17 Temperature dependence of reduced lattice parameters of $K_{0.04}Rb_{0.96}NO_3$. The lattice parameters of each phase are reduced to include one formula weight.

Fesenko[26], using a dilatometer, at III $\longrightarrow$ II transformation and above cannot be easily compared with the x-ray diffraction study and also the dilatometric study of the polycrystalline material (section 4.3).

The coefficients of linear thermal expansion and percent changes in lattice spacings calculated from the lattice parameter values (figs.4 15 to 4.17) are shown in tables 5.1 and 5.2 respectively.

4.5 Infra-red Absorption

The infrared absorption spectra of RbNO$_3$ at different temperatures are shown in figs 4.18 and 4.19. It is seen from these figures that three components are observed in each of the regions of the fundamental modes ν_1 (1036 to 1056 cm^{-1}) and ν_4 (708 to 764 cm^{-1}). Figs 4.18 and 4.20 show that three components are also observed for the mode ν_2 (816 to 838 cm^{-1}) in the room temperature phase. The positions and relative intensities of these modes in different phases of RbNO$_3$ are listed in table 4.5.

As the temperature is raised the fundamental absorption peaks in phase IV slightly diminish in intensity as well as show a little shift to the low frequency side (figs 4.18 and 4.19 and Table 4.5).
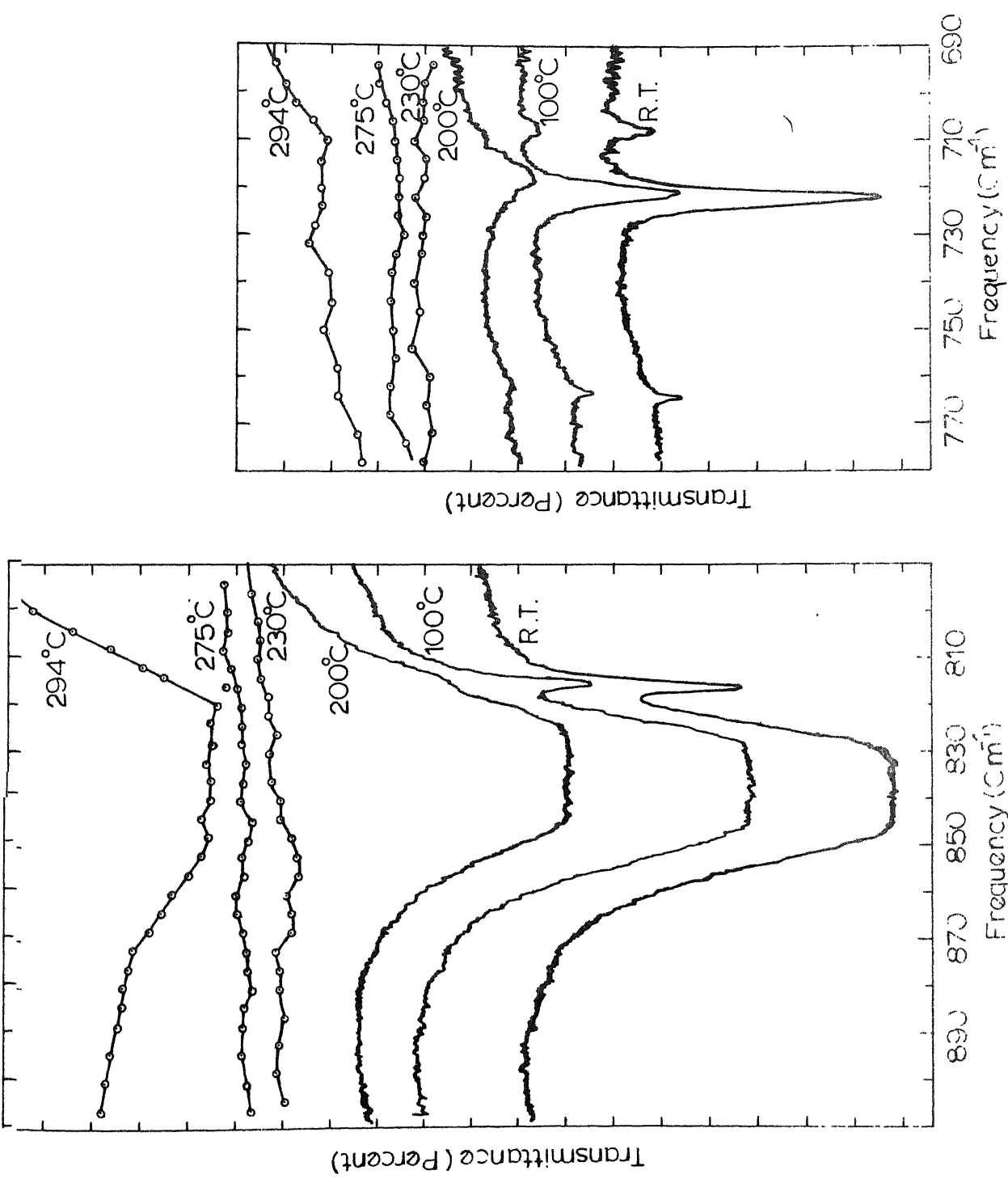
Fig. 4.18: Changes with temperature both in intensity and the number of components of fundamental vibration modes ν_2 (left) and ν_4 (right) of NO_3^- ion in $RbNO_3$.
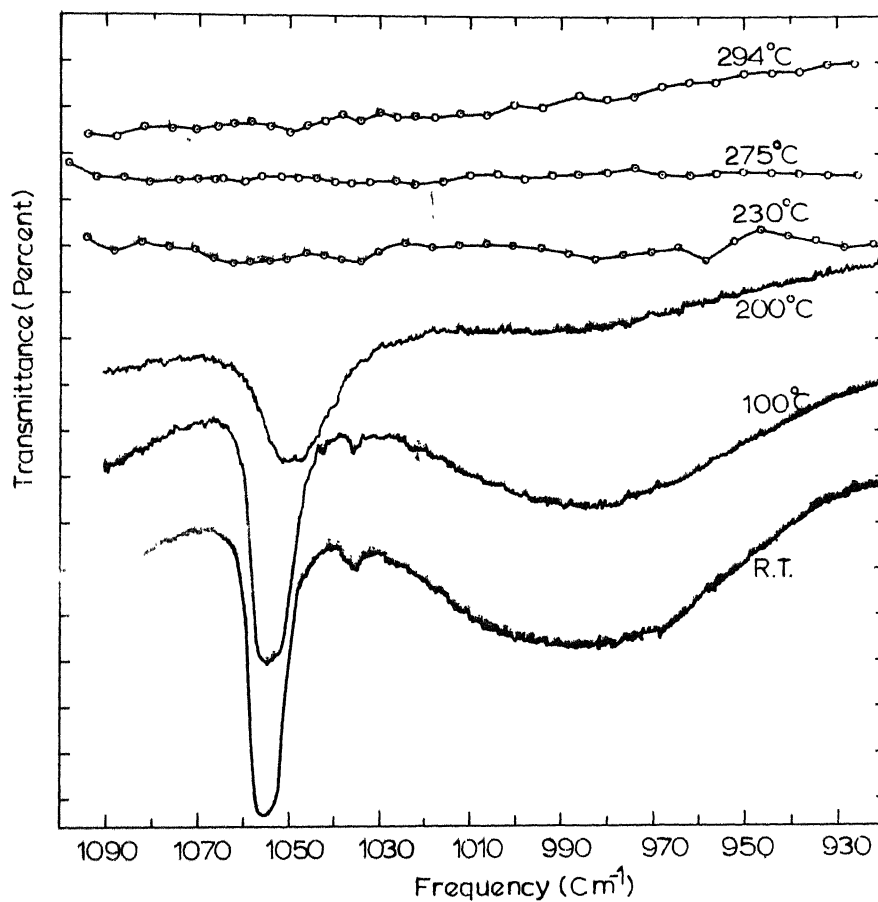
Fig. 4.19 Changes with temperature both in the intensity and
the number of components of fundamental vibration
mode ν_1 of NO_3^- ion in $RbNO_3$.

TABLE 4.5: Fundamental modes of vibration of NO_3^- ion in different phases of $RbNO_3$

Phase	Temp. (°C)	ν_4 (cm^{-1})			ν_2 (cm^{-1})		ν_1 (cm^{-1})		
		Component 1	Component 2	Component 3	Component 1	Component 2,3	Component 1	Component 2	Component 3
IV	R.T	708W	722ms sharp	764 5V.W. sharp	816.5ms sharp	838VS broad	1036V.W. broad	1054S sharp	1056S sharp
IV	100	707V.W.	721mV sharp	763.5V.W.	815 5mW.	837V S. broad	1036V.W.	1053.5S sharp	1055S sharp
III	200	—	718m broad	761.5 V.V.W.	—	834V.S. broad	—	1048ms broad	1051.5ms broad
	230	—	—	—	—	—	—	—	—
II	275	—	—	—	—	—	—	—	—
I	294	710? broad	722 broad	—	—	832V S broad	—	1050V.V.W.	—

Abbreviations: W = weak

V.W. = very weak

V.V.W. = very very weak

m.W. = medium weak

mS = medium strong.

S = strong.
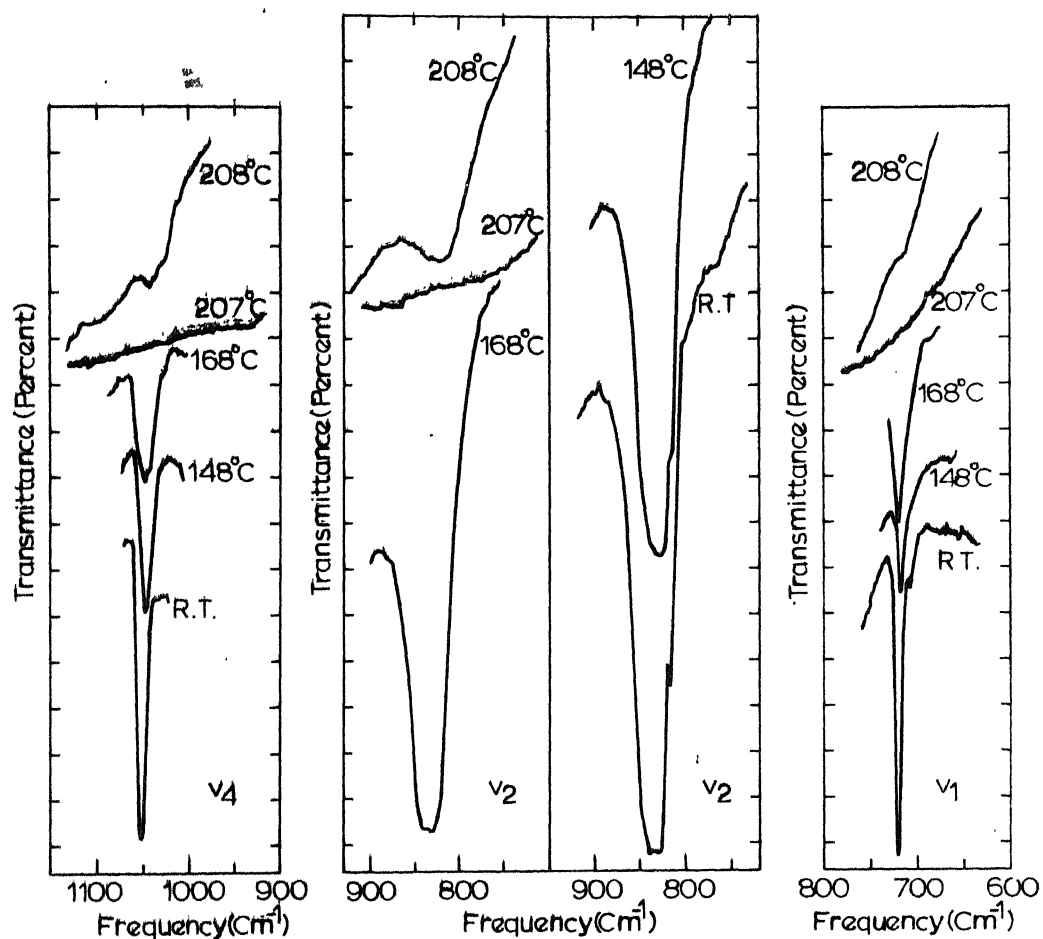
Fig. 4.20 Variation with temperature in the intensity of fundamental modes ν_1, ν_2 and ν_4 of NO_3^- ion in $RbNO_3$. At $208^{\circ}C$ the traces shown were obtained after attenuation of the reference beam.

In phase III each mode has only one component (figs 4.18 and 4.19). As the temperature is raised the fundamental modes ν_1, ν_2 and ν_4 in phase III go on diminishing in intensity. At 207°C their intensity has gone down so much (fig 4.20) that to observe them in this phase the reference beam in the double-beam spectrophotometer has to be attenuated using Perkin-Elmer attenuator attachment A comparatively large shift in frequency and a slight increase in intensity at IV $\rightarrow$ III transformation are also observed.

As the temperature is raised above 220°C phase II appears As already pointed out, the fundamental absorption peaks became too weak to be observed above 207°C. Therefore infrared spectra in phase II at different constant temperatures in the range 230°C upto 280°C were obtained using the techniques described by Greenberg and Hallgren[52] as well as by a suitable attenuation of the reference beam.

At a constant temperature two records of transmittance vs frequency were obtained on the chart paper - one with the shutter of the sample beam open and the other with the shutter of the sample beam closed The difference of transmittance readings, corresponding to each record, was plotted as a function of frequency. In figs 4.18 and 4.19 the curves at temperatures 230°C, 275°C and 294°C were obtained in this manner.

The above method was adopted by Greenberg and Hallgren[52]
on the following reasoning. When the sample beam shutter is
closed the detector is activated by thermal radiation from
the infrared cell and the pellet specimen. The specimen may
also have specific emission at those wave lengths at which
there is maximum absorption. The fact that there are
relatively high specific emissions from the specimen is
to be expected since $h\nu$ is of the same order of magnitude
as kT.

It is evident from figs 4.18 and 4.19 that no
fundamental absorption peaks $(\nu_1, \nu_2 \text{ and } \nu_4)$ are
seen at 230°C and 275°C i.e. in phase II.

When temperature is raised to 285°C phase I appears.
Figs 4.18 and 4.19 (at 294°C) show that the absorption peaks
at fundamental frequencies reappear. The fundamental
absorption peaks started appearing to a small extent at
285°C but became prominent at 290°C and 294°C (not shown
in figures).

In the solid solutions the spectra at room
temperature (figs 4.21 and 4.22) show that ν_1, ν_2 and ν_4
frequencies shift to lower frequencies with Cs^+ impurity
(larger cation size) and to higher frequencies with K^+ impurity
(smaller cation size). Table 4.6 gives a comparative study
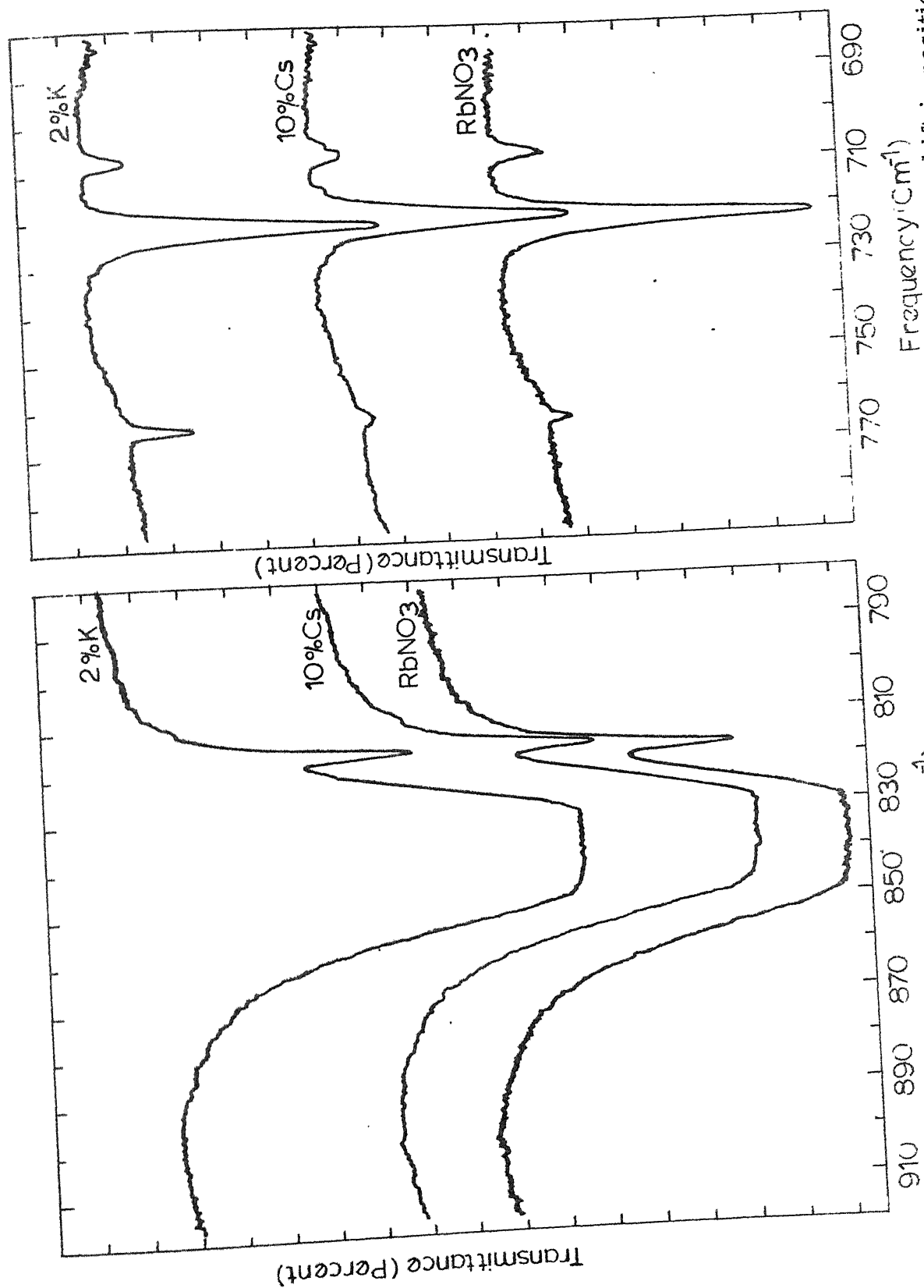
Fig. 4.21: Fundamental modes of vibration ν_2 (left) and ν_4 (right), of NO_3 group in $RbNO_3$, shift in position as the cation size is changed in the solid solutions $Cs_{0.10}Rb_{0.90}NO_3$ and $K_{0.02}Rb_{0.98}NO_3$. Traces at room temperature are shown.
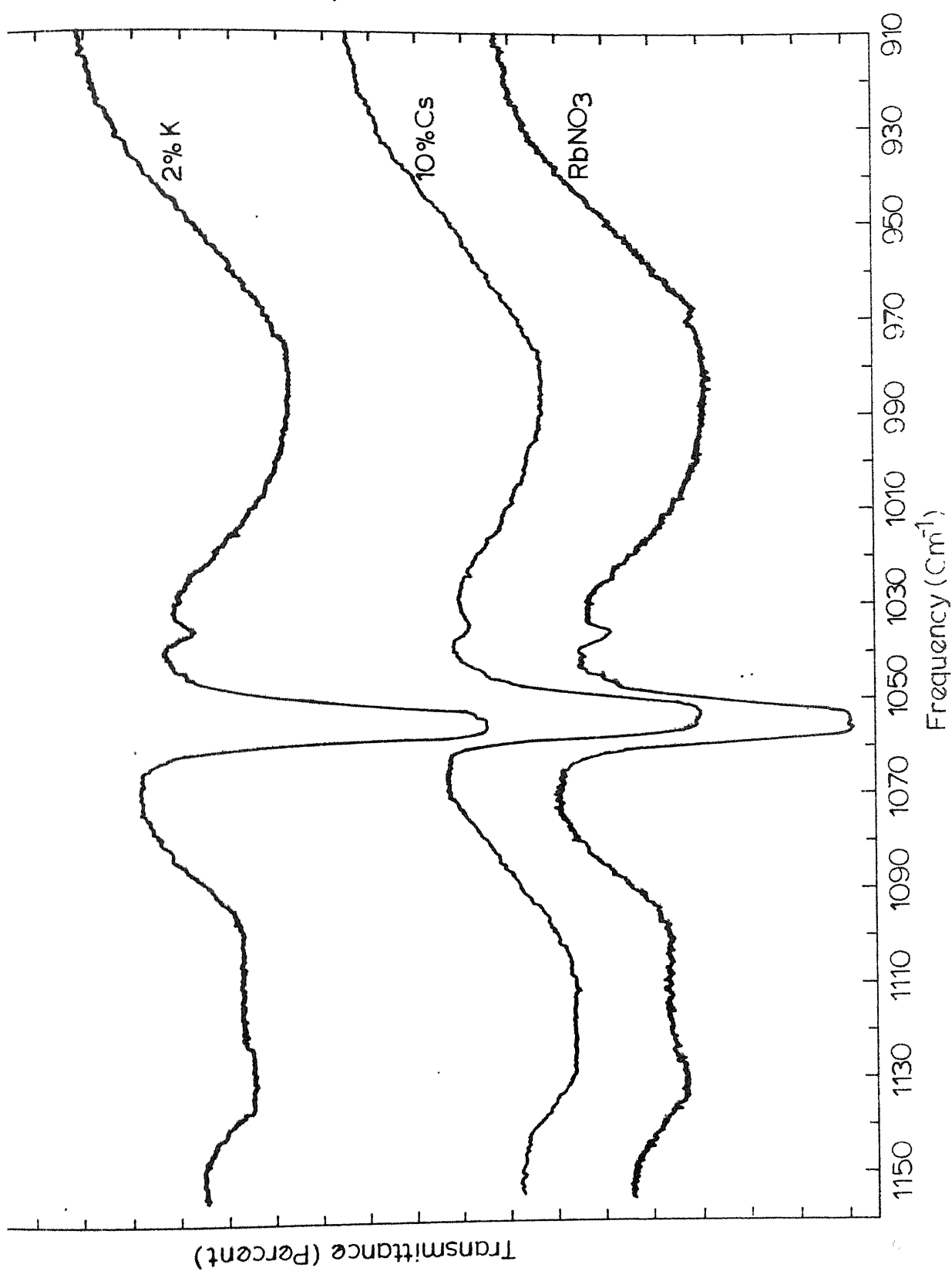
Fig. 4.22: The traces show shift in positions of the fundamental vibration mode v_1 at room temperature due to substitution of Cs^+ or K^+ ions for the cation in $RbNO_3$.

TABLE 4.6: NO_3^- ion fundamental frequencies (ν cm^{-1}) at room temperature for RbNO$_3$ and its solid solutions.

Specimen	ν_4			ν_2		ν_1		
	Component 1	Component 2	Component 3	Component 1	Component 2	Component 1	Component 2	Component 3
RbNO$_3$	708W sharp	722ms sharp	754.5V.W. sharp	816.5ms sharp	838V S broad	1035.5V.W. broad	1054S sharp	1056S sharp
Cs$_{0.1}$Rb$_{0.9}$NO$_3$	707W	721ms	763V.S.	815.5ms sharp	837V S. broad	1035V.W. broad	1053S sharp	1055.5S sharp
K$_{0.02}$Rb$_{0.98}$NO$_3$	708W	722.5ms	765W sharp	816.5ms sharp	838V S broad	1056V.W. broad	1053S sharp	1056S sharp

Abbreviations are same as in TABLE 4.5.

of fundamental modes of NO_3^- ion in the solid solutions at room temperature.

In general the intensities of absorption peaks of fundamentals reduce by Cs^+ substitution and get enhanced during K^+ substitution (figs 4.21 and 4.22).

Chapter 5

DISCUSSION

5.1 Thermal Properties:

5 1.1 Thermal Expansion Coefficients.

The slopes of the straight line portions of the dilato-
metric curves, presented in figs. 4.10 and 4.11, represent the
coefficients of linear thermal expansion of the stable phases of
RbNO$_3$ and its solid solutions   These are summarized in table 5.1.
Cleaver et al[2] have given the volume thermal expansion coefficients
for phases IV and III of RbNO$_3$ One third values of these coefficients
are listed for comparison with those of the present study.   Also
included in table 5.1 are coefficients of linear thermal expansion
of the lattice spacings and $\frac{1}{3} \frac{\Delta V}{V}$ per $^{\circ}$C from the X-ray data.   The
coefficients of expansion of lattice constants in phase IV of RbNO$_3$
are reported by Kennedy et al[17] (section 1.5).   The corresponding
values obtained in the present study (Table 5.1) are in reasonable
agreement with those.

The α_a and α_c values of the hexagonal phase IV are nearly
the same and close to the value of linear thermal expansion coeffi-
cient obtained from the dilatomatric measurement, whereas the α
values of the hexagonal phase II are strongly anisotropic.   The α
values determined from the lattice parameters are in fair agreement

- 83 -

TABLE 5.1 Coefficients of linear thermal expansion in different phases of $RbNO_3$ and its solid solutions.

Phase	Method of determination	Coefficient of linear thermal expansion.	$RbNO_3$ Literature values	$RbNO_3$ Present study	$Cs_xRb_{1-x}NO_3$ x=0.05	x=0.10	x=0.20	$K_xRb_{1-x}NO_3$ x=0.02	x=0.04
IV	Dilatometry	$\alpha \times 10^6 (°C)^{-1}$	70(2)	102 (92)	97 (83)	93 (83)	99	86	98 (98)
	X-ray diffraction	$\alpha_a \times 10^6 (°C)^{-1}$	$97.1^{(17)}$	84	104				81
		$\alpha_c \times 10^6 (°C)^{-1}$	$101.5^{(17)}$	97	86				78
		$\frac{1}{3}\frac{\Delta V}{V} \times 10^6$ $(°C)^{-1}$		101					
III	Dilatometry	$\alpha \times 10^6 (°C)^{-1}$	$113^{(2)}$	162 (79)	145 (152)	130	128	156	154
	X-ray diffraction.	$\alpha_a \times 10^6 (°C)^{-1}$	$85^{(17)}$	131	117				114
		$\frac{1}{3}\frac{\Delta V}{V} \times 10^6$ $(°C)^{-1}$		135					

(TABLE 5.1 Contd.)

Phase	Method of determination	Coefficient of linear thermal expansion.	RbNO$_3$		Cs$_x$Rb$_{1-x}$NO$_3$			Cs$_x$Rb$_{1-x}$NO$_3$		
			Literature values	Present study	x=0.05	x=0.10	x=0.20	x=0.02	x=0.02	x=0.04
II	Dilatometry	$\alpha \times 10^6(°C)^{-1}$	117	(99)	(181)			122		96 (100)
	X-ray diffraction	$\alpha_a \times 10^6(°C)^{-1}$		-265	-288					
		$\alpha_c \times 10^6(°C)^{-1}$		283	304					142
		$\frac{1}{3}\frac{\Delta V}{V} \times 10^6(°C)^{-1}$		-85						
I	Dilatometry	$\alpha \times 10^6(°C)^{-1}$		(55)	(143)					(110)

Dilatometric values given in paranthesis are obtained from cooling curves. The values of rel quoted here are $\frac{1}{3}$ of the coefficient of volume expansion.

with the dilatometric results in phase IV (where the anisotropy

of thermal expansion is small) and in phase III (which is cubic)

but not in phase II, due to the large anisotropy of axial expansion.

The α value for phase I recorded in table 5.1 may be

smaller than the real value, since the expansion here is likely

to be partly offset by the plastic deformation of the sample

under the weight of the quartz tube carrying the optical lever.

It may be recalled that this phase exists over a narrow temperature

range just below the melting point.

5.1.2 Volume and Length Changes at Phase Transitions:

Table 5.2 gives percent changes in length and lattice

spacings, at the transition points, from dilatometry (figs. 4.10

and 4.11) and X-ray data (figs 4 14 to 4.17).

The length changes observed here correspond fairly

well with the volume changes reported in the literature[2] at

the various transition points, except for the value reported by

Ubbelohde[2] at the IV $\rightarrow$ III transition. Lattice parameter

changes were reported by Kennedy et al[17] at the IV $\rightarrow$ III

transition and these values agree with the present results in

sign but not in magnitude The difference in the values of the

lattice parameter changes observed at the transformation, of the

TABLE 5.2 Percent changes in length at the phase transitions in RbNO₃ and its solid solutions.

Transition	Method of determination	Length change	RbNO₃ Literature values	RbNO₃ Present study	Cs$_x$Rb$_{1-x}$NO₃ x=0.05	Cs$_x$Rb$_{1-x}$NO₃ x=0.10	Cs$_x$Rb$_{1-x}$NO₃ x=0.20	K$_x$Rb$_{1-x}$NO₃ x=0.02	K$_x$Rb$_{1-x}$NO₃ x=0.04
IV to III	Dilatometry	$\Delta l/l$(%)	$1.7^{[2]}, 0.7^{[40]}$	0.95	0.64 (0.53)	0.81 (0.66)	0.64 (0.44)	0.95 (0.62)	0.70
	X-ray diffraction	$\Delta a/a$(%)	$0.61^{[41]}, 1.7^{[47]}$ $+0.78^{[17]}$	0.23					0.97
		$\Delta c/c$(%)	$-0.70^{[17]}$	-0.12					0.70
		$\frac{1}{3}\frac{\Delta V}{V}$(%)		0.05					
III to II	Dilatometry	$\Delta l/l$(%)	$3.33^{[2]}, 4^{[47]}$	3.96 (2.75)	3.40 (3.60)	3.56 (4.10)		3.96 (3.96)	3.60 (4.10)
	X-ray	$\Delta a/a$(%)		6.67	5.80				7.10
	diffraction	$\Delta c/c$(%)		0.07	-0.40				0.14
		$\frac{1}{3}\frac{\Delta V}{V}$(%)		4.90					

(TABLE 5.2 Contd.)

Transition	Method of determination	Length change	RbNO₃		Cs$_x$Rb$_{1-x}$NO$_3$			K$_x$Rb$_{1-x}$NO$_3$	
			Literature value	Present study	x=0.05	x=0.10	x=0.20	x=0.02	x=0.04
	Dilatometry	$\Delta\ell/\ell(\%)$	0.33[2], (1.62)[47]	0.44 (0.44)	0.46 (0.26)			0.36 (0.46)	0.22 (0.44)
II to I	X-ray diffraction	$\Delta a/a(\%)$		0.24	1.18			0.83	
		$\Delta c/c(\%)$		3.50	1.25				3.86
		$\frac{1}{3}\frac{\Delta V}{V}(\%)$		1.70					

The numbers in brackets under the columns—"Present study" and the solid solutions, represent the values obtained from cooling curves whereas superscripts in brackets denote the reference numbers. The dilatometric values are given as $\Delta V/V(\%)$ in literature. Here only $\frac{1}{3}$ ($\Delta V/V$) are tabulated to compare with the values $\Delta\ell/\ell(\%)$ of the present study. $\Delta a/a$ and $\Delta c/c$ of the present X-ray study are obtained from the reduced lattice parameter plots i.e. fig. 4.15 to 4.17.

present study and those of Kennedy, may be probably due to the reduced lattice parameters plotted here (fig. 4.15). The relatively small axial changes observed at this transition are indicative of a displacive or order-disorder transformation.

On the other hand, the axial changes at the III $\rightarrow$ II and II $\rightarrow$ I are much larger, suggestive of reconstructive phase changes. The kinking and fragmentation of crystals at the III $\rightarrow$ II, reported by Brown and McLaren[4] are no doubt due to the drastic distortion of the crystal lattice. The length changes observed in the present work and the ΔV reported by Ubbelohde[2] at the II $\rightarrow$ I transition are fairly small, in fact, smaller than at the IV $\rightarrow$ III transformation. However, the X-ray data shows substantial changes at the II $\rightarrow$ I transition, though not as large as at the III $\rightarrow$ II phase change. The reason for not recording large length changes with the dilatometer as the X-ray data suggest may be because the sample may have become plastically deformed.

5.1.3   Difference in the Thermal Expansion Plots of Dilatometric and X-ray Studies:

Fig. 5.1 shows a plot (continuous curve) of $\Delta \ell/\ell$ vs temperature from the dilatometric data on heating and (broken curve) $\frac{1}{3} \left(\frac{\Delta V}{V} \right)$ vs temperature from the X-ray data, obtained
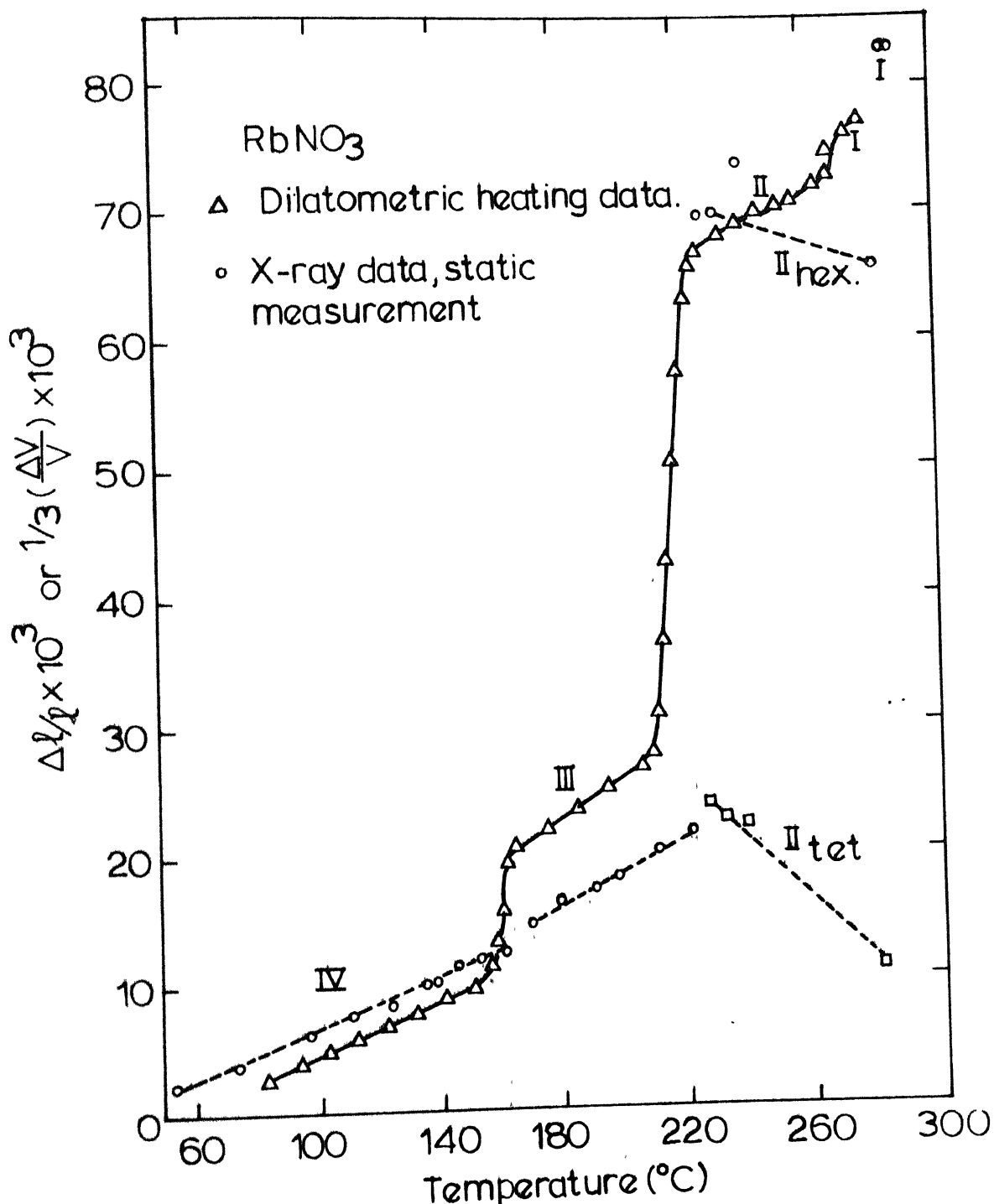
Fig. 5.1 Thermal expansion data from dilatometry ($\Delta \ell/\ell$) during heating and X-ray data (1/3) ($\Delta V/V$), obtained after thermal equilibrium has been attained. I, II, III and IV denote solid phases of $RbNO_3$. X-ray data for the tetragonal (II_{tet}) and hexagonal (II_{hex}) structures of phase II are shown.

at indicated temperatures after equilibration. The symbols I, II, III

and IV represent the different solid phases of $RbNO_3$ (section 1.2).

It is clear from the figure that at IV→III, III→II and II→I

transformations both data show thermal expansion while in phase II

contraction is observed by X-ray measurements and expansion by

dilatometric studies.

It may be seen from fig. 4.14 that, (i) after III→II

transformation there is expansion along the c-axis in phase II

and (ii) contraction along the a-axis of phase II. The result is

that $\frac{1}{3} \left(\frac{\Delta V}{V} \right)$ vs temperature plot declines at higher temperatures

(fig. 5.1). To explain the expansion in phase II (as seen in the

dilatometric curve) it seems reasonable to conclude that, after

III→II transformation, there is some preferred orientation along

the c-axis which shows expansion, as observed by X-ray data.

Therefore, the dilatometer, which measures expansion only in one

direction (i.e along the length of the rod specimen), records

expansion (see also Table 5 1)

For phase II, both the tetragonal and hexagonal cell

parameters are used in plotting $\frac{\Delta V}{V}$ vs temperature in fig 5.1.

It is clear that the large thermal expansion at the III→II

transformation and the smaller one at the II→I transition,

observed in the dilatometric experiment, cannot be accounted for on the basis of a tetragonal cell for phase II   The hexagonal cell on the other hand, gives a satisfactory agreement between the dilatometric and X-ray results.

5.1.4   Co-existence of Phases and Thermal Hysteresis in the

   Transformation Regions:

According to Ubbelohde[69] the phenomena of thermal hysteresis can be readily understood on the basis of coexistence of phases in the transformation regions   For instance, if phase 1 transforms to 2 by a volume expansion, then 2 is growing in a · matrix of 1 and is under compression   In the reverse transformation 1 is in the matrix of 2 and is under tension   So the two paths for the transformation are not identical,which gives rise to hysteresis

The transformation regions for IV $\rightleftharpoons$ III and II $\rightleftharpoons$ I are quite narrow. Very good temperature control is essential to see the coexistence of phases in these regions. Kennedy, Taylor and Patterson[21] have used micro-thermostat and polarised light to see the coexistence of phases in IV $\rightleftharpoons$ III transformation region and have reported a teperature hysteresis of 0.1°C in fresh crystals, The maximum hysteresis was found to be 1°C

after recycling this transformation several times.

In III $\rightleftharpoons$ II transformation coexistence of phases in the transformation region is readily established by X-ray diffraction methods. The (110) reflection is characteristic of phase III and (102) is characteristic of phase II. In the transformation range, the temperature was held constant at different values and (110) and (102) reflections recorded by slow scanning. Fig. 5.2 shows the data for $K_{0.04}Pb_{0.96}NO_3$. At 195°C, only phase III is present. On heating to 208° and 222°C, the intensity of the (110) line of phase III gradually decreases as that of the (102) line of phase II increases and finally, at 225°C, phase III disappears completely. On cooling, phase III does not appear until the sample is cooled to 206°C, which is 19°C below the temperature at which it disappeared on heating. The amount of phase III increases at the expense of phase II on further cooling to 203°, 198°, and 192°C and only at 185°C does phase II disappear almost completely. Thus the coexistence of phases in the transformation region and the temperature hysteresis are clearly seen in fig. 5.2. This coexistence of phases along with the thermal hysteresis can also be seen by referring to fig. 5.5.

Thermal hysteresis at the phase transformations is easily seen by referring to the conductivity plots (fig.4.1 & 4.2)
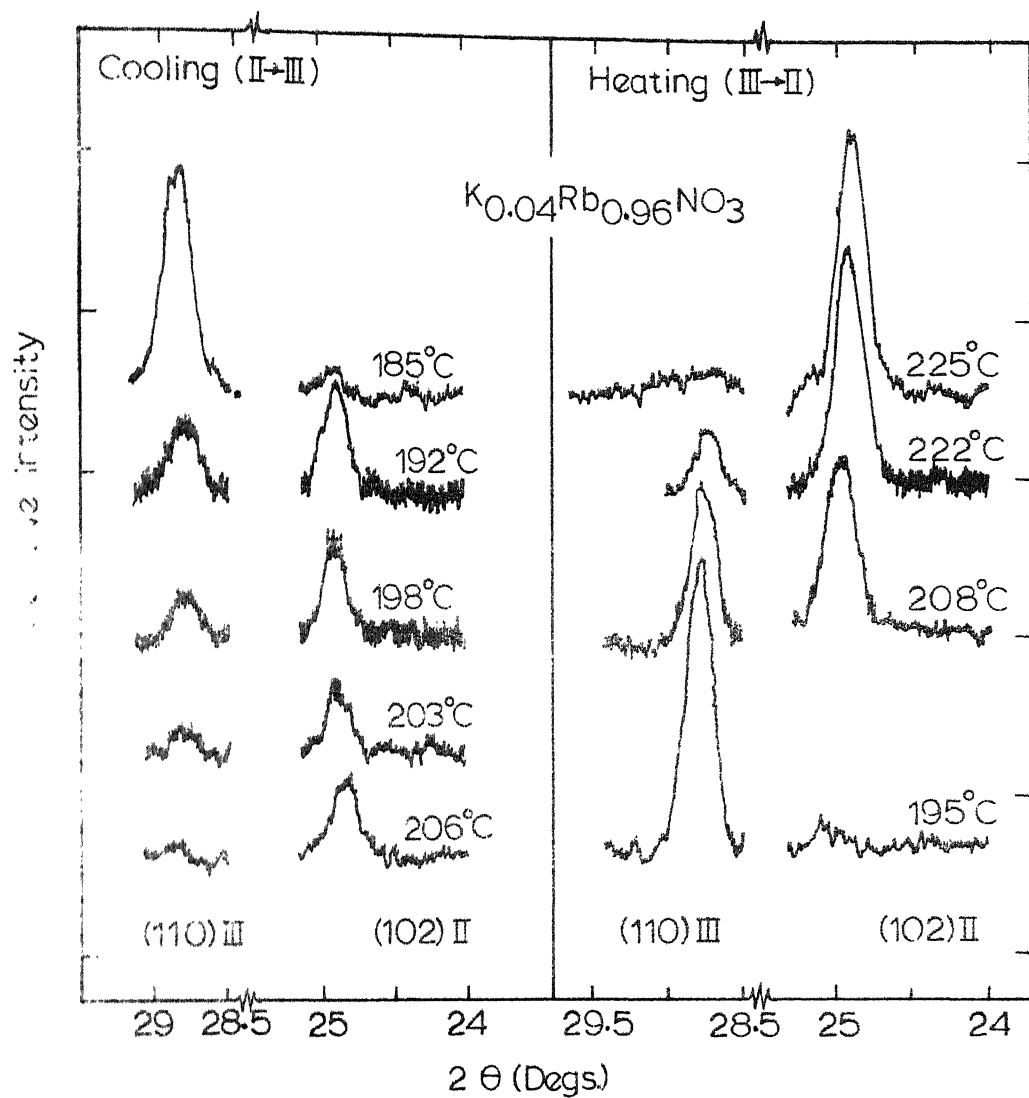
Fig. 5.2 Thermal hysteresis and co-existence of phases III and II in $K_{0.04}Rb_{0.96}NO_3$.

and dilatometric curves (figs 4.10 & 4.11). Thermal hysteresis
curves shown in fig. 5.3 for IV⇌III and III⇌II transformations
are drawn from the differential thermograms. (Appendix E) These curves plot the
amount transformed vs temperature, obtained from heating and
cooling curves The amount transformed is the ratio of the height
of a point on the DTA curve (peak) to its maximum height. This
method of plotting the hysteresis loops from DTA curves follows
that of Rao and Rao[47].

Temperature hysteresis in III⇌II transformation has also
been studied by static and dynamic methods using X-ray diffraction.
In the dynamic method, plotting the height of the characteristic
X-ray diffraction line (which is proportional to the fraction of
the transformed phase) as a function of temperature during heating
and cooling gives the hysteresis loops for the materials under
study The hysteresis loops so obtained are shown in fig. 5.4.
The slope of the vertical portion of the hysteresis loop, in case
of $RbNO_3$, shows that the transformation is quite sudden whereas
it grows sluggish with increasing concentration of Cs^+ or K^+, the
hysteresis loops become increasingly slanted with concentration.
The hysteresis in temperature decreases with Cs^+ concentration as
compared with the pure material. Reverse is the case with K^+
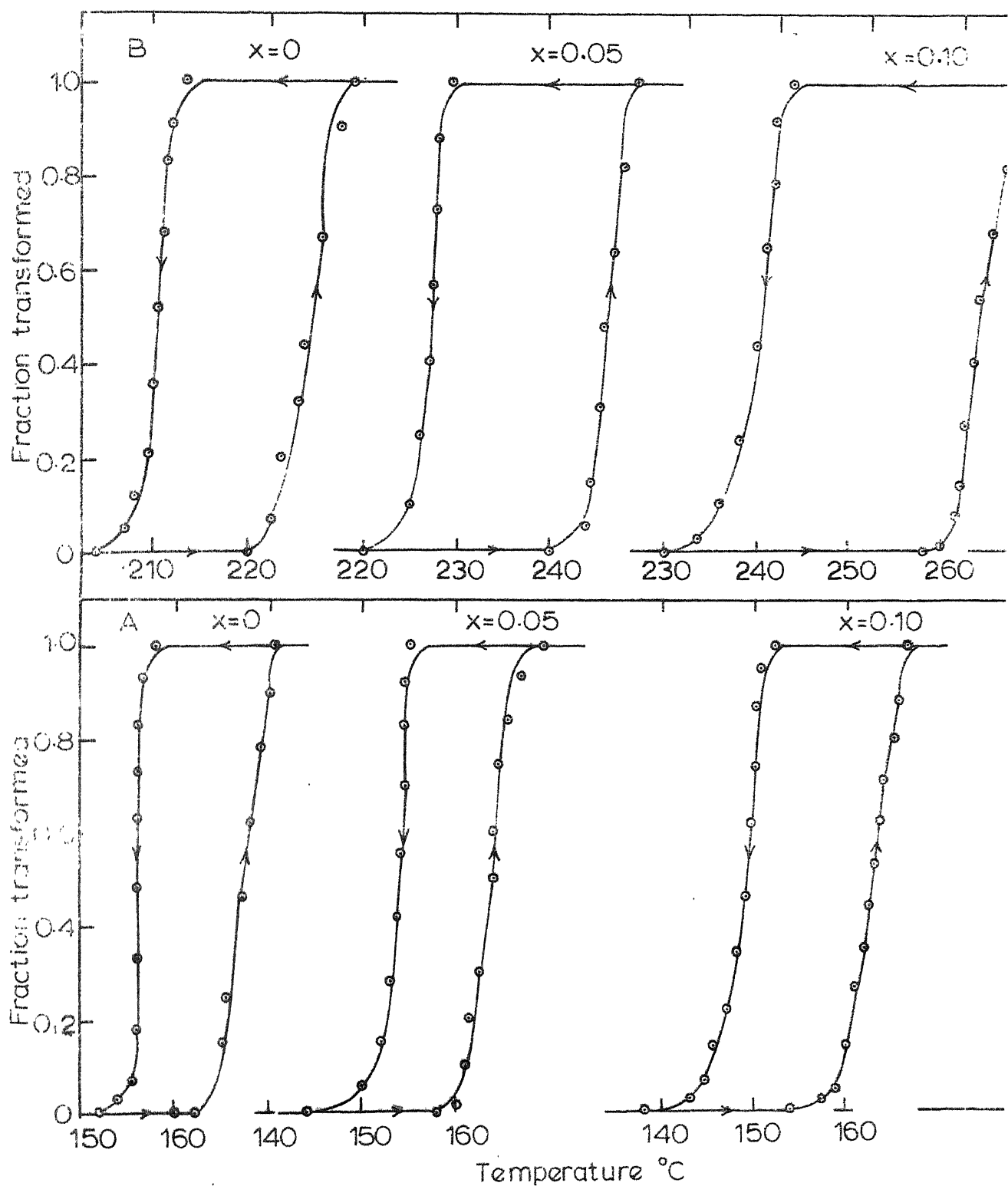
Fig. 5.3 Thermal hysterisis loops in $Cs_xRb_{1-x}NO_3$ system from DTA curve
(A) IV $\rightleftharpoons$ III transformation, (B) III $\rightleftharpoons$ II transformation.
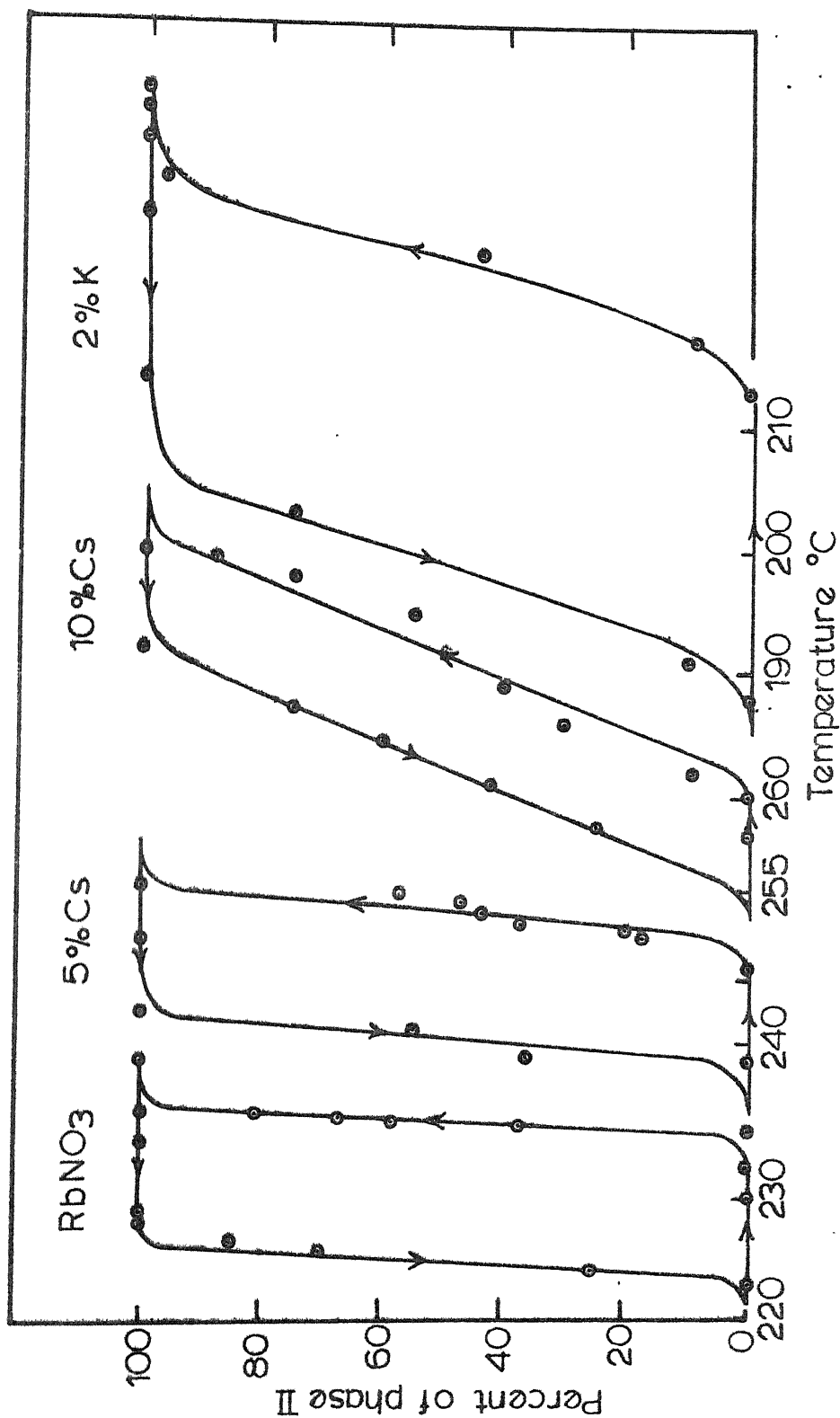
Fig. 5.4: X-ray determination of thermal hysteresis by dynamic method at III⇄II transformation in $RbNO_3$, $Cs_{0.05}Rb_{0.95}NO_3$, $Cs_{0.10}Rb_{0.90}NO_3$, $K_{0.02}Rb_{0.98}NO_3$.

concentr tion. In this connection a remark may be made about the
wide vertical hysteresis loop obtained for $Cs_{0.10}Rb_{0.90}NO_3$ at
$III \rightleftharpoons II$ transformation from DTA curves (fig 5.3) The heating
and cooling differential thermograms are not traced separately for
$III \rightleftharpoons II$ transformation due to its closeness to $II \rightleftharpoons I$ transforma-
tion and due to high rate of heating (as compared with other
methods of study) and uncontrolled cooling the spread of peaks
is not properly shown by DTA curves and hence instead of getting
a slanted loop (as determined by X-ray studies (fig 5.4)) a wide
vertical loop is obtained.

In the static method, the height of the (102) peak,
which gives the amount of phase II transformed, is plotted versus
temperature This yields a hysteresis loop. Plotting the peak
heights for (110) reflection during heating and cooling gives the
amount of phase III transformed vs temperature. Overlap of loops
shows coexistence of phases in the transformation region (see
fig 5.5) This figure is representative of the data on the
co-existence of phases in $III \rightleftharpoons II$ transition region. This is
shown here for $K_{0.04}Rb_{0.96}NO_3$ for the reason that the co-existence
of phases is observed over a larger temperature range than in the
case of the pure material and other solid solutions. The width
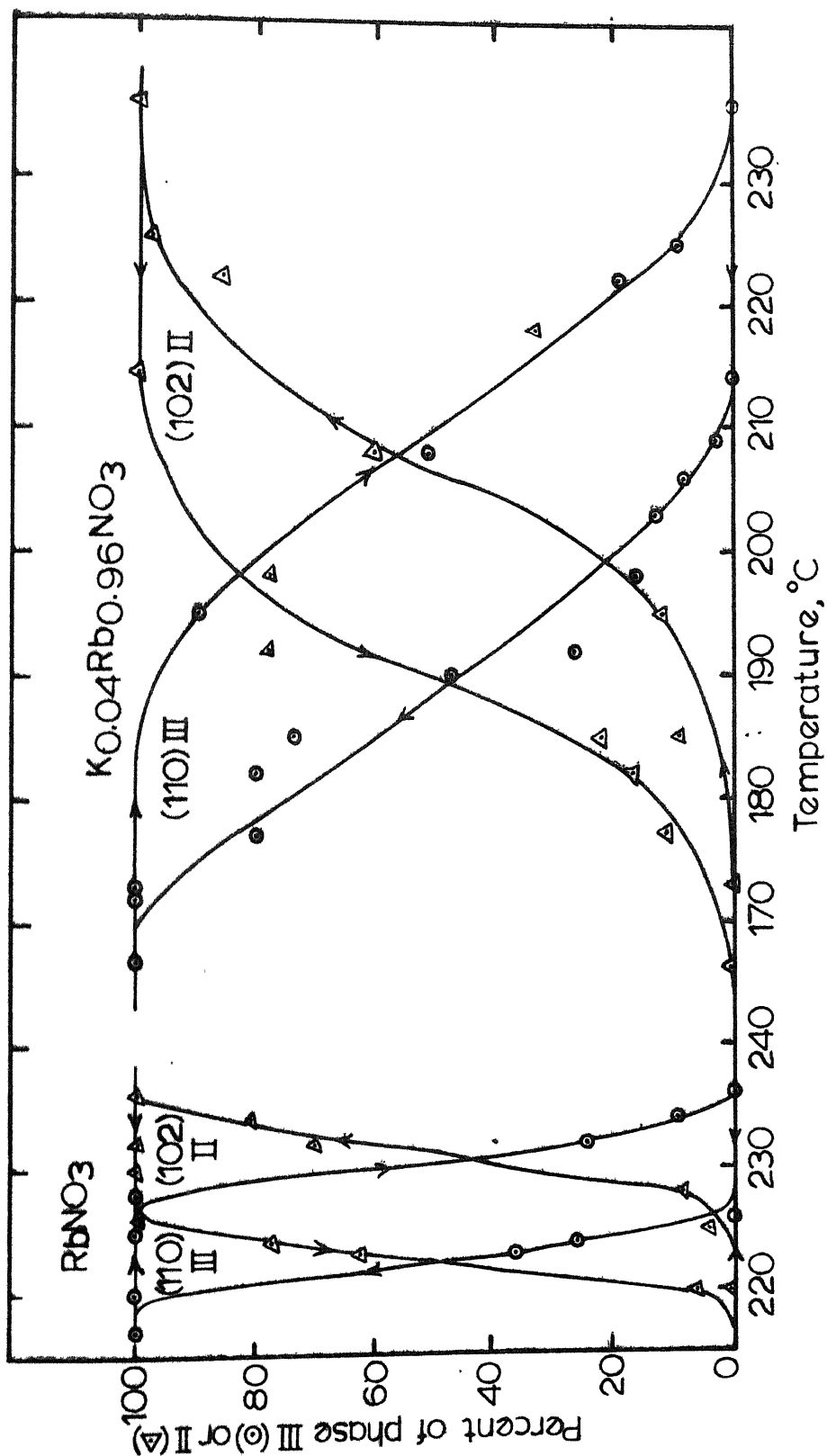
Fig. 5.5: Thermal hysteresis and coexistence of phases III and II in transition region III⇌II(static method).

of the loops in the present case is smaller than in the dynamic method. This is probably due to the fact that thermal hysteresis is a function of rate of temperature change.

The extensive solubility of $CsNO_3$ in $RbNO_3$ compared to rather small solubility of KNO_3 in $RbNO_3$ suggests that Cs^+ ions can be accommodated in the $RbNO_3$ lattice much more easily than K^+ ions without large strain or distortion. The large strain associated with the introduction of K^+ ions in $RbNO_3$ lattice gives rise to wide thermal hysteresis loops compared to those obtained with $(Cs, Rb)NO_3$ solid solutions.

Table 5.3 lists the change in volume (calculated from X-ray data) on transformation vs width of the hysteresis loop for $RbNO_3$, $Cs_{0.05}Rb_{0.95}NO_3$ and $K_{0.04}Rb_{0.96}NO_3$. This table indicates increasing hysteresis width with increasing change in volume at a transformation e.g III $\rightleftharpoons$ II transformation, for a given composition, exhibits largest hysteresis and largest volume change. Rao and Rao[47], who plotted the change in molar volume at the transformation temperatures vs area of the thermal hysteresis loops for various materials including $RbNO_3$ also find a similar relationship.

TABLE 5.3: Change in volume at the transformations (ΔV) and width of the hysteresis loops (ΔT) for $RbNO_3$, $Cs_{0.05}Rb_{0.95}NO_3$ and $K_{0.04}Rb_{0.96}NO_3$.

Phase transition	$RbNO_3$		$Cs_{0.05}Rb_{0.95}NO_3$		$K_{0.04}Rb_{0.96}NO_3$	
	$\Delta V(A^{03})$	$\Delta T(^\circ C)$	$\Delta V(A^{03})$	$\Delta T(^\circ C)$	$\Delta V(A^{03})$	$\Delta T(^\circ C)$
IV $\rightleftharpoons$ III	0.84	9	1.00	10	1.70	5
III $\rightleftharpoons$ II	11.38	18	9.64	20	12.85	36
II $\rightleftharpoons$ I	4.73	6	3.46	13	5.10	4

ΔV values are calculated from the X-ray data and ΔT from dilato-metric data.

5.2 Crystallography of $RbNO_3$:

As already seen, $RbNO_3$ has four crystalline phases.

The room temperature phase, called phase IV, is known to have a trigonal symmetry with a = $10.49A^\circ$, c = $7.44A^\circ$ and Z = 9 at room temperature   The space group is $P3_1 12$ or $P3_2 12$[4].

Finbak et al[13] have given only the Rb^+ positions in the lattice (fig. 5.7), the NO_3^- positions are indicated by Pauling and Sherman[68] in fig. 5.14. The lattice parameters determined by various authors have been compared in table 4.4. The lattice parameters at room

temperature, determined in the present study, agree very well with those reported in literature.

Phase III is cubic with Cesium Chloride type structure and a = 4.36A^O, Z = 1 at 190°C. The space group is Pa3[11]. Korhonen[11], who gave a detailed structural analysis for this phase found that NO_3 groups are situated on the body diagonals slightly away from the centre, hence he proposed a cell of double this size (fig 5.15). The results, about the space group and lattice constant of this phase, are summarized in section 1.2 and table 4.4

Phase I is known to be cubic with Sodium Chloride type structure. The cube edge is found to be 7.32A^O, a value close to the one reported by Brown and McLaren[4].

Phase II was investigated in 1937 by Finbak et al[13], for the first time, by powder X-ray diffraction techniques at 250°C. It was reported to have a hexagonal symmetry. The cell parameters found were a = 5.48A^O and c = 10.71A^O with Z = 3. The corresponding rhombohedral parameters were a = 4.77A^O, α = 70° 10' and Z = 1. In 1962, Brown and McLaren[4] reinvestigated this phase and proposed a number of possible unit cells for this phase. Based on the closeness of fit and an apparently simple relationship between the

cell parameters of phases II and III, Brown and McLaren proposed a tetragonal cell for this phase with lattice constants a = 6.19A^O, c = 8.74A^O and Z = 4.

An indexed X-ray diffraction pattern for phase II is shown in table 5.4. This table shows that both the tetragonal (a = 6.16A^O and c = 8.73A^O) and the hexagonal (a = 5.51A^O, c = 10.74A^O) cells fit equally well for this phase. So the only reason, for Brown and McLaren to prefer a tetragonal cell for this phase, seems to be the simple relationship between phases III and II. It was also reported[4] that RbNO$_3$ crystals crack and bend at III →II transformation. In view of this disruptive nature of the transformation, a simple relationship between phases III and II, does not seem to be an essential requirement.

In fig. 5.1 is plotted $\frac{1}{3} \frac{\Delta V}{V}$ vs temperature, from the X-ray data, to compare with the corresponding dilatometric data. For phase II, this plot is shown both for the tetragonal and the hexagonal cells. It is evident that the hexagonal symmetry for phase II is definitely the better choice.

Further support for the above choise can be derived from the density calculations based on the dilatometric and the X-ray data. This is shown in table 5.5. The calculated density values

TABLE 5 4 Observed and calculated 'd' values for the hexagonal and

tetragonal structures of phase II of $Pb^{II}O_3$

Observed 'd' (A^O)			Hexagonal cell		Tetragonal cell	
FHS[13]	BM[4]	Present study	d cal	h k l	d cal	h k l
4.25	4.36	4.35	4.36	101	4.36	002
3.53	3.57	3.58	3.58	003	3.56	102
2.72	2.77	2.76	2.76	110	2.75	210
2.31	2.34	2.34	2.34	104	2.33	212
2.18	2.19	2.19	2.18/2.18	202/113	2 18	004
	1.96		1.96	105	1.95	222
1.77	1.79		1.79	006	1.78	312
1.70	1.72		1.71	212	1.71	320
	1.60		1.59	300	1.59	322
1.50	1.50		1.50/1.50	116/214	1.49	410
1.45	1.46		1.46/1.45	107/303	1.45	330

TABLE 5.5 (Structural parameters and) density, calculated from the X-ray and dilatometric data, at different temperatures.

Phase	Temperature (°C)	Lattice Parameters* (Å)		Z	Density calculated from X-ray data (g/cc)	Density calculated from dilatometric data (g/cc)	Observed density[70]	Crystal structure
IV	29	$a_R=6.54$	$\alpha_R=106°\ 28'$		3.11	3.11	3.11	Rhombohedral
	161	6.63	$106°\ 38'$	3	3.00	2.99	2.99	
	29	$a_H=10.45$	$c_H=7.44$		3.11	3.11	3.11	Hexagonal
	161	10.63	7.51	3	3.00	2.99	2.99	
III	170	$a = 4.347$		1	2.98	2.93	2.93	Cubic
	222	4.376			2.92	2.85	2.87	

(TABLE 5.5 contd.)

Phase	Temperature (°C)	Lattice Parameters* (A°)		Z	Density calculated from X-ray detanometric data (g/c.c)	Density calculated from dilatometric data (g/c.c.)	Observed density(70) (g/c.c)	Crystal structure
	227	a_R=4.80	α_R=70° 43'	1	2.56	2.57		Rhombohedral
	281	4.81	69° 8'		2.62	2.52		
II	227	a_H=5.55	c_H=10.69	3	2.56	2.57		Hexagonal
	281	5.47	10.80		2.60	2.52		
	227	a_T=6.21	c_T=8.75	4	2.91	2.57		Tetragonal
	281	6.11	8.71		3.01	2.52		
I	289	a = 7.32		4	2.50	2.49		Cubic

* a_R and α_R are the lattice constants of the Rhombohedral cell a_H and c_H represent the parameters for the Hexagonal cell and ε_T, c_T for the Tetragonal cell.

in phase II compare reasonably well with those based on the hexagonal symmetry for this phase The calculated density values, based on the tetragonal cell do not agree at all with those determined from dilatometric data The density values for the other phases calculated from the dilatometric and X-ray data are in good agreement. Also the observed values of density[70] in phases IV and III of $RbNO_3$ are very close to those calculated from the dilatometric data and also from the X-ray data.

Based on the number of formula units a probable hexagonal cell with cation positions is proposed in fig. 5.6. The true symmetry for phase II can only be established unambiguously by single crystal X-ray study. However, attempts to retain the crystal in a sound condition on heating to $250^{\circ}C$, in the present study as well as by earlier workers, have been unsuccessful.

5.2.1 Lattice Relationships between the four Phases of $RbNO_3$.

5.2.2 IV and II relation:

Finbak et al[13] have shown a relation between the hexagonal phase IV and the cubic phase III in fig. 5.7. It is easy to write down with the help of this diagram that

$$3a_{III} = \sqrt{a^2_{IV} + c^2_{IV}} \qquad (1)$$

(2)
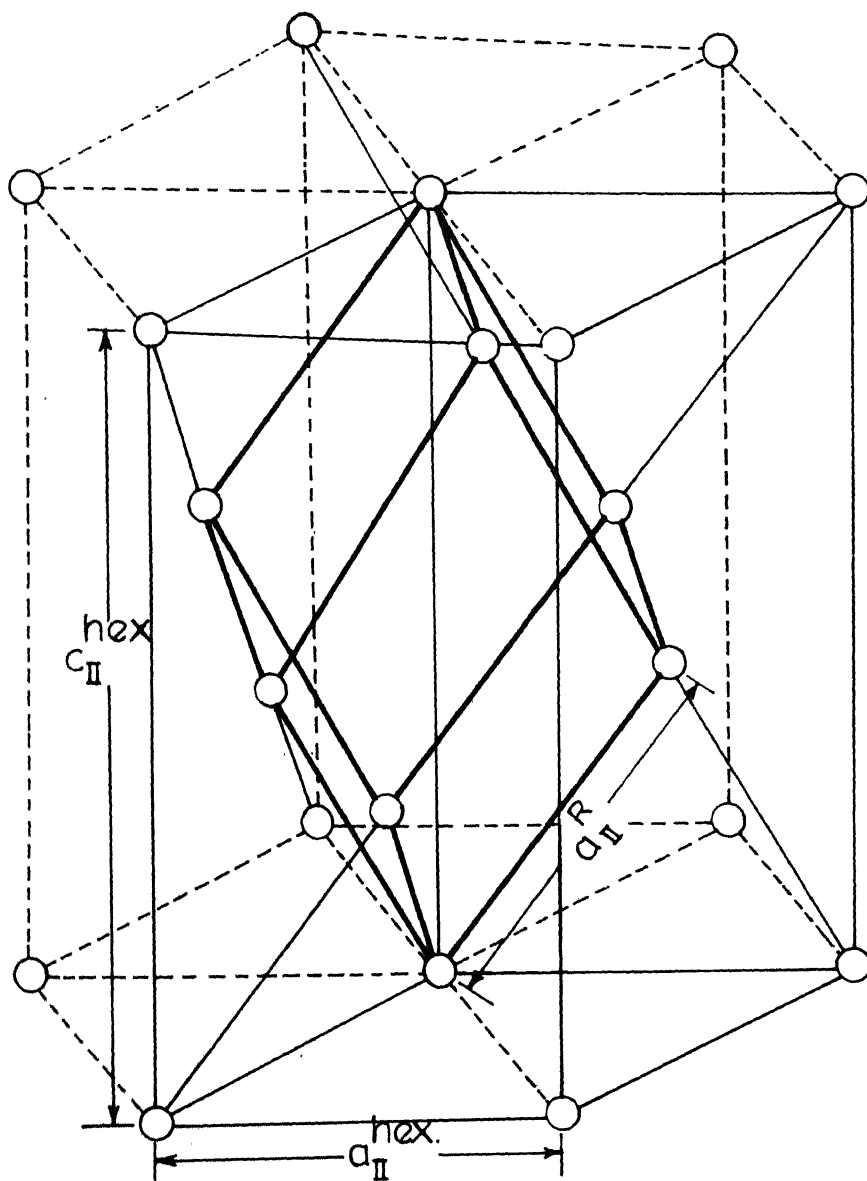
Fig. 5.6: Proposed hexagonal cell of phase II. The corresponding rhombohedral cell is also shown by thick lines. Circules indicate the cation positions.
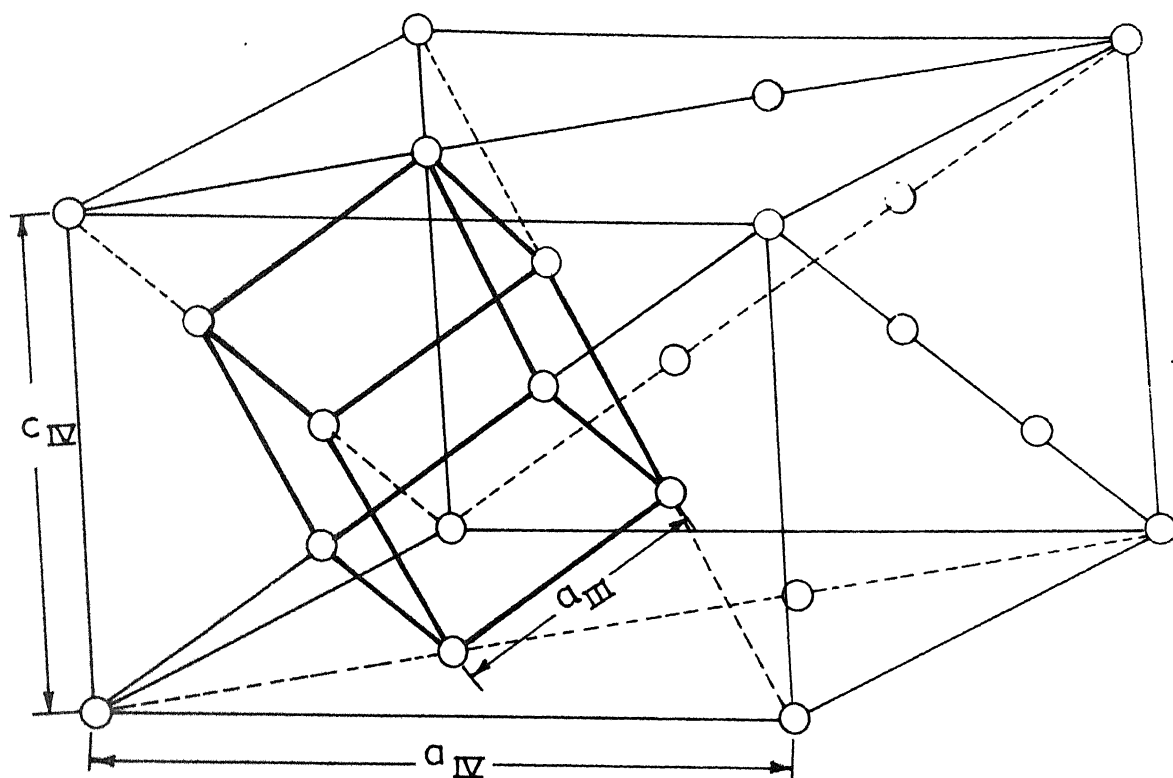
Fig. 5.7: Structural relationship between phases IV and III of $RbNO_3$ [ref. 13].

where a_{IV}, c_{IV} and a_{III} are the lattice parameters of the phases

IV and III respectively.

From (1) and (2),

$$a_{IV} = \sqrt{6}\ a_{III}$$

and $$c_{IV} = \sqrt{3}\ a_{III}$$

$$a_{IV} = \sqrt{2}\ c_{IV}$$

(3)

As seen in section 1.2, Brown and McLaren[4] also

pointed out that the c-axis of the trigonal phase transforms to

cubic $[111]$ direction and $[10.1]$ of the trigonal to cubic edge

at IV→III transformation This relationship was shown in fig.

1.2. The relationships (3) also indicate that going from phase

III to IV the hexagonal parameters a_{IV} and c_{IV} are obtained in the

directions $[211]$ and $[111]$ respectively of the cube. This is

shown in fig 5.8

The relationships (3) are also apparent from the lattice

parameter values, as follows:

$$a_{IV} = 10.63 A^{\circ}, \quad \sqrt{6}\ a_{III} = 10.65 A^{\circ}$$

$$c_{IV} = 7.51 A^{\circ}, \quad \sqrt{3}\ a_{III} = 7.53 A^{\circ}.$$

The a_{IV} and c_{IV} values quoted above are at $161^{\circ}C$ and a_{III} value at

$170^{\circ}C$
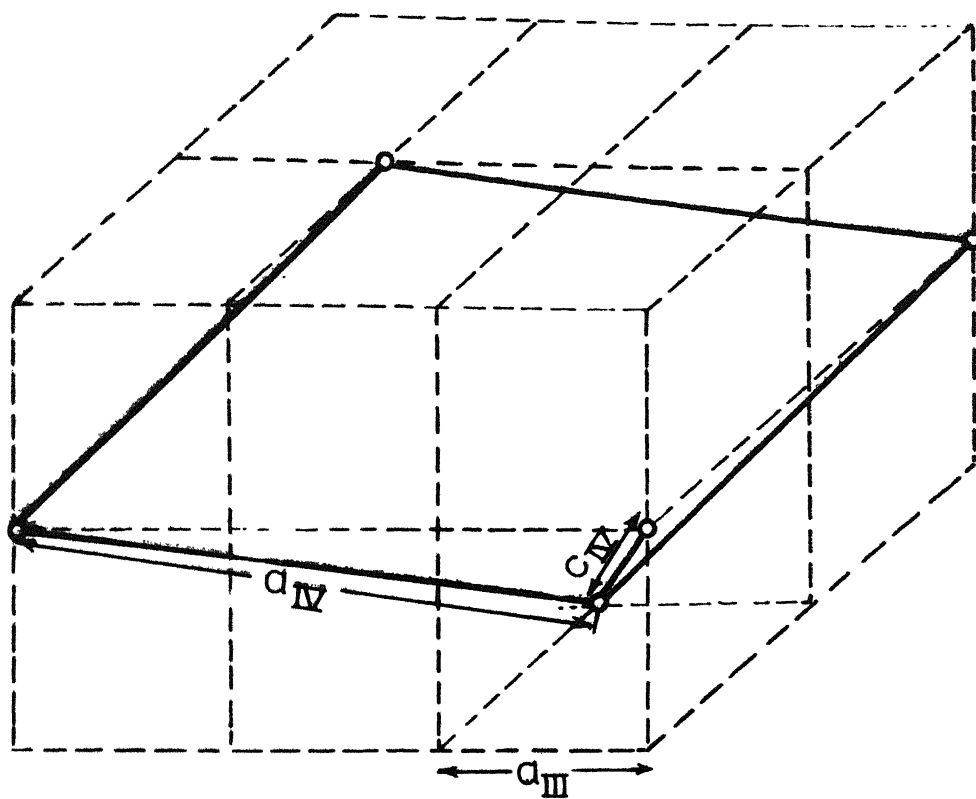
Fig. 5. ₍ Lattice relationship of phases III and IV in RbNO₃.

The volume of the trigonal phase IV can be written as

$$V_{IV} = \frac{\sqrt{3}}{2} a_{IV}^2 c_{IV}$$

$$= \frac{\sqrt{3}}{2} 6a_{III}^2 \sqrt{3} a_{III}$$

$$= 9a_{III}^3$$

$$V_{IV} = 9V_{III} \tag{4}$$

This volume relationship between phases IV and III is consistent with the number of molecules per unit cell in these phases i.e. $Z=9$ in phase IV and $Z = 1$ in phase III.

5.2.3   III and II relation:

Phase II has been proposed by Brown and McLaren[4] as one of tetragonal symmetry   The simple relation between phases III and II was shown to be the following (see section 1.2):

$$\left.\begin{array}{c} \sqrt{2} \; a_{III} = a_{II} \\[2mm] 2 \; a_{III} = c_{II} \end{array}\right\} \tag{5}$$

This is illustrated in fig. 1.3. The volume of phase II can be written as

$$V_{II} = a_{II}^2 c_{II}$$

$$= 2a_{III}^2 \cdot 2a_{III} = 4a_{III}^3$$

$$V = 4V_{III} \tag{6}$$

This volume relationship is again consistent with the number of molecules per unit cell in each of these phases i e. $Z = 1$ for phase III and $Z = 4$ for phase II.

As seen in section 5.2 a hexagonal (or rhombohedral) unit cell is a better choice for phase II. Hence it seems reasonable to propose that at III $\rightarrow$ II transition the cube distorts to become a rhombohedron. The cubic edge ($a_{III} = 4.38A^{\circ}$) of phase III gets elongated to become equal to the rhombohedral edge ($a_{II}^{R} = 4.8A^{\circ}$) and the 90° angle of the cube changes to the rhombohedral angle (α) of 70° $48'$. This is shown in fig. 5.9. This large expansion seems reasonable in view of the dilatometric observation at this phase transition Also distortion of the cube angle is consistent with the bending and cracking of $RbNO_3$ crystals observed by Brown and McLaren[4] at this phase change

Since a rhombohedral cell has a corresponding hexagonal cell, we can write down the corresponding parameters for these two cells,

$$a_{II}^{R} = 4.80A^{\circ}, \quad \text{and} \quad a_{II}^{hex} = 5.55A^{\circ}$$

$$\alpha^{R} = 70^{\circ} \quad 48' \qquad c_{II}^{hex} = 10.71A^{\circ}$$

(7)

Also (see below), $\sqrt[4]{2} \; a_{III} = 5.21A^{\circ}$

and $\sqrt{6} \; a_{III} = 10.73A^{\circ}$

(8)
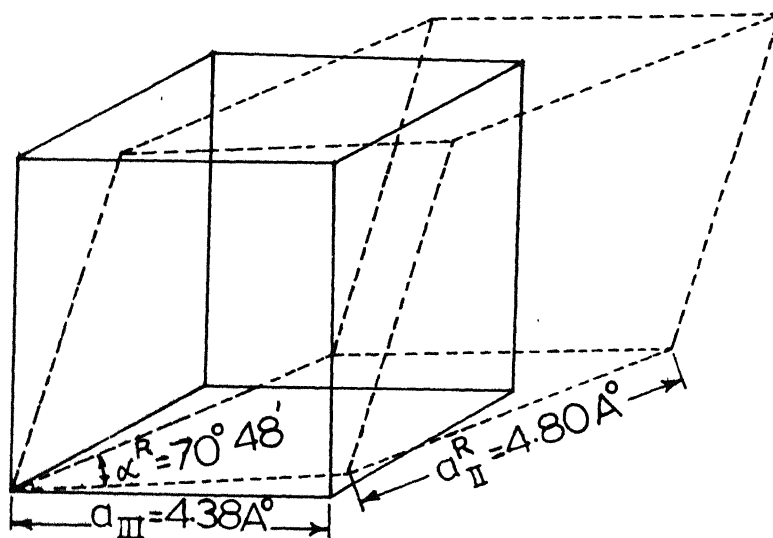
Fig. 5.9: Proposed structural * relationship between
the cubic phase III and the rhombohedral
phase II.

The lattice parameters in eqn.(7) are taken at 227°C and in eqn.(8) at 222°C

Based on the equivalence of unit cell volumes of phases II and III, it can be shown that

$$a_{II}^{hex} \simeq \sqrt[4]{2} \; a_{II}^{*}$$

and
$$c_{II}^{hex} \simeq \sqrt{6} \; a_{III}$$
(9)

so that the volume of phase II is

$$V_{II} = \frac{\sqrt{3}}{2} \; a_{II}^{hex^{2}} \; c_{II}^{hex}$$

$$= \frac{\sqrt{3}}{2} \sqrt{2} \; a_{III}^{2} \; \sqrt{6} \; a_{III}$$

$$= 3a_{III}^{3}$$

$$\therefore \quad V_{II} = 3V_{III}$$
(10)

This volume relationship, between phases III and II, agrees with the number of formula units in these phases i.e. $Z = 1$ for phase III and $Z = 3$ for phase II.

5.2.4 II and I relation.

At 281°C, the rhombohedral parameters of phase II are

$$a_{II}^{R} = 4.81 \overset{o}{A}$$

and
$$\alpha^{R} = 69^{o} \; 8'$$
(11)

The volume of phase II is

$$V_{II} = a_{II}^{R^3} \sqrt{1-3\cos^2\alpha^R + 2\cos^3\alpha^R}$$

$$= 93.63 \text{ A}^{O3}$$

Assuming that no change in volume took place at II→I transition except that the rhombohedral angle changed from 69° $8'$ to 60°, the resulting rhombohedral edge will be $5.07A^O$. It may be noted that phase I has Sodium Chloride type structure. Joining the cube corners, at the end of a body diagonal, with the face centres yields a rhombohedron (fig. 5.10). If this rhombohedral edge (a_R, in phase II) becomes equal to half the face diagonal of a cube of phase I (fig 5.10), then we can write down the cubic edge of phase I as,

$$\frac{\sqrt{2} \, a_I}{2} = 5.07$$

$$\text{or} \quad a_I = 7.17A^O$$

This value of cubic edge is close to the observed value at $290^O C$, viz $7.32A^O$. The difference may be due to the large thermal expansion taking place at II→I transition as is evident from fig. 4.15.

Since a rhombohedral cell has a corresponding hexagonal cell, the corresponding parameters may be written as
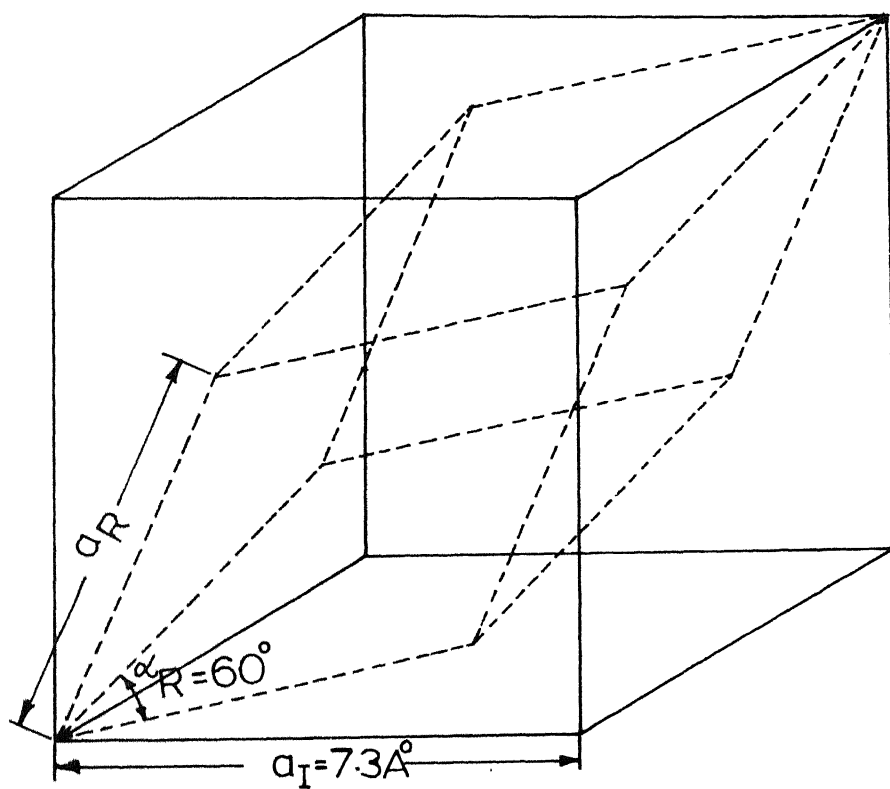
Fig. 5.10: Proposed structural relationship between the cubic phase I and the rhombohedral phase II.

$$a_{II}^{hex} = 5.47A^{0} \qquad a_{II}^{R} = 4.81A^{0}$$

$$c_{II}^{hex} = 10.89A^{0} \qquad \alpha^{R} = 69^{0} \quad 8^{/} \qquad (12)$$

From (12), we may also write

$$c_{II}^{hex} = 2a_{II}^{hex} \qquad (13)$$

Also,

$$a_{I} = 7.32A^{0}, \qquad \sqrt[4]{3} \; a_{II}^{hex} = 7.20A^{0}$$

$$\frac{2}{3} \; c_{II}^{hex} = 7.26A^{0}$$

Hence the lattice relationships may be

$$a_{I} \simeq \sqrt[4]{3} \; a_{II}^{hex} = \frac{2}{3} \; c_{II}^{hex} \qquad (14)$$

These relationships can be derived from the equivalence of unit

cell volumes of phases II and I.

The volume of phase II may be written as

$$V_{II} = \frac{\sqrt{3}}{2} \; a_{II}^{hex^{2}} \; c_{II}^{hex}$$

$$\simeq \frac{\sqrt{3}}{2} \; \frac{a_{I}^{2}}{\sqrt{3}} \; \frac{3}{2} \; a_{I}$$

$$= \frac{3}{4} \; V_{I}$$

$$\text{or} \quad \frac{V_{II}}{3} = \frac{V_{I}}{4} \qquad (15)$$

This volume relationship is again agreeable with the

number of formula units in phases II and I i.e. Z = 3 for phase II

5.3 Solid Solution Effects.

5.3.1 Effect of Ionic Size and Solubility Limits:

Lattice parameters vs composition for $(Cs, Rb)NO_3$ and $(K, Rb)NO_3$ systems at room temperature are shown in fig. 5.11. It can be seen that in $(Cs, Rb)NO_3$ system the 'a' parameter increases at a faster rate than the 'c' parameter. After the solubility limit is reached in phase IV both become constant. In $(K, Rb)NO_3$ system both 'c' and 'a' decrease with K^+ concentration and become constant when the solubility limit is reached as expected. It is, therefore, concluded that addition of Cs^+ increases the lattice volume and addition of K^+ decreases it. This is consistent because of the size of Rb^+ ion being intermediate between those of Cs^+ and K^+ ions. (The radii of K^+, Rb^+ and Cs^+ are respectively $1.33A^\circ$, $1.48A^\circ$ and $1.68A^\circ$). Another conclusion is that the solubility limit of $CsNO_3$ in $RbNO_3$, in phase IV, is much greater than that of KNO_3 in $RbNO_3$. This is probably due to the similarity of the room temperature phases of $RbNO_3$ and $CsNO_3$ and incompatibility of the room temperature phase of $RbNO_3$ with that of KNO_3. (see table 5.6).

It was seen in Chapter 4 that in $Cs_xRb_{1-x}NO_3$ system there is a complete disappearance of phase II in the range $0.25 < x < 0.30$ during heating and cooling. From table 5.6 it is clear that phase I
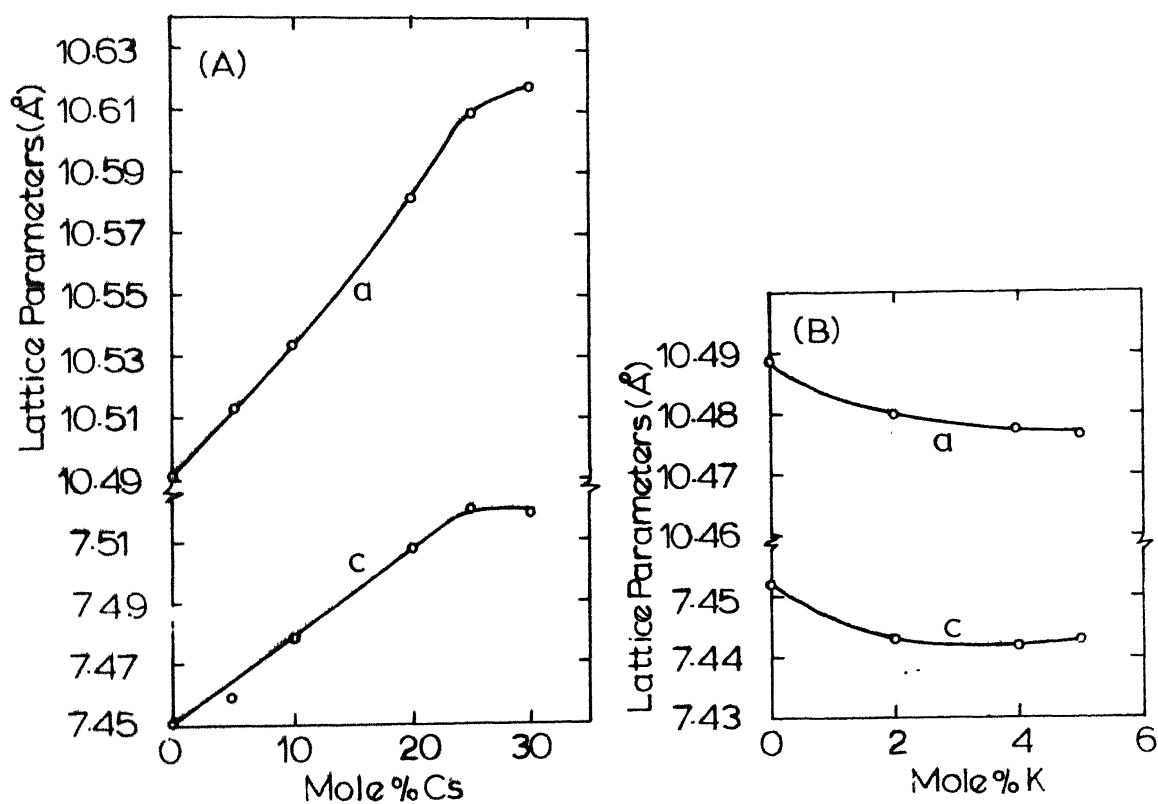
Fig. 5.11 Lattice parameters vs composition of (A) $Cs_x Rb_{1-x} NO_3$ and (B) $K_x Rb_{1-x} NO_3$ systems at room temperature.

TABLE: 5.6   Structural parameters of Nitrates of Rubidium, Cesium and Potassium in different phases.

Temperature scale (°C)	$RbNO_3$	$CsNO_3$	KNO_3
0	Phase IV	Phase II[73]	Phase II[57]
			Orthorhombic
	$a_H = 10.49$Å	$a_H = 10.87$	$a = 5.41$Å
			$b = 9.14$Å
			$c = 6.43$Å
50	$c_H = 7.44$Å	$c_H = 7.76$	$Z = 4$
	$Z = 9$		
	(Parameters at room temperature)		
100			
			Phase III*
			↓ ↑
			Phase I[75]
150			$a_H = 5.385$A°
	Phase III	Phase I[74]	$c_H = 9.760$A°
	$a = 4.36$A°	$a = 4.499$A°	$Z = 3$
200	$Z = 1$	(at 170°C)	or
	(at 190°C)		$a_R = 4.50$A°
	Phase II		$\alpha_R = 73° \ 30'$
	$a_H = 5\ 54$A°		$Z = 1$
250	$c_H = 10.75$A°		
	$Z = 3$		
	or $a_R = 4.80$A°,		
	$\alpha_R = 70° \ 28'$		
	$Z = 1$ (at 232°C)		

TABLE 5.6 (Continued)

Temperature scale(°C)	RbNO₃	CsNO₃	KNO₃
	$RbNO_3$	$CsNO_3$	KNO_3

Temperature scale (°C)	$RbNO_3$	$CsNO_3$	KNO_3
300	Phase I $a = 7.32 A°$ $z = 4$ (at 290°C)		
	Liquid		
250			Liquid
200			
		Liquid	

The dotted lines represent the transformation temperatures.
The arrows pointing up and down in the last column indicate
cooling and heating respectively.

x The lattice parameters of phase III (rhombohedral) of KNO_3
are $a_R = 4.365 A°$, $\alpha_R = 76° 56'$ at 120°C (ref. 57).

of $CsNO_3$ is similar to phase III of $RbNO_3$. This leads to an extension of phase III of $RbNO_3$, with increasing x, in $Cs_xRb_{1-x}NO_3$ system at the expense of phase II. In $K_xRb_{1-x}NO_3$ system phase III disappears during cooling in the range $0\ 03 < x < 0.05$. Referring to table 5.6, it is evident that phase I of KNO_3 is similar to phase II of $RbNO_3$. This results in the widening of phase II in $K_xRb_{1-x}NO_3$ system with increasing x.

It was noted in chapter 4 that the transformations in $RbNO_3$ get smeared due to ionic substitutions in the two systems of solid solutions. This may be understood in terms of the distortion of the $RbNO_3$ lattice due to these substitutions. K^+ substitution seems to distort the lattice more than what Cs^+ does.

5.3.2 Shifting of Transformation Temperatures.

As seen in chapter 4 the transformation temperatures of $RbNO_3$ get shifted by partial substitution of Rb^+ ions by ions of comparatively larger size e.g. Cs^+ or of smaller size e.g. K^+. It was observed that transition temperature III$\rightleftharpoons$II shifts markedly towards higher or lower temperatures by ionic substitutions of Rb^+ with Cs^+ or K^+ respectively. The transition temperatures IV$\rightleftharpoons$III and II$\rightleftharpoons$I are shifted slightly to lower temperatures in both types of substitution

This shifting of transition temperatures is explained below on the basis of (i) similarity of phases of KNO_3 and $CsNO_3$ with those of $RbNO_3$ and (ii) activation energy values determined from the differential thermal analysis studies.

5.3 3 Similarity of Phases:

As seen in section 5.3.1 the phases IV and III of $RbNO_3$ are similar to the phases II and I of $CsNO_3$. Also the transformation temperature IV $\rightleftharpoons$ III in $RbNO_3$ and II $\rightleftharpoons$ I in $CsNO_3$ are quite close (table 5.6). Due to these reasons the transformation temperature IV $\rightleftharpoons$ III in $RbNO_3$ is not much affected with increasing x in $Cs_x Rb_{1-x} NO_3$. From table 5.6 it is seen that the temperature range of phase I of $CsNO_3$, which is similar to phase III of $RbNO_3$, is very large. Hence phase III extends in $Cs_x Rb_{1-x} NO_3$ system with increasing x. Since the only way it can extend is by shifting III $\rightarrow$ II transition, therefore, this transition temperature shifts markedly to higher temperatures with concentration of $CsNO_3$.

It was seen in section 5 3.1 that phase II of $RbNO_3$ is similar to phase I of KNO_3. Hence in $K_x Rb_{1-x} NO_3$ system, phase II becomes wider with increasing x Since the transition temperature II $\rightarrow$ I in KNO_3 is very much lower than IV $\rightarrow$ III in $RbNO_3$ so that phase II in $K_x Rb_{1-x} NO_3$ has a tendency to extend on the low temperature

side. This results in a substantial shifting of $III \rightleftharpoons II$ transition with increasing concentration of KNO_3.

5.3.4 Thermal Activation Energy.

As seen in section 4.2 on "Thermodynamic parameters from DTA", the activation energy E_a is proportional to the slope of activation energy plot. In fig. 5.12 if straight line 1 represents the activation energy plot for the pure material then 2 and 3 represent those for the solid solutions $K_x Rb_{1-x} NO_3$ and $Cs_x Rb_{1-x} NO_3$ at $III \rightarrow II$ transformation. It is seen from this figure that for the same rate constant (or rate of transformation) if the slope increases from curves 1 to 3 (and hence the activation energy also) the transformation temperature T increases and vice versa. If the value of rate constant is also slightly lowered then these changes of transformation temperature are even more. In $III \rightarrow II$ transformation, the rate of transformation is lowered in both systems i.e. $Cs_x Rb_{1-x} NO_3$ and $K_x Rb_{1-x} NO_3$ but E_a increases in the first system and decreases in the second system (Table 4.3). Therefore, transformation temperature increases and decreases respectively for these systems.

In $IV \rightarrow III$ transformation the activation energy is lowered in both the systems (Table 4.3) and hence the transformation temperature in both cases is slightly lowered. These conclusions may be regarded as semiquantitative only.
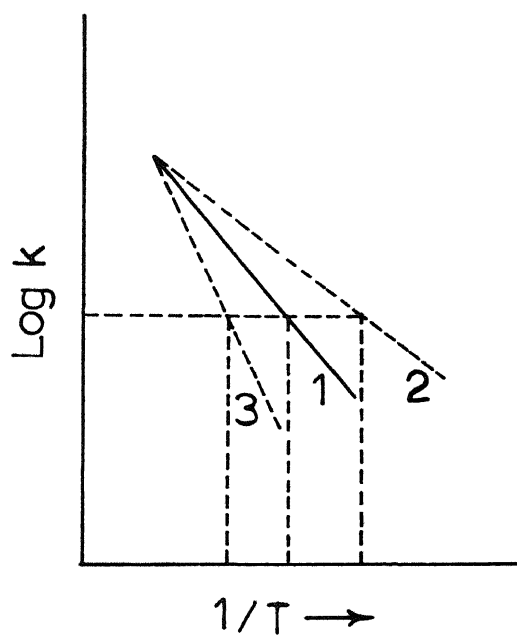
Fig. 5.12: Schematic diagram showing the effect of ionic substitution on the activation energy plot.

5.4 Infrared Absorption:

The infrared absorption spectra of $RbNO_3$, from $30^{\circ}C$ to $294^{\circ}C$, which is near its melting point, are presented in figs. 4.18 and 4.19 and of the solid solutions $Cs_{0.10}Rb_{0.90}NO_3$ and $K_{0.02}Rb_{0.98}NO_3$ at room temperature in figs. 4.21 and 4.22. Table 4.5 lists the fundamental modes of vibration of NO_3^- ion in different phases of $RbNO_3$ and table 4.6 gives a comparative study of these modes in the solid solutions at room temperature. In this section we wish (i) to interpret the spectra in the four crystalline phases of $RbNO_3$ and (ii) to explain the changes in infrared spectra of $RbNO_3$ due to partial substitution of Cs^+ and K^+ for Rb^+.

The spectra of $RbNO_3$ consist almost exclusively of the frequencies to be associated with the NO_3 group[52]. Starting with the spectrum of a free nitrate ion, correlation charts giving the theoretical pattern of the spectrum of th nitrate ion in different phases can be set up.

A free nitrate ion belongs to the symmetry point group D_{3h} and has four distinct fundamental modes, as shown below (Table 5.7)[71].

TABLE: 5.7 The spectral activity, approximate position, species

and types of vibration of fundamental modes of NO_3^- ion

of symmetry D_{3h}.

Fundamental mode	Species	Type of vibration	Approximate frequency (cm^{-1})	Spectral activity
ν_1	A_1'	Symmetric stretching	1050	Raman (R)
ν_2	A_2''	Out-of-plane bending	830	Infrared (IR)
ν_3	E'	degenerate-stretching	1390	(R, IR)
ν_4	E'	degenerate-bending	720	(R, IR).

5.4.1 Phase IV:

According to Pauling and Sherman[68] the room temperature

phase of $RbNO_3$ is hexagonal, space group C_{3v}^2 with nine molecules

per unit cell (fig. 5.14).

From fig. 5.14 it is evident that there are two sets of

sites for NO_3 group in the hexagonal structure, one set having site

symmetry C_{3v} and the other set having site symmetry C_s. Let the

co-ordinate axes be so chosen that the z-axis is perpendicular to the

plane of the NO_3^- ion (or plane of the paper) and x-axes coincides

with one of the N-O bonds   The correlation table 5.8 shows that

at this site all the modes become infrared active, the resulting

modes entering into the various species of the group C_{3v}^2 as shown

TABLE 5.8   Correlation showing the fundamental modes of NO_3^- ion

   (of site symmetry C_s) entering into various species of

   the group C_{3v}^2 .

Transition dipole component in D_{3h} sym. group.	Funda-mental modes	Species of D_{3h} symmetry	Species of C_s symmetry	Species of C_{3v} symmetry	Transition dipole components in C_{3v} group.
	ν_1	A_1'		A_1'	T_z
T_z	ν_2	A_2''	A' (T_x, T_y)		
T_x, T_y	ν_3, ν_4	E	A'' (T_z)	E A_2	T_x, T_y

in this table   The selection rules for this group show that only

the species A_1 and E are infrared active with their transition dipoles

along the z, and x,y directions respectively. Thus the modes ν_1, ν_2,

ν_3 and ν_4 will have two components each, which are infrared active. Correlation table 5.9 gives the resulting species due to the site symmetry C_{3v}. The selection rules for this group, as already seen, show that the species A_1 and E are infrared active. Therefore, the

TABLE 5.9   Correlation showing the fundamental modes of NO_3 group, of site symmetry C_{3v}, entering into the various species of the C_{3v} group.

Transition dipole components in D_{3h} sym group	Funda-mental modes	Species of D_{3h} symmetry	Species of C_{3v} symmetry	Transition dipole components in C_{3v} group.
	ν_1	A_1'		
T_z	ν_2	A_2''	A_1	T_z
T_x, T_y	ν_3, ν_4	E'	E	T_x, T_y

modes ν_1, ν_2, ν_3 and ν_4 will have one component each. Both sets of sites contribute to the transition dipoles. To understand the observed number of components the following explanation seems reasonable. Consider fig. 5.13. The symbols IA_1, IE and IIA_1, IIE
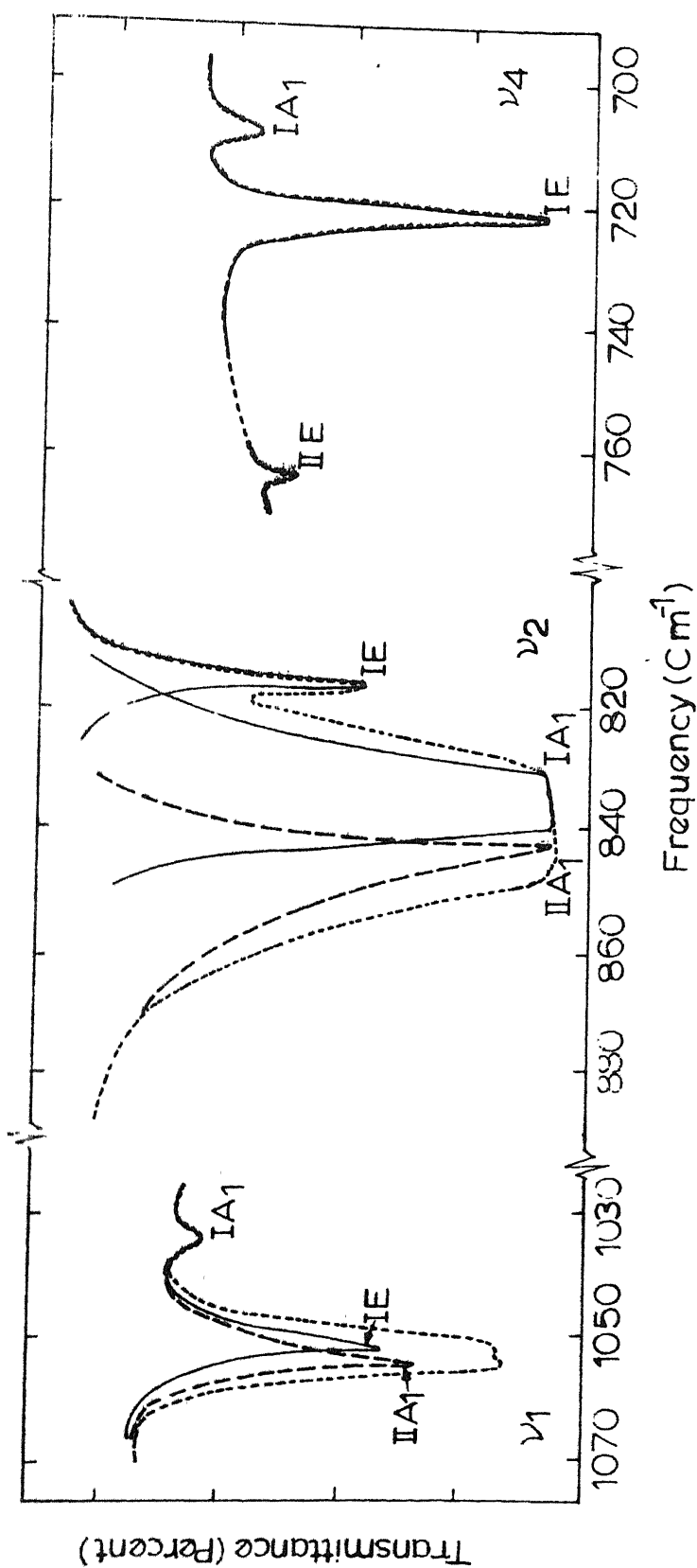
Fig. 5.13: Schematic diagram showing the number of components observed in phase IV of $RbNO_3$. Curves shown by smaller dashes are the observed traces, continuous curves are due to sites of set I and those shown by longer dashes are due to sites of set II. A_1 and E represent the symmetry species.

represent the different species $(A_1$ or E) preceded by the number
of set (i.e I or II) of sites. Let the continuous curves show
the absorption peaks due to the set I (of site symmetry C_s) and
curves, shown by longer dashes, due to the set II (of site symmetry
C_{3v}), then the curves shown by smaller dashes, which are the result-
ant of these (i e. the continuous and (longer) dashed curves), repres-
ent the observed absorption peaks. It may be noted that the components
due to the site symmetry C_{3v} (set II) lie at higher frequencies as
compared to those due to site symmetry C_s. This is probably because
the NO_3 groups with lower site symmetry (C_s) are perturbed more by
the environmental symmetry than the sites of symmetry C_{3v}. The
latter site symmetry is the same as the environmental symmetry and
is therefore, less perturbed Due to this difference in perturbation
the vibrations of set I are damped more than those of set II. Hence
vibrational frequencies of set I occur at lower frequencies as
compared to those of set II. This effect is expected to be least
in the case of symetrical stretching vibration ν_1, a little more
for the out-of-plane bending mode ν_2 and maximum for ν_3 and ν_4
modes. It may be pointed out that the z-components of the modes
ν_1, ν_3 and ν_4 which are derived from the in-plane vibration modes
of the nitrate ion, are expected to be weaker than the x and y

components. Similarly the x and y components of the mode ν_2, derived from the out-of-plane bending vibration mode, should be weaker than the z-component.

It is clear from fig 5.13 that three bands at 708 cm^{-1}, 722 cm^{-1} and 764.5 cm^{-1} can be assigned to the three components of ν_4 (two due to sites of set I and one due to sites of set II). Their individual assignment may be E 722 cm^{-1} and A_1 708 cm^{-1} due to sites of set I and A_1 764.5 cm^{-1} due to sites of set II (fig.5.13). A broad band centered around 838cm^{-1} corresponds to ν_2 mode and has two components due to sites of set I. Individual assignment may be 838 cm^{-1} (A_1) and 816.5 cm^{-1} (E) due to set I and A_1 (845cm^{-1}) due to set II (fig 5.13). Two bands at 1056 cm^{-1} and 1036 cm^{-1} (fig.5.13) are observed in the region of symmetric stretching mode ν_1. The stronger one at 1054 cm^{-1} may be assigned to E and weaker at 1036cm^{-1} to A_1 species due to sites of set I and the other at 1056 cm^{-1} of species A_1 due sites of set II (fig 5.13) It is not clear why the inactive mode ν_1 gives rise to two components A_1 and E in phase IV.

The absorption in the region of ν_3 is too broad to give any information and has, therefore, not been studied.

It may be remarked that Brown and McLaren[4] have given a space group D_3^4 or D_3^6 for phase IV of RbNO$_3$. If correlation chart

is prepared by taking D_3^4 or D_3^6 as the symmetry group then the number of components of vibrational modes of NO_3^- ion do not correspond to what is observed in the present spectra.

As seen above, the occurrence of more than one absorption peak for the modes ν_1, ν_2 and ν_4, is explained on the basis of the inequivalence of two sets of sites of NO_3^- ion in phase IV. It may be noted that this is only one of the possible explanations. Another explanation which also appears to be reasonable is that the weak additional components observed are mostly due to natural abundant isotopic species of NO_3^- ion involving either a ^{15}N atom or an ^{18}O atom. The natural abundances of $^{15}N\,^{16}O_3^-$ and $^{14}N\,^{16}O_2\,^{18}O^-$ are 0.36 percent and 0.61 percent while each of the other isotopic combination involving ^{15}N or ^{18}O has only less than 0.002 percent abundance. Thus one may expect weak absorption, due to $^{14}N\,^{16}O_2\,^{18}O^-$ and $^{15}N\,^{16}O_3^-$ isotopic species in addition to the strong absorption due to the main species $^{14}N\,^{16}O_3^-$.

Kato and Rolfe[76] have recently studied the absorptions due to naturally abundant isotopic species and enriched isotopic species of NO_3^- ion in KBr with different varieties of combinations of ^{15}N, ^{14}N, ^{16}O and ^{18}O. We will restrict overselves here with the species $^{14}N\,^{16}O_3^-$, $^{15}N\,^{16}O_3^-$ and $^{14}N\,^{16}O_2\,^{18}O^-$ as we are only

interested in molecules with sufficient natural abundance to show
up in absorption. All the four modes of vibration of NO_3^- ion (i.e.
ν_1, ν_2, ν_3 and ν_4) have been observed for NO_3^- ion in KBr where
the symmetry was assumed to be D_{3h} though ν_1 is expected to be
inactive in the infrared The ν_3 and ν_4 of NO_3^- ion with D_{3h} or
C_{3v} symmetry will split into two (A_1, B_1) for species like $^{14}N\,^{16}O_2\,^{18}O^-$
which have a site symmetry of C_{2v}. The observed and calculated
positions for ν_1, ν_2, ν_3 and ν_4 for the different isotopic species
of $^{14}N\,^{16}O_3^-$, $^{15}N\,^{16}O_3^-$ and $^{14}N\,^{16}O_2\,^{18}O^-$ according to the Kato and
Rolfe[76] are given in table 5.10.

The ν_3 vibration is too strong and broad and its
components are unobservable. The assignments of the various
absorption peaks corresponding to ν_1, ν_2 or ν_4 observed at room
temperature (or phase IV) in the present study of $RbNO_3$ are given in
table 5.11. The assignments here for NO_3^- ion in $RbNO_3$ are based on
the assignments of NO_3^- ion in KBr of table 5.10.

It may be noted that all the observed peaks except the
one at $762 cm^{-1}$ could be very well explained as belonging to the
naturally abundant isotopic species of NO_3^- ion.

To have a better understanding of the components it may
probably be worth while to study the infrared and Raman spectra of

single crystals of $RbNO_3$ at different temperatures (at low as well as high temperatures).

TABLE 5.10[76]. Experimental and calculated values of the vibrational frequencies of $^{14}N^{16}O_3^-$, $^{15}N^{16}O_3^-$ and $^{14}N^{16}O_2^{18}O^-$ ions in KBr

ν (cm^{-1})		Vibrational mode	Molecule
Experimental	Calculated		
1383.2	1383.3	ν_3(E)	$^{14}N^{16}O_3^-$
1383.2	1381.9	ν_3(B$_2$)	$^{14}N^{16}O_2^{18}O^-$
1371.1	1371.3	ν_3(A$_1$)	$^{14}N^{16}O_2^{18}O^-$
1352.3	1349.1	ν_3(E)	$^{15}N^{16}O_3^-$
1054.8	1054.3	ν_1(A$_1$)	$^{14}N^{16}O_3^-$
1055.1	1054.8	ν_1(A$_1$)	$^{15}N^{16}O_3^-$
1034.9	1034.8	ν_1(A$_1$)	$^{14}N^{16}O_2^{18}O^-$
841.3	841.4	ν_2(A$_2$)	$^{14}N^{16}O_3^-$
837.8	837.8	ν_2(B$_1$)	$^{14}N^{16}O_2^{18}O^-$
820.0	819.4	ν_2(A$_2$)	$^{15}N^{16}O_3^-$
715.6	715.7	ν_4(E)	$^{14}N^{16}O_3^-$
714.4	714.5	ν_4(E)	$^{15}N^{16}O_3^-$
	704.8	ν_4(A$_1$)	$^{14}N^{16}O_2^{18}O^-$
	693.5	ν_4(B$_2$)	$^{14}N^{16}O_2^{18}O^-$

TABLE 5.11 Assignments of the observed absorptions in $RbNO_3$ in phase IV to vibrational modes of $^{14}N^{16}O_3^-$, $^{14}N^{16}O_2^{18}O^-$ and $^{15}N^{16}O_3^-$.

Observed ν (cm^{-1})	Assignment	Molecule
1056[a]	ν_1	$^{15}N^{16}O_3^-$
1054[a]	ν_1	$^{14}N^{16}O_3^-$
1035.5	ν_1	$^{14}N^{16}O_2^{18}O^-$
838[b]	ν_2	$^{14}N^{16}O_3^-$
816.5[b]	ν_2	$^{15}N^{16}O_3^-$
764.5	ν_4	
722	ν_4	$^{14}N^{16}O_3^-$
708	ν_4	$^{14}N^{16}O_2^{18}O^-$

[a] The weak absorption at 1056 cm^{-1} probably overlaps with strong absorption of 1054 cm^{-1}, so that one sees the appearance of a barely resolved doublet.

[b] The weak absorption at 816.5 partly overlaps the strong and broad band at 838 cm^{-1}.

As the temperature is raised in this phase the intensity of the fundamental modes of vibration is reduced. This is evident from figs. 4.18 to 4.20

From the shape of the bands on either side of the absorption peak ν_1 (figs. 4.19 and 4.22) it seems that these are similar to the P and R branches in the rotation-vibration spectra[70]. This means that associated with the vibrational modes of NO_3 group is some amount of rotation about the trigonal axis. The rotational components of absorption band may be too close to be resolved in the present case. This can be seen from the following considerations.

The rotational constant of BF_3 molecule in its ground state are[72] $B_{[o]} = 0.35$ cm^{-1} and $A_{[o]} = 0.17$ cm^{-1}. The molecule BF_3 has a plane symmetrical form similar to the NO_3 group. The atomic weights of F and O are 19 and 16 respectively. The bond lengths N-O and B-F are[71] 1.22 A^o and 1.29A^o respectively. The ratio of moments of inertia $\left[I_B = I_A = 3/2 \; mr^2 \right]$ of NO_3 and BF_3 is 0.89 The corresponding rotational constants of NO_3 group will, therefore, be $B_{[o]} = 0.4$ cm^{-1} and $A_{[o]} = 0.2$ cm^{-1}. Hence separation of the rotational components in the band will be less than 1 cm^{-1}.

It may be remarked that if single crystals of $RbNO_3$ and high resolution instruments are used then it might be possible

to resolve these components.

5.4.2 Phase III

On heating to temperatures between $164^\circ C$ and $220^\circ C$ RbNO$_3$ transforms into a cubic phase. The space group reported by Korhonen[11] is T_h^6 with four molecules per unit cell. The site symmetry is $C_3^{(7)}$. The correlation table 5.12 shows that at this site all the modes become infrared active, the resulting modes

TABLE 5.12 Correlation showing the fundamental modes of NO$_3^-$ ion (of site symmetry C_3) entering into various species of the group T_h^6.

Transition dipole component in D_{3h} sym. group.	Fundamental modes	Species of D_{3h} sym.	Species of C_3 sym. (comps. of transition dipole)	Species of T_h^6 sym.	Transition dipole comps. in T_h group.
	ν_1	A_1'			
T_z	ν_2	A_2''	A (T_z)	A' A''	
T_x, T_y	ν_3, ν_4	E'	E (T_x, T_y)	F'' E' E''	T

in the group T_h^6 are shown in this table. The selection rules for m_h^6 group show that only the triply degenerate species F'' is infrared active. Thus the modes ν_1, ν_2, ν_3' and ν_4 have one component each which is triply degenerate and is infrared active.

It is clear from figs 4.18 and 4.19 that only one component at 200°C i.e in the cubic phase III is observed in each of the cases. The components due to sites of set II in phase IV in each of the modes ν_1, ν_2, and ν_4 seem to have disappeared and the remaining two components due to site I in phase IV seem to have combined to give rise to one triply degenerate component in each case. This is probably due to the reduction in the sets of sites from two to one as we go from phase IV to III.

It is seen from fig. 4.20 that as the temperature is raised in phase III the fundamental modes ν_1, ν_2' and ν_4' go on diminishing in intensity. At 207°C their intensity has gone down so much that to observe them in this phase the reference beam in the double-beam spectrophotometer has to be attenuated using Perkin Elmer attenuator attachment. By referring to table 4.5 we can see that in phase IV as the temperature is raised from room temperature to 100°C the frequencies ν_1, ν_2 and ν_4' change by a maximum of 1 cm^{-1} whereas at 200°C i e. in going to phase III the change is 3 cm^{-1} to

5.5 c.$^{-1}$. This comparatively large change in frequencies may be

attributed to the phase transformation IV→III which involves a

sudden increase in volume at the phase change and hence weakening

of the molecular bonds. Also at the phase change a slight increase

in intensity of the fundamental absorptions is observed. This may

also be understood on the basis of volume expansion at the phase

transition. The amplitude of vibrations of the NO_3^- ion could

increase, thus enhancing the intensity of the infrared absorption.

5.4.3 Phase II.

As the temperature is raised above $220^{\circ}C$ phase II appears.

As already pointed out, the absorption bands became too weak to be

observed without attenuation at temperatures above $207^{\circ}C$. Therefore,

infrared spectra in phase II at different constant temperatures in

the range $230^{\circ}C$ upto $280^{\circ}C$ have been obtained using the techniques

described by Greenburg and Hallgren[52] as well as by suitable

attenuation of the reference beam (section 4.5).

It is evident from figs. 4.18 and 4.19 that no fundamental

absorption peaks are seen at $230^{\circ}C$ and $275^{\circ}C$ i.e. in phase II.

This shows that the fundamental modes of vibration vanish in phase II.

This may be discussed as follows.

Brown and McLaren[4] have proposed that $RbNO_3$ exists in the tetragonal symmetry in phase II above $220^{\circ}C$. The space group of this phase is not known. However, the point groups C_4, C_{4h}, D_4 and D_{2d} of the tetragonal system may be taken as the possible symmetry groups for phase II. In order that these possible point groups are realized in phase II the requirement of C_4 axis of symmetry in C_4, C_{4h} and D_4 point groups and of S_4 in point group D_{2d} requires a change in the position and orientation of NO_3^- planes. A possible model based on such orientational effects may be used to explain (1) a sharp decrease in electrical conductivity at the III$\rightarrow$II transformation, and (2) the difference in the thermal expansion measured by dilatometric and X-ray methods. This may be further supported by the observation of Kennedy[5] that after III$\rightarrow$II transformation recrystallization of $RbNO_3$ takes place in phase II. Now the symmetry species of D_{3h} symmetry of the NO_3^- ion do not reduce to any of those in the tetragonal point groups cited above. The reason for this is that the common symmetry elements are no more than the identity. Hence no spectrum is observed in this phase.

As seen in section 5.2, a hexagonal (or rhombohedral) symmetry seems more probable for phase II. However, in the absence of detailed structural analysis of this phase, it is not possible to

analyse the infrared spectrum in this phase.

5.4.4 Phase I:

When $RbNO_3$ is heated above $285^{\circ}C$ phase I appears. It has cubic symmetry but no structural determination has been reported so far

Figs 4.18 and 4.19 (at $294^{\circ}C$) show that the absorption peaks at fundamental frequencies reappear. Greenberg and Hallgren[52] have also observed the infrared spectrum of $RbNO_3$ at $25^{\circ}C$ less than the melting point of $RbNO_3$ (m.p. = $310^{\circ}C$). The present observation shows that their spectrum is in cubic phase I.

Whereas no spectrum could be observed in phase II, a spectrum could be recorded on heating to higher temperatures to obtain phase I. This appears to indicate a gradual disordering of the NO_3 groups due to the phase transformation. Such a picture is consistent with the gradual increase in electrical conductivity at the II $\rightarrow$ I transition.

The frequencies observed in the spectrum of phase I are near the ones in the room temperature spectrum, suggesting that the fundamental frequencies of the NO_3 group persist in phase I. A more detailed analysis of the infrared spectrum of phase I, however, has to await a determination of the structure of the cubic phase.

5.4.5 Liquid Phase:

Greenberg and Hallgren[52] have also observed the infrared spectrum of $RbNO_3$ in liquid phase (25°C above the melting point). This spectrum was found to be essentially similar to the one of phaseI, indicating that in both cases the fundamental frequencies of the NO_3 groups are the ones being observed.

5.4.6 Solid Solutions:

In the solid solutions the spectra at room temperature (figs. 4.21 and 4.22) show that ν_1, ν_2 and ν_4 frequencies shift to lower frequencies with Cs^+ impurity (larger cation size) and to higher frequencies with K^+ impurity (smaller cation size). As already referred to, Greenberg and Hallgren[52] in their study of infrared spectra of alkali metal nitrates have observed a similar shifting of ν_1, and ν_4 frequencies but the opposite behaviour for the mode ν_2. The shifts in fundamental frequencies (table 4.6) observed by substituting Cs^+ or K^+ for Rb^+ are very small Therefore it is not possible to verify the conclusions of Greenberg and Hallgren[52] by the present study which.involves partial substitution of cations whereas Greenberg and Hallgren's[52] study is about the complete substitution of cations.

Also in general the intensities of absorption peaks of fundamentals reduce by Cs^+ substitution and get enhanced during K^+

substitution (figs. 4 21 and 4.22). This may be understood as follows. Substitution of the smaller K^+ ion for Rb^+ ion provides more available space for NO_3^- ion in the lattice and hence increases the amplitude of vibration of NO_3^- ion which leads to an increase in the intensity of the fundamentals of NO_3 group. The reverse should be expected in case of substitution of larger Cs^+ for Rb^+.

It may also be seen in fig. 4.22 that the low frequency component, of split components of E species, is more prominent in $RbNO_3$ as compared to the other at higher frequency. The prominence of the low frequency component is enhanced by Cs^+ substitution whereas it is reduced by K^+ substitution. Instead, the component at higher frequency becomes more prominent in the K^+ substitution.

The modes of vibration of NO_3^- ion in the solid solutions change with temperature in different phases in a manner similar to $RbNO_3$. They have been studied but not presented here.

5.5 Electrical Conductivity Changes and Mechanisms of Phase Transformations in $RbNO_3$.

5.5.1: Electrical Conductivity Changes at Phase Transitions in $RbNO_3$.

It was seen in section 1.3 (fig 1.4) that, from the conductance measurements on powder pellets of $RbNO_3$, Brown and McLaren[4] made the following observation: The transformation IV → III

increases the conductivity of $RbNO_3$ by a factor of about 100 and
III$\rightarrow$II transition decreases it by a factor of 3. After completing
III$\rightarrow$II transformation (for the first time), if the sample is cooled,
III$\rightleftharpoons$II transformation involves a change of conductivity by a factor
of 30 and IV$\rightleftharpoons$III transformation by a factor of 1000. These latter
changes in conductivity are repeatable after traversing III$\rightarrow$II
transformation for the first time (earlier changes in conductivity
being no more observable). This permanent increase in the conductivity
of phase III after first undergoing III$\rightarrow$II transition, however,
remained unexplained.

In the present experiments a conductivity change by a
factor of 100 at IV$\rightleftharpoons$III transition and by a factor of 3 at III$\rightleftharpoons$II
transformation was never observed, as seen in the lower most graph of
figs. 4.1 and 4.2. This suggests that, in the powder pellets of
Brown and McLaren[4], some recrystallization took place after traver-
sing III$\rightarrow$II transformation This was not the situation when the
first change of conductivity, by a factor of 100 at IV$\rightleftharpoons$III trans-
formation and by a factor of 3 at III$\rightarrow$II transition, was observed.
Recrystallization of phase II, after III$\rightarrow$II transformation, has
been recently reported by Kennedy[5]. Therefore, no such discrepancy
in conductivity change at IV$\rightleftharpoons$III transformation was observable, when

samples of the present study were prepared, as already explained.

5.5.2 Mechanisms of Phase Transformations in $RbNO_3$.

A brief discussion of the mechanisms of phase transformations
in $RbNO_3$ may be given in the light of the present study and the
available literature on phase transitions of $RbNO_3$.

5.5.3 IV ⟶ III Transformation:

The hexagonal structure for the room temperature phase
of $RbNO_3$, reported by Pauling and Sherman[68], is reproduced in
Fig. 5.14 From this figure it is evident that the NO_3 group has two
sets of sites (or orientations). Two thirds of the NO_3^- ions have
symmetry C_s (which could remove the possibility of disorder) and the
remaining third have a symmetry C_{3v}[49]. Fig. 5.15 is drawn, following
Borhman[11], for the cubic structure of phase III. In this figure
it can be seen that there are four equivalent orientations of
symmetry C_{3v} available to the NO_3 groups in the unit cell. During
the transformation IV⟶III the symmetry of all orientations increases
to C_{3v} leading to disorder. This means that phase III is disordered
with respect to phase IV in terms of the orientations of the NO_3 groups.

The orientational disordering of NO_3 group in phase III
may be partly responsible for the increase in electrical conductivity
at IV⟶III transformation in $RbNO_3$. The increase in electrical

Oxygen atom Rubidium atom

• Nitrogen atom
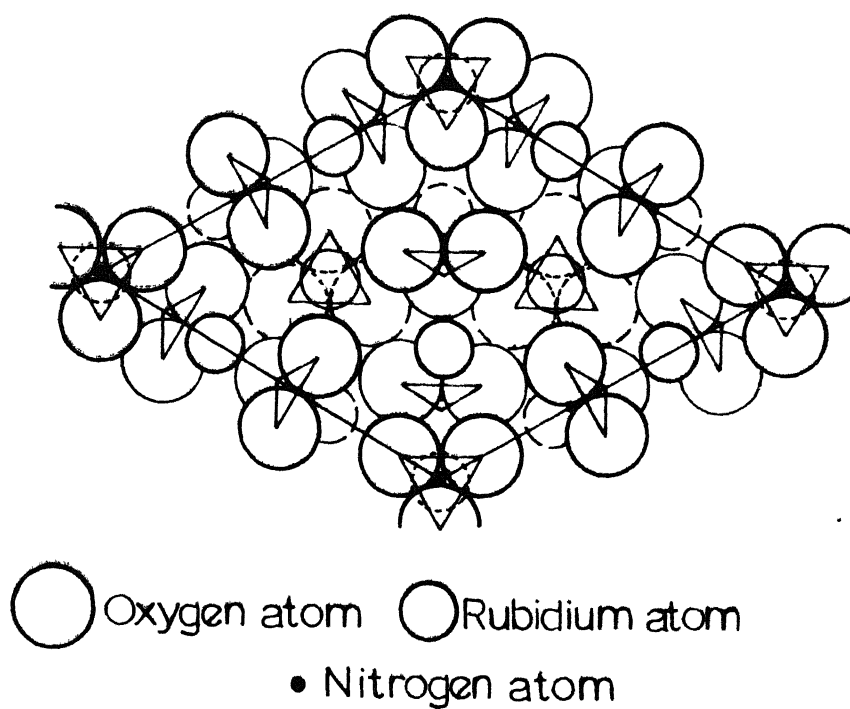
Fig. 5.14 Hexagonal crystal structure of phase IV of RbNO$_3$ (ref. 68). Rubidium and Oxygen atoms are in an approximate cubic-close-packed arrangement; their distribution among the three superposed layers shown is indicated by dark, light and dashed circles.
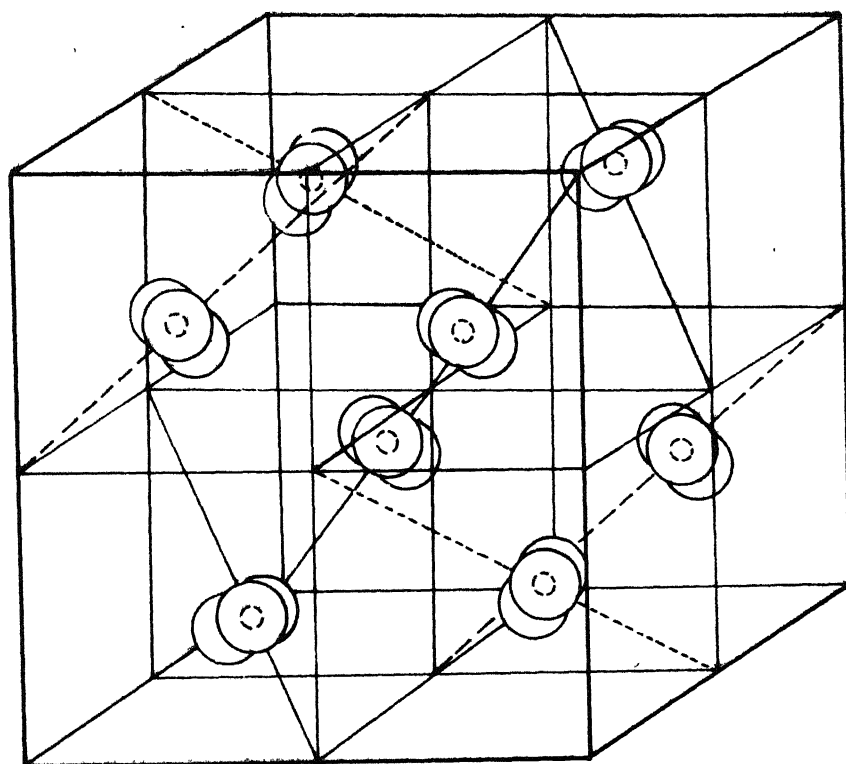
◯ Oxygen atom

◌ Nitrogen atom

Fig. 5. 15 Structure of $RbNO_3$ in cubic phase III (following

Korhonen[11]). The Rubidium ions are at the
corners of the small cubes (not shown) and NO_3^-

ions are shown on the body diagronals of the
small cubes. The plane of NO_3^- ion is perpendicular
to the body diagonal.

conductivity at this transformation is very large and hence the
orientational disordering of NO_3 group may not alone be responsible
for this The suggestion of Brown and McLaren[4] is that this large
increase in electrical conductivity may be due to the randomization
of the Rb^+ ions at this transformation. The latter proposal has been
made on the basis of the following considerations.

The crystallographic relationship between phases II and I
of $TlNO_3$ is analogous to that existing between phases IV and III of
$PbNO_3$. This is clear from the following comparative study of $TlNO_3$
and $RbNO_3$[16].

$TlNO_3$	$RbNO_3$
(i) Electrical conductance increases by a factor of 100 at II $\rightarrow$ I transformation.	(i) Corresponding increase is by a factor of 1000 at IV $\rightarrow$ III transformation.
(ii) Phase II is hexagonal with a=10.47A$^\circ$ c=7.52A$^\circ$ and Z=9.	(ii) Phase IV is trigonal with a=10.49A$^\circ$, c=7.44A$^\circ$ and Z = 9.
(iii) Five lines in the X-ray powder pattern of phase I in the range $15^\circ \angle 2\theta \angle 50^\circ$ are identical with five strongest lines in the pattern	(iii) Four lines in the X-ray powder diffraction pattern of phases III and IV as given in table 5.13

of phase II, the slight shift to lower Bragg angles is due to the thermal expansion.

are similarly identical, with a slight shift in Bragg angles due to thermal expansion.

Rowland and Bromberg[77] show by thallium magnetic resonance that Tl^+ ion has mobility in phase I as high as in the melt of $TlNO_3$. This suggests that large increase in conductance at $II \rightarrow I$ transformation in $TlNO_3$ is due to the positional disorder of Tl^+ ion

TABLE 5 13 'd' values and indices of four similar lines in phases IV and III of $PbNO_3$.

Phase IV (Temperature 124°C)		Phase III (Temperature 170°C)	
d(A^O)	h k l	d(A^O)	h k l
4.308	111	4.347	100
3.044	300	3.074	110
2.509	221	2.509	111
1.935	303	1.944	210

Therefore, it seems reasonable to assume that, associated

with the orientational disordering of the NO_3^- ions is some amount of positional randomization of the Rb^+ ions. This hypothesis receives support from the following observation (section 1.3) of Kennedy[17] (Chaplin and Kennedy). On annealing phase III (after IV $\longrightarrow$ III transformation) for 20 hours, changes in X-ray reflections correspond to changes of 20 to 40% in the ionic conductivity of $RbNO_3$ crystals. Since the X-ray reflections are mostly affected by the positions of Rb^+ ions, therefore, about 40% of the change in conductivity might be due to the randomization of Rb^+ ions.

As seen in section 1.7 Myasnikova and Yatsenko[53] have recently reported that the internal vibrations of the NO_3^- ion in $RbNO_3$ contribute very little to the change in dielectric constant at IV $\longrightarrow$ III transition and that the main contribution is from the structure vibrations. Dentsiger and Fesenko[26] have remarked that changes of dielectric constant at the transition temperatures do not correspond to the changes in electrical conductivity in $RbNO_3$. It is, therefore, clear that the change in electrical conductivity is not completely due to the positional randomization of Rb^+ ions which mainly control the lattice vibrations. Hence IV $\longrightarrow$ III transformation seems to be of the order-disorder type.

While a diffuse X-ray scattering study of phase III
might throw some additional light on the disordering of the NO_3^-
ion, experiments on IV → III transformation in the far-infrared
region might help to find out the changes in lattice modes
involving randomization of Rb^+ ions during the transformation.

5.5.4 III → II transformation:

We have seen in section 4.5 that no infrared absorption
spectra is observed in phase II of $RbNO_3$. This is explained on
the basis of ordering of NO_3 groups in phase II Dantsizer[61]
also proposes antiferroelectric properties in phase II on the
assumption of ordering of NO_3 groups.

This ordering process may be responsible for the sharp
decrease in electrical conductivity at III → II transformation.
The ordering of NO_3 groups is probably responsible for the
observation of Kennedy[5] that recrystallization takes place in
phase II after III → II transformation However, the suggestion
of Brown and McLaren[4] is that Rb^+ ions (probably) are getting
ordered in phase II

It was concluded, while explaining the difference
between the thermal expansion plots obtained from dilatometric
and X-ray studies (section 5.1), that preferred orientation takes

place of the III → II transformation   This observation seems to

be consistent with the reconstructive nature of this transformation

as reported by Kennedy [5]

5.5.5   II → I transformation:

In the infrared absorption spectra of $PbNO_3$ at $285^{\circ}C$

(not shown in the text) the strong band at the position of funda-

mental mode ν_2 of NO_3^- ion in $PbNO_3$ made a slight appearance.

This band got enhanced at $290^{\circ}C$ and $294^{\circ}C$

This re-appearance of the infrared spectrum in phase I

is explained (section 5.3) on the basis of gradual disordering

of the NO_3 groups due to the phase transition II → I in $RbNO_3$.

This gradual disordering process seems to be responsible for the

gradual increase in electrical conductivity at this transformation.

The gradual nature of this transition is also clear from dilato-

metric curves (uppermost curve of fig. 4.10).

Kennedy [5] has also concluded this transformation as

one of gradual order-disorder. The basis of his conclusion is

the progressive fading of some of the X-ray reflections and changes

in the intensity of others as the transformation I → II is traversed

in (probably) single crystals of $RbNO_3$.

REFERENCES

1. B. Cleaver, E. Rhodes and A.R. Ubbelhode, Proc. Roy. Soc. A276, 437 (1963).

2. B. Cleaver, E Rhodes and A.R. Ubbelohde, Proc. Roy. Soc. A276, 453 (1963)

3. A.C. McLaren, Rev. Pure Appl Chem. 12, 54 (1962).

4. R.N Brown and A.C. McLaren, Acta Cryst 15, 974 (1962).

5. S.W Kennedy, Nature 210, 936 (1966).

6. P. Süe, J Pauly and A. Nouaille, Bull. Soc Chim. France, 5, 593 (1958).

7. R.A. Schroeder, C.E. Weir, and E.R. Lippincott, J. Research NBS 66A, 407 (1962).

8. V E Plyushchev, I.B. Markina and L.P. Shklover, Proc. Zhur. Neorg. Khim. 1, 1613 (1956).

9. A P Rostkovskii, J. Russ. Phys. Chem. Soc. 62, 2067 (1930).

10. C. Finbak and O. Hassel, Z. Phys. Chem. (B)35, 25 (1937).

11. U. Korhonen, Ann. Acad. Sci. Fennicae, Series A, I, No. 102, 37 pp. (1951).

12. H.F Fischmeister, J. Inorg Nuclear Chem. 3, 182 (1956).

13. C. Finbak, O. Hassel and L.C. Strømme, Z. Phys. Chem. B37, 468(1937).

14. J.H. Patterson, Thesis, 1959; Ph.D. Thesis, Adelaide University, 1962.

15. R.N. Brown and A.C. McLaren, Proc. Roy. Soc. A266, 329 (1962).

16. R.N. Brown and A.C McLaren, Acta Cryst. 15, 977(1962).

17. S.W. Kennedy, G F. Taylor, and (in part) J.H. Patterson, phys. stat. Sol. 16, K175 (1966).

REFERENCES (Continued)

18. P. I. Protsenko, N.P. Popovskaya, Z.I. Belova, A.V Protsenko, O.N. Shokina, and R.P. Shisholina Tr. Vses. Sovrhch. po Fiz - Khim. Resplavln. Solei, 2nd, Kiev. 1963, 55 (1965) (Russ.).

19. V.P. Shcedov and I.A Invanov. Elektrokhimya, 3, 95 (1967).

20 I.G. Murgulescu, et al., Rev. Roumaina Chim., 11, 1031 (1966).

21 F.R. Duke and G. Victor, J Electrochem. Soc. 110, 91(1963).

22 J.A A. Ketelaar and E P. Honig, J. Phys. Chem. 68, 1596(1964).

23. J.A A. Ketelaar and J.C. Th. Kwak, J. Phys.Chem.71, 1149(1967).

24. P.I. Protsenko and O.N.Razumovskaya, Zh. Prikl. Khim., 38, 2355 (1965).

25. A. Ya Dantsiger, Nauchn. Konf. Aspirantov, 75 (1962).

26 A. Ya Dantsiger and E.G. Fesenko, Soviet Phys.- Cryst. 8, 717 (1964).

27 I.S. Zheludev and A.S. Sonin, Bull. Acad. Sci. USSR. Phys. Series 22, No. 12, 1435 (1958).

28 A S. Sonin and I.S. Zheludev, Soviet Phys -Cryst. 8, 219 (1963).

29. A.S. Sonin, I.S. Zheludev and G.F Dobrzhanskii Izv. ANSSSR, Ser. fiz., 24, 1209 (1960).

30. P.I. Protsenko, A.L Khodakov, E.Z. Mirskaya, and L.N. Venerovskaya. Ferroelectrics (in Russian), publ. Rostov-on-Don University, p.21 (1961).

31 A.Ya Dantsiger and E.G. Fesenko, Soviet Phys.-Cryst. 10, 272 (1965).

32. S. Sawada, S. Nomura and Y. Asao, J Phys. Soc. Japan, 16, 2486 (1961).

33. C. Finbak and O. Hassel, J Chem.Phys. 5, 460(1937).

34. E. Rapoport, J. Phys. Chem. Solids 27, 1349(1966).

REFERENCES (Continued)

35. P.W. Bridgman, J Phys Chem.Solids, 27, 1349(1966).

36. P.W. Bridgman, Proc.Am Acad. Arts Sci. 51, 582 (1916).

37. E. Rapoport and G.C. Kennedy, J.Phys.Chem.Solids, 27, 93(1966).

38. Handbook of Chemistry and Physics, 1957.

39. H. Schinke and F. Sauerwald, Z.anorg. u. allgem.Chem. 304, 25 (1960).

40. P.W Bridgman, Proc.Am. Acad. Arts Sci 51, 603 (1915).

41. J. Peyhonen, T. Sivonen and M. Hilpela, Ann Acad. Sci. Fennicae, Ser A, VI, No. 170,8pp (1964).

42. H. Spindler and F Saueriwald, Z. Anorg. Allgem. Chem., 335, 267 (1965).

43. B.B. Owens, J. Chem. Phys. 42, 2259(1965).

44. A Mustajoki, Ann. Acad. Sci. Fennicae, Ser. A, VI, No. 9, pp 3-16 (1958).

45. A. Arell and M. Varteva, Ann Acad. Sci. Fennicae, Ser. A.VI, 88, 8 pp. (1961).

46. S. Gordon and C. Campbell, Anal. Chem. 27, 1102 (1955).

47. K. J. Rao and C.N.R. Rao, J. Material Science, 1, 238(1966).

48. V.P. Vasil'ev and V.N. Vasil'eva Zh. Fiz. Khim. 36,2517(1962).

49. D.M. Newsand and L.A.K Staveley, Chem.Rev. 66, 267 (1966).

50. M.F.C. Ladd and W.H Lee, J. Inorg. and Nucl. Chem.,13,218(1960).

51. F. Vranty, Appl. Spectroscopy, 13, 59 (1959).

52. J. Greenberg and L.J. Hallgren, J. Chem. Phys. 33, 900(1960).

53. T.P. Myasnikova and A.F. Yatsenko, Soviet Phys. - Solid State, 8, 2252(1967).

54. N.A. Puschin and M. Radoičić: Z.anorg allgem. chem.233, 41 (1937).

55. R.G. Samuseva and V.E. Plyuschev, Zh. Neorg. Khim. 12, 220(1967).

REFERENCES (Continued)

56 U. Kawabe, T. Yanagi and S. Sawada, J. Phys. Soc. Japan, 19, 767 (1964).

57. U. Kawabe, T. Yanagi and S. Sawada, J. Phys. Soc. Japan 20, 2059 (1965).

58. A. Ya Dantsiger, Bull. Acad USSR, 29, 1043 (1965).

59. A. Ya Dantsiger and I A Freizon, Soviet Phys.- Solid State, 7, 1762 (1966).

60 V. F Blidin, Izv SPKhA, 23, 233 (1953).

61 A. Ya Dantsiger, Soviet Phys.- Solid State, 7, 1845 (1966).

62 S. Gordon, J. Chem. Ed., 40, A87 (1963).

63 F. M Wahl, R. E. Grim and R. B. Graf, Am. Mineral. 46, 196 (1961).

64 C. J. Schneer and R. W. Whiting, Am. Mineral 48, 737 (1963).

65. F. Vranty and B. Graves, Revs. Sc. Instrm. 31, 65 (1960).

66. H. J. Borchardt and F. Daniels, J Am. Chem. Soc. 79, 41 (1957).

67 K. J. Rao, G. V. S. Rao, and C. N. R. Rao, J. Phys. Chem. Solids (in press).

68. L. Pauling and J. Sherman, Z. Krist. A84, 213 (1933).

69 A. R Ubbelohde, "Melting and Crystal Structure", Clarendon Press: Oxford (1965).

70. International Critical Tables.

71. G. Herzberg, 'Infrared and Raman Spectra of Polyatomic molecules', D. Van Nostrand Co., Inc., New York, 1964.

72. D. M. Gage and E. F. Barker, J. Chem. Phys. 7, 455 (1939).

73 G. Ferrari et al, Gazz. Chim. Ital. 87, 630 (1957).

74. C. Finbak and O. Hassel, SBV, 83 (1937).

75 F. C. Kracek et al, SBII, 381 (1932).

76 R. Kato and Rolfe, J. Chem Phys. 47, 1901 (1967).

77 T. J. Rowland and J P. Bromberg, J Chem. Phys. 29, 626 (1958).

APPENDIX

A. Calculation of Heat of Transition $\triangle H$ from the DTA Peak.

Let m_1 gms. of a standard material (say $RbNO_3$ in this case) of molecular weight M_1 be packed in one of the holes of the metal block of DTA apparatus. The quantity of heat released by $\dfrac{m_1}{M_1}$ moles of the standard material is $\dfrac{m_1}{M_1} H$ cals., where H cals/mole is the heat of transformation of the standard material. This quantity of heat is represented by area A_1 of the DTA peak for $RbNO_3$.

Let the other hole of the metal block of the DTA apparatus be packed by an equal volume of the sample substance (solid solutions in this case). Let the weight of the substance taken be m_2 gms and molecular weight be M_2. Therefore $\dfrac{m_2}{M_2}$ moles of the substance correspond to an area A_2 of the DTA peak A_2 is equivalent to $H\dfrac{m_1}{M_1}\dfrac{A_2}{A_1}$ cals. of heat. This heat is released by $\dfrac{m_2}{M_2}$ moles of the substance. Therefore one mole will release $H\dfrac{m_1 A_2}{M_2 A_1}\dfrac{M_2}{M_1}$ or

$$\triangle H = H\dfrac{m_1 A_2}{m_2 A_1}\dfrac{M_2}{M_1}$$

B. Calculation of Energy of Activation E_a from the DTA Curves

Rate constant of a reaction (or thermal transformation) is given by (Arrhenius rate equation)

$$k = C \ e^{-E_a/RT}$$

$$\text{or } \log_e k = {}^{-E}a/RT \ + \log_e C \tag{1}$$

where E_a is the energy of activation for the transformation,

R the gas constant, T the absolute temperature and C is a

constant. $\log k$ at different temperatures are calculated

from the DTA peak and a plot of $\log k$ vs $1/T$, called the

activation energy plot, is obtained. From the slope of this

plot, which is a straight line plot, E_a is calculated.

From (1),

$$\frac{E_a}{2.303R} = \text{Slope of activation energy plot}$$

$$E_a = 2\ 303\ R\ (\text{Slope of activation energy plot}).$$

C. Calculation of the Magnification of the Dilatometer.

Let O, S and T (fig (b)) represent the

(a)   (b)
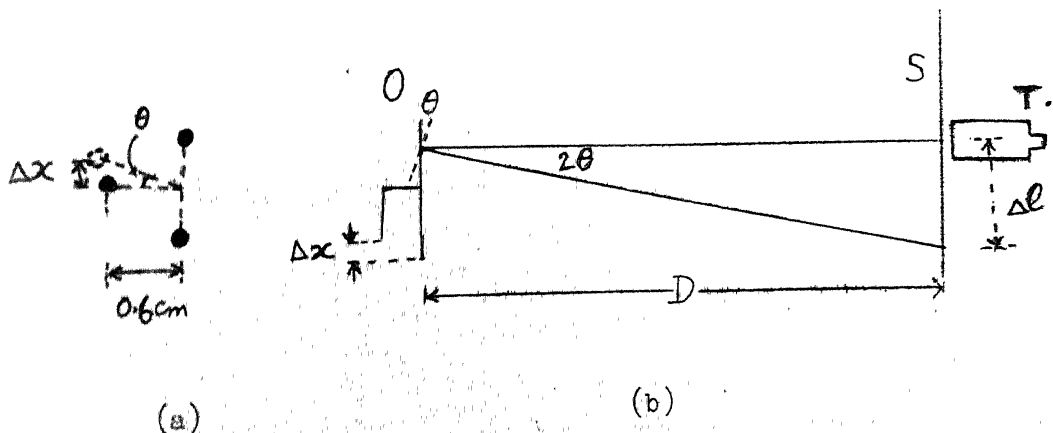
Fig. Optical lever arrangement in the dilatometric
experiment

optical lever, vertical scale and the telescope respectively

in the dilatometric experiment   The solid circles in fig (a)

represent the foot prints of the optical lever.

Suppose the central leg of the optical lever is

displaced (from solid circle to open circle fig.(a) vertically

by a distance Δx. This tilts the mirror of the optical

lever (fig (b) by an angle ϕ resulting in a shift of 2 θ for the

optical beam from the telescope. From the geometery of the

figure (b) it is evident that

$$\tan 2\phi = \frac{\Delta l}{D}$$

where 2 ϕ and D are shown in the figure. Since 2ϕ is very

small, we can write

$$2\theta = \frac{\Delta l}{D}$$

$$\therefore \phi = \frac{\Delta l}{2 D}$$

Also from fig (a),

$$\phi = \frac{\Delta x}{0.6}$$

where 0.6 cm is the distance shown in the figure.

$$\therefore \Delta x = 0.6 \; (\phi)$$

$$= 0.6 \; \frac{\Delta l}{2 D}$$

The distance D, between the optical lever and the scale, was

measured as 136 cm in the experimental set up.

$$\therefore \Delta x = 0.6 \; \frac{\Delta l}{2 \times 136}$$

$$\therefore \text{Magnification} = \frac{\Delta l}{\Delta x} = \frac{2 \times 136}{0.6}$$

D. Conductivity Data.

TABLE. D1. Conductivity data during heating and cooling for $RbNO_3$

$T(^\circ K)$	$\frac{1000}{T}(^\circ K)^{-1}$	Conductivity$(\Omega-cm)^{-1}$ Heating	$T(^\circ K)$	$\frac{1000}{T}(^\circ K)^{-1}$	Conductivity $(\Omega-cm)^{-1}$ Cooling
403	2.4814	1.68×10^{-7}	405	2.4690	3.19×10^{-7}
413	2.4213	1.83 "	407	2.4570	3.48 "
423	2.3641	3.17 "	409	2.4440	4.17 "
427	2.3419	3.57 "	413	2.4213	5.49 "
429	2.3310	4.39 "	415	2.4096	7.06 "
430	2.3250	6.80 "	417	2.3981	1.19×10^{-6}
431	2.3202	9.52 "	418	2.3920	1.66 "
432	2.3140	1.90×10^{-6}	419	2.3866	2.72 "
433	2.3095	7.52 "	420	2.3800	9.06 "
434	2.3040	2.83×10^{-5}	421	2.3753	2.30×10^{-5}
435	2.2989	5.29 "	422	2.3690	1.97×10^{-4}
436	2.2930	7.52 "	423	2.3641	2.34 "
437	2.2883	2.04×10^{-4}	425	2.3529	2.94 "
438	2.2830	2.38 "	427	2.3419	3.36 "
439	2.2779	2.38 "	429	2.3310	3.57 "
441	2.2670	2.86 "	433	2.3095	4.28 "
443	2.2573	3.17 "	443	2.2573	6.54 "
445	2.2472	3.57 "	453	2.2075	9.83 "

T(°K)	$\frac{1000}{T}(°K)^{-1}$	Conductivity $(\Omega\text{-cm})^{-1}$ Heating	T(°K)	$\frac{1000}{T}(°K)^{-1}$	Conductivity $(\Omega\text{-cm})^{-1}$ Cooling
447	2.2371	4.08×10^{-4}	463	2.1598	1.41×10^{-3}
453	2.2075	5.71 "	467	2.1413	1.61 "
463	2.1598	6.50 "	471	2.1231	1.88 "
473	2.1142	1.19×10^{-3}	472	2.1180	1.96 "
483	2.0704	1.59 "	473	2.1142	1.97 "
489	2.0450	2.04 "	474	2.1090	2.04 "
493	2.0284	2.28 "	475	2.1053	5.10×10^{-4}
495	2.0202	2.38 "	476	2.1000	3.17 "

T(°K)	$\frac{1000}{T}$(°K)$^{-1}$	Conductivity (Ohm-cm)$^{-1}$ Heating	T(°K)	$\frac{1000}{T}$(°K)$^{-1}$	Conductivity $(\mho$-cm)$^{-1}$ Cooling
496	2.0160	2.38×10^{-3}	477	2.0964	1.10×10^{-4}
497	2.0121	2.42 "	479	2.0877	3.64×10^{-5}
498	2.0080	2.28 "	480	2.083	2.74 "
499	2.0040	5.49×10^{-4}	481	2.0790	1.48 "
500	2.0000	2.13 "	483	2.0704	1.26 "
501	1.9960	1.14 "	489	2.0450	1.45 "
502	1.9920	7.71×10^{-5}	493	2.0284	1.61 "
503	1.9881	4.86 "	497	2.0121	1.83 "
504	1.984	3.86 "	503	1.9881	2.16 "
505	1.9802	3.08 "	507	1.9724	2.46 "
506	1.976	2.28 "	511	1.9569	2.77 "
507	1.9724	2.30 "	513	1.9493	2.93 "
513	1.9493	2.36 "	514	1.9450	3.04 "
519	1.9268	2.67 "	515	1.9417	3.10 "
523	1.9120	2.60 "	516	1.9370	3.24 "
525	1.9048	3.04 "	517	1.9342	3.36 "
526	1.9010	3.14 "	519	1.9268	3.48 "
527	1.8975	3.21 "	521	1.9194	3.64 "
528	1.8930	3.28 "	522	1.9150	3.76 "

T(°K)	$\frac{1000}{T}(°K)^{-1}$	Conductivity (Ohm-cm)$^{-1}$ Heating	T(°K)	$\frac{1000}{T}(°K)^{-1}$	Conductivity (Ω-cm)$^{-1}$ Cooling
529	1.8904	3.36×10^{-5}	523	1.9120	3.91×10^{-5}
533	1.8762	3.81 "	524	1.9080	4.08 "
535	1.8691	4.08 "	525	1.9048	4.20 "
539	1.8553	4.61 "	526	1.9010	4.33 "
543	1.8416	5.10 "	527	1.8975	4.46 "
549	1.8215	6.42 "	528	1.8930	4.61 "
551	1.8149	7.32 "	529	1.8904	4.76 "
552	1.8110	7.52 "	530	1.8860	4.84×10^{-5}
553	1 8083	8.40 "	531	1.8832	4.92 "
554	1.8050	8.93 "	532	1.8790	5.15 "
555	1.8018	1.02×10^{-4}	533	1.8762	5.39 "
556	1.7980	1.10 "	534	1.8720	5.60 "
557	1.7953	1.30 "	535	1.8691	6.21 "
558	1.7920	2.04 "	536	1.8650	6.42 "
559	1.7889	2.38 "	537	1.8622	6.64 "
560	1.7850	2.36 "	538	1.8580	6.88 "
561	1.7825	2.91 "	539	1.8553	7.14 "
562	1.7790	3.24 "	540	1.8510	7.72 "
563	1.7762	3.24 "	541	1.8484	8.40 "

$T(^\circ K)$	$\frac{1000}{T}(^\circ K)^{-1}$	Conductivity (Ohm-cm)$^{-1}$ Heating	$T(^\circ K)$	$\frac{1000}{T}(^\circ K)^{-1}$	Conductivity (Ω-cm)$^{-1}$ Cooling
564	1.7730	3.52×10^{-4}	543	1.8416	1.26×10^{-4}
567	1.7637	–	547	1.8282	2.72 "
571	1.7513	8.05×10^{-4}	553	1.8083	1.78×10^{-3}
573	1.7452	8.93 "	557	1.7953	2.13 "
575	1.7391	1.19×10^{-3}	563	1.7762	3.62 "
577	1.7331	3.24 "	573	1.7452	4.39×10^{-2}
579	1.7271	5.35 "	575	1.7391	5.95 "
581	1.7212	1.63×10^{-2}	579	1.7271	6.21 "
583	1.7153	3.17 "	583	1.7153	4.76 "

TABLE.D2 Conductivity data during heating and cooling for $K_{0.05}Rb_{0.95}NO_3$

$T(^\circ K)$	$1000/T(^\circ K)^{-1}$	Conductivity $(\Omega\text{-cm})^{-1}$	
		Heating	Cooling
373	2.6809	1.08×10^{-7}	−
393	2.5445	1.06 "	1.37×10^{-7}
403	2.4814	1.10 "	1.31 "
407	2.4570	1.04 "	1.34 "
411	2.4331	1.08 "	1.37 "
413	2.4213	1.03 "	−
415	2.4096	1.01 "	1.48 "
417	2.3981	1.06 "	1.63 "
419	2.3866	1.10 "	1.60 "
421	2.3753	1.08 "	1.71 "
423	2.3641	1.14 "	1.86 "
425	2.4529	1.07 "	1.97 "
427	2.3419	1.10 "	2.18 "
429	2.3310	1.17 "	2.48 "
431	2.3202	1.23 "	3.14 "
433	2.3095	1.26 "	4.86 "
435	2.2989	1.37 "	7.14 "
437	2.2883	1.43 "	1.80×10^{-6}

$T(^\circ K)$	$1000/T(^\circ K)^{-1}$	Conductivity $(\text{ohm-cm})^{-1}$	
		Heating	Cooling
439	2.2779	4.28×10^{-7}	6.28×10^{-5}
441	2.2676	5.14×10^{-6}	1.85×10^{-4}
443	2.2573	1.40×10^{-5}	2.34 "
445	2.2472	1.97 "	2.63 "
447	2.2371	2.37 "	2.94 "
449	2.2271	2.66 "	3.14 "
451	2.2173	2.97 "	3.71 "
453	2.2075	3.43 "	4.00 "
463	2.1598	5.14×10^{-5}	6.28×10^{-4}
473	2.1142	7.43 "	9.43 "
483	2.0704	1.06×10^{-4}	1.26×10^{-3}
493	2.0284	1.57 "	1.74 "
503	1.9881	2.14 "	2.31 "
507	1.9724	2.46 "	2.57 "
511	1.9569	2.77 "	2.86 "
513	1.9493	2.94 "	2.97 "
515	1.9417	3.11 "	3.08 "
517	1.9342	3.43 "	3.43 "
519	1.9268	3.48 "	3.54 "
521	1.9194	3.48 "	3.54 "

$T(^{\circ}K)$	$1000/T(^{\circ}K)^{-1}$	Conductivity $(\Omega\text{-cm})^{-1}$	
		Heating	Cooling
523	1.9120	1.28×10^{-4}	3.71×10^{-3}
525	1.9048	1.37 "	1.71 "
527	1.8975	1.00 "	4.28×10^{-4}
529	1.8904	7.74×10^{-5}	7.14 "
531	1.8832	5.74 "	5.71 "
533	1.8762	4.28 "	4.28 "
535	1.8691	3.71 "	3.71 "
537	1.8622	3.43 "	3.43 "
543	1.8416	2.31 "	2.28 "
547	1.8282	1.94 "	1.91 "
551	1.8149	1.60 "	1.68 "
553	1.8083	1.57 "	1.68 "
555	1.8018	1.56 "	1.60 "
557	1.7953	1.57 "	1.48 "
559	1.7889	1.59×10^{-5}	1.48×10^{-4}
561	1.7825	1.74 "	1.57 "
563	1.7762	2.23 "	2.54 "
565	1.7699	3.71 "	2.54 "

$T(^{\circ}K)$	$\dfrac{1000}{T}$ $(^{\circ}K)^{-1}$	Conductivity $(\text{ohm} - cm)^{-1}$	
		Heating	Cooling
567	1.7637	4.57×10^{-5}	3.43×10^{-4}
569	1.7575	5.71 "	4.86 "
571	1.7513	8.00 "	6.86 "
573	1.7452	–	1.34×10^{-3}
575	1.7391	–	3.71 "
577	1.7331	–	8.28 "
579	1.7271	–	1.06×10^{-2}
581	1.7212	–	1.66 "
583	1.7153	–	1.91 "
585	1.7094	–	2.14 "
587	1.7036	–	2.34 "
589	1.6978	–	2.51 "
591	1.6920	–	2.54 "
593	1.6863	–	2.57 "
595	1.6807	–	2.63 "
597	1.6750	–	2.71 "
599	1.6694	–	2.71 "
601	1.6639	–	2.71 "
603	1.6584	–	2.83 "

TABLE D3. Conductivity data during heating and cooling for
$\bullet_{30.10}Rb_{0.90}NO_3$.

T(°K)	$\frac{1000}{T}$(°K)$^{-1}$	Conductivity Heating $(\Omega\text{-cm})^{-1}$	T(°K)	$\frac{1000}{T}$(°K)$^{-1}$	Conductivity Cooling $(\Omega\text{-cm})^{-1}$
393	2.5445	1.23×10^{-7}	393	2.5445	1.54×10^{-7}
403	2.4814	1.26 "	403	2.4814	1.89 "
413	2.4213	1.34 "	405	2.4690	2.20 "
417	2.3981	1.40 "	407	2.4570	2.57 "
419	2.3866	1.48 "	409	2.4450	2.86 "
421	2.3753	1.60 "	411	2.4331	3.71 "
423	2.3641	1.74 "	413	2.4213	4.28 "
425	2.3529	1.86 "	415	2.4096	5.14 "
427	2.3419	2.46 "	417	2.3981	6.00 "
429	2.3310	3.43 "	419	2.3866	6.86 "
431	2.3202	6.00 "	421	2.3753	8.28 "
433	2.3095	1.34×10^{-6}	423	2.3641	1.17×10^{-6}
435	2.2989	1.23×10^{-5}	425	2.3529	1.63 "
437	2.2883	8.57 "	427	2.3419	3.14 "
439	2.2779	1.08×10^{-4}	429	2.3310	2.28×10^{-5}
441	2.2676	1.23 "	431	2.3202	5.71 "
443	2.2573	1.31 "	433	2.3095	8.00 "

$T(°K)$	$\frac{1000}{T}(°K)^{-1}$	Conductivity Heating $(\Omega\text{-}cm)^{-1}$	$T(°K)$	$\frac{1000}{T}(°K)^{-1}$	Conductivity Cooling $(\Omega\text{-}cm)$
453	2.2075	2.00×10^{-4}	435	2.2989	1.00×10^{-4}
463	2.1598	3.14 "	439	2.2779	1.23 "
473	2.1142	4.86 "	443	2.2573	1.48 "
483	2.0704	7.14 "	453	2.2075	2.28 "
493	2.0284	9.91 "	463	2.1598	3.43 "
503	1.9881	1.41×10^{-3}	473	2.1142	5.43 "
515	1.9493	2.06 "	483	2.0704	7.71 "
523	1.9120	2.60 "	493	2.0284	1.14×10^{-3}
527	1.8975	2.91 "	503	1.9881	1.51 "
531	1.8832	3.25×10^{-3}	513	1.9493	2.14×10^{-3}
533	1.8762	3.43 "	517	1.9342	2.46 "
535	1.8691	3.62 "	519	1.9268	2.43 "
537	1.8622	3.68	521	1.9194	2.23 "
539	1.8553	2.22 "	523	1.9120	1.88 "
541	1.8484	1.29 "	525	1.9048	1.54 "
543	1.8416	8.57×10^{-4}	527	1.8975	1.28 "
547	1.8282	5.40 "	529	1.8904	1.06 "
551	1.8143	4.06 "	531	1.8832	9.14×10^{-4}

T($^\circ$K)	$\frac{1000}{T}$ ($^\circ$K)$^{-1}$	Conductivity Heating (Ω-cm)$^{-1}$	T($^\circ$K)	$\frac{1000}{T}$ ($^\circ$K)$^{-1}$	Conductivity Cooling (Ω-cm)$^{-1}$
553	1.8083	3.48×10^{-4}	533	1.8762	7.43×10^{-4}
557	1.7953	2.38 "	535	1.8691	5.31 "
559	1.7889	3.03 "	537	1.8622	2.59 "
561	1.7825	1.14×10^{-3}	539	1.8553	1.57 "
563	1.7762	2.43 "	541	1.8484	1.14 "
565	1.7699	5.71 "	543	1.8416	1.06 "
567	1.7637	1.51×10^{-2}	547	1.8282	1.06 "
569	1.7575	1.94 "	551	1.8149	1.28 "
571	1.7513	2.20 "	553	1.8083	1.57 "
573	1.7452	2.31 "	555	1.8018	3.14 "
575	1.7391	2.54 "	557	1.7953	8.00 "
577	1.7331	2.94 "	559	1.7889	2.57×10^{-3}
579	1.7271	2.87 "	561	1.7825	1.20×10^{-2}
581	1.7212	3.11 "	563	1.7762	1.48 "
583	1.7153	3.14 "	565	1.7699	1.86 "
–	–	–	567	1.7637	2.14 "
–	–	–	569	1.7575	2.51 "
–	–	–	571	1.7513	2.71×10^{-2}

$T(^{\circ}K)$	$\frac{1000}{T}\ (^{\circ}K)^{-1}$	Conductivity Heating $(\Omega - cm)^{-1}$	$T(^{\circ}K)$	$\frac{1000}{T}\ (^{\circ}K)^{-1}$	Conductivity Cooling $(\Omega - cm)^{-1}$
–	–	–	573	1.7452	2.80×10^{-2}
–	–	–	575	1.7391	2.96 "
–	–	–	577	1.7331	2.88 "
–	–	–	579	1.7271	3.00 "
–	–	–	581	1.7212	3.14 "
–	–	–	583	1.7153	3.14 "

TABLE D.4 Conductivity data during heating and cooling for $Cs_{0.20}Rb_{0.80}NO_3$

$T(^\circ K)$	$1000/T(^\circ K)^{-1}$	Conductivity $(-\Omega - cm)^{-1}$	
		Heating	Cooling
393	2.5445	1.14×10^{-7}	1.23×10^{-7}
403	2.4814	1.23 "	1.25 "
407	2.4570	1.31 "	1.23 "
411	2.4331	1.37 "	1.28 "
413	2.4213	1.37 "	1.31 "
415	2.4096	1.31 "	1.45 "
417	2.3981	1.31 "	—
419	2.3866	1.34 "	2.51×10^{-7}
421	2.3753	1.31 "	2.57 "
423	2.3641	1.31 "	8.57 "
425	2.3529	1.37 "	3.14×10^{-6}
427	2.3419	1.68 "	8.05 "
429	2.3310	3.43 "	2.17×10^{-5}
431	2.3202	9.14×10^{-6}	2.51 "
433	2.3095	1.83×10^{-5}	2.77 "
435	2.2989	2.48 "	3.17 "
437	2.2883	2.97 "	3.51 "
439	2.2779	3.43 "	3.88 "
441	2.2676	3.77 "	4.34 "
443	2.2573	4.23 "	4.85 "
453	2.2075	7.24 "	8.00 "

T(^{o}K)	1000/T(^{o}K)$^{-1}$	Conductivity (Ω--cm)$^{-1}$	
		Heating	Cooling
541	1.8484	2.02×10^{-3}	2.23×10^{-3}
543	1.8416	2.19 "	1.65 "
545	1.8349	2.28 "	1.68 "
547	1.8282	2.39 "	1.68 "
549	1.8215	2.54 "	1.51 "
551	1.8149	2.73 "	—
553	1.8083	2.85 "	—
555	1.8018	3.03 "	2.28×10^{-3}
557	1.7953	3.08 "	2.85 "
559	1.7889	3.07×10^{-3}	5.43×10^{-3}
561	1.7825	3.50 "	9.14 "
563	1.7762	4.41 "	1.26×10^{-2}
565	1.7699	8.57 "	1.97 "
567	1.7637	1.48×10^{-2}	2.31 "
569	1.7575	1.91 "	2.34 "
571	1.7513	2.17 "	2.37 "
573	1.7452	2.25 "	2.43 "
575	1.7391	2.40 "	2.43 "
577	1.7331	2.45 "	2.57 "
579	1.7271	2.48 "	2.60 "
581	1.7212	2.57 "	2.57 "
583	1.7153	2.57 "	2.57 "

TABLE D.5 Conductivity data during heating and cooling for $Cs_{0.25}Rb_{0.75}NO_3$

$T(^\circ K)$	$1000/T(^\circ K)^{-1}$	Conductivity $(\Omega\text{-cm})^{-1}$	
		Heating	Cooling
393	2.5445	1.11×10^{-7}	1.14×10^{-7}
403	2.4814	1.14 "	1.23 "
407	2.4570	1.14 "	1.43 "
411	2.4331	1.23 "	4.28 "
413	2.4213	1.21 "	8.57 "
417	2.3981	1.26 "	5.14×10^{-6}
419	2.3866	1.31 "	9.14 "
421	2.3753	1.34 "	1.20×10^{-5}
423	2.3641	1.43 "	1.37 "
425	2.3529	1.48 "	1.57 "
427	2.3419	2.03 "	1.74 "
429	2.3310	4.00 "	1.94 "
431	2.3202	9.43 "	2.20 "
433	2.3095	1.58×10^{-6}	2.46 "
435	2.2989	4.00 "	—
437	2.2883	6.57 "	—
439	2.2779	1.06×10^{-5}	—
441	2.2676	1.34 "	—
443	2.2573	1.60 "	4.28×10^{-5}
453	2.2075	3.08 "	7.14 "
463	2.1598	5.14 "	1.14×10^{-4}

T(^{o}K)	1000/T(^{o}K)$^{-1}$	Conductivity ($-\gamma-$ $-cm$)$^{-1}$	
		Heating	Cooling
473	2.1142	8.28x10^{-5}	1.77x10^{-4}
483	2.0704	1.34x10^{-4}	2.68 "
493	2.0284	2.14 "	4.60 "
503	1.9881	3.14 "	6.00 "
513	1.9493	5.14 "	8.57 "
523	1.9120	7.43x10^{-4}	1.17x10^{-3}
533	1.8762	1.06x10^{-3}	1.77 "
537	1.8622	1.20 "	2.28 "
541	1.8484	1.34 "	3.43 "
543	1.8416	1.46 "	7.43 "
545	1.8349	1.54 "	9.71 "
547	1.8282	1.66 "	1.26x10^{-2}
549	1.8215	1.77 "	1.40 "
551	1.8149	1.86 "	1.57 "
553	1.8083	1.97 "	1.74 "
555	1.8018	2.06 "	1.86 "
557	1.7953	2.23 "	1.88 "
559	1.7889	2.40 "	1.94 "
561	1.7825	2.77 "	2.00 "
563	1.7762	3.43 "	2.00 "
565	1.7699	4.00 "	2.11 "
567	1.7637	8.57 "	2.08 "

$T(^{\circ}K)$	$1000/T(^{\circ}K)^{-1}$	Conductivity $(\Omega\text{-cm})^{-1}$	
		Heating	Cooling
569	1.7575	1.14×10^{-2}	2.11×10^{-2}
571	1.7513	1.40 "	2.17 "
573	1.7452	1.54 "	2.23 "
575	1.7391	1.66 "	2.17 "
577	1.7331	1.77 "	2.14 "
579	1.7271	1.86 "	2.2 "
581	1.7212	1.91 "	2.2 "
583	1.7153	2.06 "	2.20 "

TABLE D6   Conductivity data on $Cs_{0.30}Rb_{0.70}NO_3$

T($^{\circ}$K)	1000/T($^{\circ}$K)$^{-1}$	Conductivity (Ohm-cm)$^{-1}$	
		Heating	Cooling
393	2.5445	1.14×10^{-7}	1.23×10^{-7}
403	2.4814	1.28 "	1.31 "
407	2.4570	1.28 "	2.31 "
411	2.4331	1.40 "	6.28 "
413	2.4213	1.46 "	1.06×10^{-6}
415	2 4096	1.51 "	2.17 "
417	2.3981	1.54 "	5.14 "
419	2 3866	1.60 "	1.03×10^{-5}
421	2.3753	1 80 "	1.34 "
423	2.3641	2 34 "	1.57 "
425	2.3529	4 00 "	1.86 "
427	2.3419	1.54×10^{-6}	2.08 "
429	2.3310	5.43 "	2.36 "
431	2.3202	9.71 "	2.66 "
433	2.3095	1.20×10^{-5}	2.86 "
435	2 2989	1.34 "	3.43 "
437	2 2883	1.54 "	3.71 "
43	2 2779	1.74 "	4 28 "
441	2 2676	2.06 "	4.86 "
443	2 2573	2 28 "	5.14 "
453	2 2075	3.71 "	8.86 "
463	2.1598	6.28 "	1.48×10^{-4}
473	2.1142	1.06×10^{-4}	2.37 "
483	2 0704	1.71 "	3.71 "
493	2.0284	2.71 "	5.43 "
503	1.9881	4.00 "	8.00 "

$T(^{\circ}K)$	$1000/T(^{\circ}K)^{-1}$	Conductivity $(Ohm\text{-}cm)^{-1}$	
		Heating	Cooling
513	1.9493	6.28×10^{-4}	1.14×10^{-3}
523	1 9120	9.14 "	1.60 "
527	1.8975	1.06×10^{-3}	1.80 "
529	1 8904	1.11 "	1.91 "
531	1.8832	1.20 "	2.06 "
533	1.8762	1.36 "	2.23 "
535	1.8691	1.40 "	2.37 "
537	1.8622	1.51 "	2.51 "
539	1.8553	1.60 "	2.66 "
541	1.8484	1.71 "	2.83 "
543	1.8416	1.83 "	2.80 "
545	1 8344	1.94 "	3.14 "
547	1.8282	2.06 "	3.71 "
549	1.8215	2.17 "	4.57 "
551	1 8149	2.31 "	6.28 "
553	1 8083	2.51 "	9.14 "
555	1.8018	2.63 "	1.23×10^{-2}
557	1.7953	2.83 "	1.51 "
559	1.7889	3 08 "	1.68 "
561	1.7825.	3.43 "	1.83 "
563	1 7762	4.57 "	1.88 "
565	1 7699	7.43 "	2.00 "
567	1 7637	8.71 "	2.08 "
569	1.7575	1.11×10^{-2}	2.08 "
571	1 7513	1.37 "	2.11 "
573	1.7452	1.57 "	2.31 "

T($^{\circ}$K)	1000/T($^{\circ}$K)$^{-1}$	Conductivity (Ohm-cm)$^{-1}$	
		Heating	Cooling
575	1.7391	$1\ 80 \times 10^{-2}$	2.20×10^{-2}
577	1 7331	1.91 "	2.20 "
579	1.7271	2.06 "	2.20 "
581	1 7212	2.06 "	2.26 "
583	1 7153	2 06 "	2.26 "

TABLE D7 Conductivity data on $K_{0.02}Rb_{0.98}NO_3$

T(°K)	1000/T(°K)$^{-1}$	Conductivity (Ohm-cm)$^{-1}$	
		Heating	Cooling
393	2.5445	1.11×10^{-7}	1.17×10^{-7}
395	2.5316	1.11 "	-
397	2.5188	1.11 "	-
399	2.5062	1.11 "	-
401	2.4937	1.11 "	-
403	2.4814	1.11 "	1.17×10^{-7}
405	2.4691	1.11 "	-
407	2.4570	1.14 "	-
409	2.4449	1.14 "	1.20×10^{-7}
411	2.4331	1.11 "	1.17 "
413	2.4213	1.14 "	1.17 "
415	2.4096	1.14 "	1.26 "
417	2.3981	1.11 "	1.37 "
419	2.3866	1.11 "	1.46 "
421	2.3753	1.20 "	2.28 "
423	2.3641	1.24 "	5.71×10^{-6}
425	2.3529	1.28 "	6.57×10^{-5}
427	2.3419	1.43 "	1.40×10^{-4}
429	2.3310	1.43 "	1.80 "
431	2.3202	1.54 "	1.97 "
433	2.3095	1.60 "	2.14 "
435	2.2989	1.91 "	2.37 "
437	2.2883	3.71 "	2.57 "
439	2.2779	6.86 "	2.86 "
441	2.2676	3.26×10^{-6}	3.14 "
443	2.2573	4.57×10^{-5}	3.43 "

T($^\circ$K)	1000/T($^\circ$K)$^{-1}$	Conductivity (Ohm-cm)$^{-1}$	
		Heating	Cooling
445	2 2472	—	3.71x10^{-4}
447	2.2371	1 71x10^{-4}	4.00 "
449	2.2272	2 26 "	4.57 "
451	2.2173	2.71 "	4.57 "
453	2 2075	3 03 "	2 28 "
455	2.1978	3 43 "	8.57x10^{-5}
457	2.1882	3 71 "	3.71 "
459	2 1786	4.00 "	1.43 "
461	2.1692	4 28 "	5.43x10^{-6}
463	2.1598	4.57 "	2.66 "
465	2.1505	4.86 "	2.14 "
467	2.1413	5.14 "	2.08 "
469	2.1322	5.71 "	2.11 "
471	2 1231	6.00 "	2.23 "
473	2.1142	6.57 "	2.40 "
475	2 1053	6.86 "	2.57 "
477	2 0964	7.43 "	2.74 "
479	2 0877	8.00 "	2.86 "
481	2 0790	8.57 "	3.14 "
483	2 0704	9.14	3.43 "
485	2 0619	9.43 "	3.71 "
487	2 0534	9.43 "	4.00 "
489	2 0450	8.57 "	4.28 "
491	2 0367	6.57"	4.57 "
493	2.0284	3.71 "	4.86 "
495	2.0202	1.71 "	5.43 "

$T(^{o}K)$	$1000/T(^{o}K)^{-1}$	Conductivity $(Ohm-cm)^{-1}$	
497	2.0121	1.08×10^{-4}	5.71×10^{-6}
499	2.0040	7.71×10^{-5}	6.00 "
501	1.9960	5.43 "	6.57 "
503	1.9881	3.43 "	6.86 "
505	1.9802	2.00 "	7.43 "
507	1.9724	1.37 "	8.00 "
509	1.9646	1.11 "	8.57 "
511	1.9569	1.03 "	9.14 "
513	1.9493	1.03 "	9.71 "
515	1.9417	1.06 "	1.03×10^{-5}
517	1.9342	1.06 "	1.08 "
519	1.9268	1.08 "	1.14 "
521	1.9194	1.14 "	1.23 "
523	1.9120	1.20 "	1.31 "
525	1.9048	1.26 "	1.43 "
527	1.8975	1.34 "	1.54 "
529	1.8904	1.40 "	1.63 "
531	1.8832	1.48 "	1.74 "
533	1.8762	1.60 "	1.86 "
535	1.8691	1.68 "	2.08 "
537	1.8622	1.80 "	2.26 "
539	1.8553	1.91 "	2.43 "
541	1.8484	2.03 "	2.57 "
543	1.8416	2.17 "	4.57 "
545	1.8349	2.31 "	8.00 "
547	1.8282	2.43 "	1.11×10^{-4}

T($^\circ$K)	1000/T($^\circ$K)$^{-1}$	Conductivity (Ohm-cm)$^{-1}$	
		Heating	Cooling
549	1.8215	2 57x10^{-5}	2.00x10^{-4}
551	1.8149	2.77 "	3.43 "
553	1.8083	2 97 "	7.14 "
555	1.8018	3.43 "	1.26x10^{-3}
557	1.7953	3.71 "	1.66 "
559	1 7889	4.28 "	–
561	1 7825	4 86 "	2.20x10^{-3}
563	1 7762	6.86 "	2.28 "
565	1 7699	8.28 "	4.28 "
567	1.7637	9.43 "	6 00 "
569	1 7575	1 08x10^{-4}	1.0Cx10^{-2}
571	1.7513	1.28 "	1.34 "
573	1.7452	1.60 "	1.80 "
575	1 7391	2.08 "	2.11 "
577	1 7331	3.26 "	2.57 "
579	1.7271	5.71 "	2.86 "
581	1 7212	1 08x10^{-3}	3.14 "
583	1.7153	1.40 "	3.14 "
585	1.7094	1 88 "	3.14 "
587	1.7036	4.28 "	3.14 "
589	1 6978	8.28 "	–
591	1.6920	2.40x10^{-2}	–
593	1.6863	–	3.43x10^{-2}
595	1.6807	3 71x10^{-2}	3.43 "
597	1.6750	3 43 "	3.43 "
599	1.6694	3.43 "	3.43 "
601	1.6639	3.43 "	3.43 "
603	1.6584	3.43 "	3.43 "

TABLE D.8 Conductivity data on $K_{0.04}Rb_{0.96}NO_3$

$T(°K)$	$1000/T$ $(°K)^{-1}$	Conductivity $(Ohm-cm)^{-1}$	
		Heating	Cooling
393	2 5445	1.26×10^{-7}	1.40×10^{-7}
395	2.5316	1.26 "	1.43 "
397	2.5188	1 23 "	1.46 "
399	2.5062	1.26 "	1.51 "
401	2.4937	1.26 "	1.57 "
403	2.4814	1.28 "	1.94 "
405	2.4691	1.26 "	2.40 "
407	2.4570	1.26 "	2.66 "
409	2.4449	1.28 "	2.86 "
411	2.4331	1.34 "	3.14 "
413	2 4213	1.31 "	3.43 "
415	2 4096	1.28 "	3.71 "
417	2.3981	1.28 "	4.57 "
419	2.3866	1.28 "	8.86 "
421	2.3753	1.37 "	2.28×10^{-6}
423	2.3641	1.43 "	4.00×10^{-5}
425	2.3529	1.48 "	7.43 "
427	2.3419	1.51 "	7.14 "
429	2.3310	1.57 "	4.83 "
431	2.3202	1.68 "	2.80 "
433	2 3095	1.86 "	1.34 "
435	2 2989	2.17 "	6.57×10^{-6}
437	2.2883	4 00 "	2.54 "
439	2.2779	$4 57 \times 10^{-6}$	1.77 "
441	2.2676	2.60×10^{-5}	1.48 "
443	2.2573	8.0 "	1.34 "

T(°K)	1000/T(°K)$^{-1}$	Conductivity (Ohm-cm)$^{-1}$	
		Heating	Cooling
445	2.2472	1.40×10^{-4}	1.28×10^{-6}
447	2.2371	1.63 "	1.26 "
449	2.2272	1.86 "	1.26 "
451	2.2173	2.06 "	1.28 "
453	2.2075	2.23 "	1.31 "
455	2.1978	2.40 "	1.37 "
457	2.1882	2.57 "	1.46 "
459	2.1786	2.68 "	1.54 "
461	2.1692	2.80 "	1.66 "
463	2.1598	2.86 "	1.80 "
465	2.1505	2.83 "	1.94 "
467	2.1413	2.54 "	2.08 "
469	2.1322	2.40 "	2.20 "
471	2.1231	2.37 "	2.37 "
473	2.1142	2.31 "	2.57 "
475	2.1053	2.28 "	2.77 "
477	2.0964	2.23 "	3.00 "
479	2.0877	2.11 "	3.14 "
481	2.0790	1.91 "	3.43 "
483	2.0704	1.77 "	3.71 "
485	2.0619	1.60 "	4.00 "
487	2.0534	1.46 "	4.57 "
489	2.0450	1.28 "	4.86 "
491	2.0367	1.06 "	5.14 "
493	2.0284	8.86×10^{-5}	5.43 "
495	2.0202	6.86 "	5.71 "

T($^{\circ}$K)	1000/T($^{\circ}$K)$^{-1}$	Conductivity (Ohm-cm)$^{-1}$	
		Heating	Cooling
497	2.0121	5.43×10^{-5}	6.0×10^{-6}
499	2.0040	3.71 "	6.28 "
501	1.9960	2.57 "	6.86 "
503	1.9881	1.80 "	7.43 "
505	1.9802	1.43 "	7.71 "
507	1.9724	1.20 "	8.57 "
509	1.9646	1.11 "	9.14 "
511	1.9569	1.08 "	1.00×10^{-5}
513	1.9493	1.08 "	1.06 "
515	1.9417	1.11 "	1.14 "
517	1.9342	1.14 "	1.23 "
519	1.9268	1.17 "	1.31 "
521	1.9194	1.20 "	1.37 "
523	1.9120	1.26 "	1.48 "
525	1.9048	1.31 "	1.57 "
527	1.8975	1.37 "	1.68 "
529	1.8904	1.43 "	2.00 "
531	1.8832	1.48 "	2.26 "
533	1.8762	1.54 "	2.43 "
535	1.8691	1.63 "	2.63 "
537	1.8622	1.71 "	3.14 "
539	1.8553	1.83 "	4.00 "
541	1.8484	1.94 "	5.43 "
543	1.8416	2.06 "	6.86 "
545	1.8349	2.17 "	9.43 "
547	1.8282	2.34 "	1.23×10^{-4}
549	1.8215	2.48 "	1.77 "

T(^{o}K)	1000/T(^{o}K)$^{-1}$	Conductivity (Ohm-cm)$^{-1}$	
		Heating	Cooling
551	1.8149	2.68×10^{-5}	3.71×10^{-4}
553	1.8083	2.96 "	6.57 "
555	1.8018	3.14 "	1.48×10^{-3}
557	1.7953	3.71 "	2.00 "
559	1.7889	4.28 "	–
561	1.7825	5.71 "	3.43×10^{-3}
563	1.7762	8.86 "	6.00 "
565	1.7699	1.11×10^{-4}	9.14 "
567	1.7637	1.31 "	1.23×10^{-2}
569	1.7575	1.51 "	1.57 "
571	1.7513	1.63 "	1.83 "
573	1.7452	2.00 "	1.97 "
575	1.7391	2.83 "	2.06 "
577	1.7331	4.28 "	2.23 "
579	1.7271	8.28	2.28 "
581	1.7212	4.00×10^{-3}	2.34 "
583	1.7153	6.00 "	2.31 "
585	1.7094	8.00 "	2.40 "
587	1.7036	1.17×10^{-2}	2.46 "
589	1.6978	2.03 "	2.54 "
591	1.6920	2.34 "	2.54 "
593	1.6863	2.71 "	2.57 "
595	1.6807	2.46 "	2.51 "
597	1.6750	2.57 "	2.63 "
599	1.6694	2.63 "	2.68 "
601	1.6639	2.66 "	2.74 "
603	1.6584	2.68	2.77 "

TABLE D.9   Conductivity data on $K_{0.05}Rb_{0.95}NO_3$

$T(^{o}K)$	$1000/T(^{o}K)^{-1}$	Conductivity $(Ohm-cm)^{-1}$	
		Heating	Cooling
393	2.5445	1.34×10^{-7}	3.71×10^{-7}
403	2.4814	1.66 "	3.43 "
407	2.4570	1.91 "	4.00 "
411	2.4331	2.11 "	4.57 "
413	2.4213	2.26	4.57 "
415	2.4096	2.43	5.14 "
417	2.3981	3.14 "	5.14 "
419	2.3866	3.43 "	5.71 "
421	2.3753	3.71 "	6.00 "
423	2.3641	4.28 "	7.71 "
425	2.3529	4.57 "	2.00×10^{-6}
427	2.3419	4.86 "	3.43 "
429	2.3310	5.43 "	1.28 "
431	2.3202	6.57 "	7.71×10^{-7}
433	2.3095	1.14×10^{-6}	7.43
435	2.2989	8.57 "	7.43 "
437	2.2883	4.00×10^{-5}	7.43 "
439	2.2779	6.80 "	7.71 "
441	2.2676	1.03×10^{-4}	7.71 "
443	2.2573	1.34 "	8.00 "

$T(^\circ K)$	$1000/T(^\circ K)^{-1}$	Conductivity $(Ohm\text{-}cm)^{-1}$	
		Heating	Cooling
445	2.2472	1.54×10^{-4}	8.43×10^{-7}
447	2.2371	1.63 "	8.57 "
449	2.2272	1.66 "	8.86 "
451	2.2173	1.71 "	9.71 "
453	2.2075	1.74 "	1.03×10^{-6}
455	2.1978	1.75 "	1.11 "
457	2.1882	1.78 "	1.20 "
459	2.1786	1.74 "	1.31 "
461	2.1692	1.72 "	1.43 "
463	2.1598	1.52 "	1.51 "
465	2.1505	1.59 "	1.63 "
467	2.1413	1.53 "	1.74 "
469	2.1322	1.41 "	1.88 "
471	2.1231	1.27 "	2.03 "
473	2.1142	1.14 "	2.20 "
475	2.1053	1.03 "	2.37 "
477	2.0964	8.86×10^{-5}	2.54 "
479	2.0877	7.83 "	2.77 "
481	2.0790	6.28 "	3.14 "
483	2.0704	4.00 "	3.43 "
485	2.0619	2.86 "	3.71 "
487	2.0534	2.00 "	3.71 "
489	2.0450	1.66 "	4.00 "
491	2.0367	1.26 "	4.26 "
493	2.0284	8.86×10^{-6}	4.57 "
495	2.0202	7.71 "	5.14 "

T($^{\circ}$K)	1000/T($^{\circ}$K)$^{-1}$	Conductivity (Ohm-cm)$^{-1}$	
		Heating	Cooling
497	2.0121	7.14×10^{-6}	5.43×10^{-6}
499	2.0040	6.86 "	5.71 "
501	1.9960	7.14 "	6.00 "
503	1.9881	7.20 "	6.57"
505	1.9802	7.34 "	7.43 "
507	1.9724	7.51 "	8.00 "
509	1.9646	7.63 "	8.57 "
511	1.9569	7.91 "	8.86 "
513	1.9493	8.20 "	9.71 "
515	1.9417	8.51 "	1.06×10^{-5}
517	1.9342	8.83 "	1.11 "
519	1.9268	9.20 "	1.20 "
521	1.9194	9.60 "	1.28 "
523	1.9120	1.01×10^{-5}	1.37 "
525	1.9048	1.06 "	1.48 "
527	1.8975	1.13 "	1.60 "
529	1.8904	1.19"	1.74 "
531	1.8832	1.23 "	1.38 "
533	1.8762	1.32 "	2.06 "
535	1.8691	1.41 "	2.20 "
537	1.8622	1.47 "	2.57 "
539	1.8553	1.55 "	3.43 "
541	1.8484	1.64 "	4.28 "
543	1.8416	1.75 "	5.43 "
545	1.8349	1.85 "	7.43 "
547	1.8282	1.98 "	1.03×10^{-4}
549	1.8215	2.10 "	1.57 "

T($^{\circ}$K)	1000/T($^{\circ}$K)$^{-1}$	Conductivity (Ohm-cm)$^{-1}$	
		Heating	Cooling
551	1.8149	2.28×10^{-5}	2.57×10^{-4}
553	1.8083	2.86 "	3.43 "
555	1.8018	3.71 "	4.00 "
557	1.7953	4.80 "	4.28 "
559	1.7889	5.37 "	4.57 "
561	1.7825	5.83 "	5.14 "
563	1.7762	6.66 "	6.57 "
565	1.7699	5.86 "	1.37×10^{-3}
567	1.7637	7.34 "	2.43 "
569	1.7575	1.08×10^{-4}	–
571	1.7513	1.45 "	2.73×10^{-1}
573	1.7452	3.08	2.76 "
575	1.7391	5.14 "	2.30 "
577	1.7331	8.00 "	2.30 "
579	1.7271	1.48×10^{-3}	2.34 "
581	1.7212	3.14×10^{-1}	2.40 "
583	1.7153	3.11 "	2.39 "
585	1.7094	1.11 "	2.40 "
587	1.7036	1.14 "	2.40 "
589	1.6978	1.14 "	2.40 "
591	1.6920	1.17 "	2.40 "
593	1.6863	2.43 "	2.47 "
595	1.6807	2.43 "	2.46 "
597	1.6750	2.43 "	2.45 "
599	1.6694	2.43 "	2.44 "
601	1.6639	2.43 "	2.44 "
603	1.6584	2.43 "	2.43 "

Table D.10 Conductivity data on $K_{0.07}Rb_{0.93}NO_3$.

$T(^\circ K)$	$1000/T(^\circ K)^{-1}$	Conductivity $(Ohm-cm)^{-1}$	
		Heating	Cooling
393	2.5445	1.94×10^{-7}	2.34×10^{-7}
395	2.5316	2.06 "	2.48 "
397	2.5188	2.11 "	2.54 "
399	2.5062	2.83 "	2.77 "
401	2.4927	3.14 "	2.83 "
403	2.4814	3.71 "	2.88 "
405	2.4691	4.00 "	2.94 "
407	2.4570	4.57 "	2.97 "
409	2.4449	5.14 "	3.03 "
411	2.4331	5.43 "	2.94 "
413	2.4213	6.00 "	2.94 "
415	2.4096	6.86 "	3.14 "
417	2.3981	7.71 "	3.14 "
419	2.3866	8.57 "	3.71 "
421	2.3753	9.71 "	4.57 "
423	2.3641	1.08×10^{-6}	4.86 "
425	2.3529	1.26 "	5.14 "
427	2.3419	1.40 "	5.43 "
429	2.3310	1.60 "	5.71 "
431	2.3202	1.83 "	6.00 "
433	2.3095	2.51 "	6.57 "
435	2.2989	3.71 "	6.86 "
437	2.2883	1.14×10^{-5}	7.43 "
439	2.2779	2.74 "	8.00 "
441	2.2676	5.71 "	8.28 "
443	2.2573	1.14×10^{-4}	8.86 "

$T(^\circ K)$	$1000/T(^\circ K)^{-1}$	Conductivity $(Ohm-cm)^{-1}$	
		Heating	Cooling
445	2.2472	1.34×10^{-4}	9.43×10^{-7}
447	2.2371	1.43 "	1.03×10^{-6}
449	2.2272	1.48 "	1.11 "
451	2.2173	1.54 "	1.23 "
453	2.2075	1.57 "	1.28 "
455	2.1978	1.57 "	1.43 "
457	2.1882	1.57 "	1.51 "
459	2.1786	1.54 "	1.63 "
461	2.k692	1.51 "	1.74 "
463	2.1598	1.43 "	1.91 "
465	2.1505	1.37 "	2.06 "
467	2.1413	1.26 "	2.20 "
469	2.1322	1.20 "	2.40 "
471	2.1231	1.11 "	2.60 "
473	2.1142	1.00 "	2.74 "
475	2.1053	8.86×10^{-5}	3.03 "
477	2.0964	8.00 "	3.14 "
479	2.0877	6.86 "	3.43 "
481	2.0790	5.71 "	3.71 "
483	2.0704	4.86 "	4.00 "
485	2.0619	4.00 "	4.28 "
487	2.0534	3.14 "	4.86 "
489	2.0450	2.28 "	5.14 "
491	2.0367	1.74 "	5.43 "
493	2.0284	1.40 "	5.71 "
495	2.0202	1.11 "	6.28 "

T(^{o}K)	1000/T(^{o}K)$^{-1}$	Conductivity (Ohm-cm)$^{-1}$	
		Heating	Cooling
497	2.0121	9.71×10^{-6}	6.57×10^{-6}
499	2.0040	9.14 "	7.14 "
501	1.9960	9.14 "	7.71 "
503	1.9881	9.43 "	8.28 "
505	1.9802	9.71 "	8.86 "
507	1.9724	1.03×10^{-5}	9.43 "
509	1.9646	1.08 "	1.03×10^{-5}
511	1.9569	1.14 "	1.08 "
513	1.9493	1.20 "	1.20 "
515	1.9417	1.28 "	1.26 "
517	1.9342	1.34 "	1.37 "
519	1.9268	1.40 "	1.46 "
521	1.9194	1.46 "	1.54 "
523	1.9120	1.57 "	1.68 "
525	1.9048	1.66 "	1.83 "
527	1.8975	1.77 "	2.00 "
529	1.8904	1.86 "	2.14 "
531	1.8832	1.97 "	2.3k "
533	1.8762	2.11 "	2.60 "
535	1.8691	2.23 "	2.94 "
537	1.8622	2.37 "	3.43 "
539	1.8553	2.48 "	4.57 "
541	k.8484	2.66 "	7.43 "
543	1.3416	2.88 "	9.71 "
545	1.8349	3.08 "	1.28×10^{-4}
547	1.8282	3.43 "	1.68 "
549	1.8215	3.43 "	2.57 "

T($^\circ$K)	1000/T ($^\circ$K)$^{-1}$	Conductivity (Ohm-cm)$^{-1}$	
		Heating	Cooling
551	1.8149	3.71×10^{-5}	3.43×10^{-4}
553	1.8083	4.23 "	6.00 "
555	1.8018	4 86 "	1.23×10^{-3}
557	1.7953	7.14 "	2.57 "
559	1.7889	1.51×10^{-4}	4.00 "
561	1.7825	2.06 "	6.28 "
563	1.7762	2.40 "	8.86 "
565	1.7699	2.54 "	1.31×10^{-2}
567	1 7637	2.54 "	1.77 "
569	1.7575	2.68 "	2.17 "
571	1.7513	4.57 "	2.40 "
573	1.7452	8.28 "	2.63 "
575	1 7391	1.00×10^{-3}	2.74 "
577	1.7331	2.28 "	2.86 "
579	1 7271	8.00 "	2.86 "
581	1.7212	1.74×10^{-2}	2.86 "
583	1.7153	2.28 "	2.86 "
585	1.7094	–	2.86 "
587	1.7036	3.03×10^{-2}	2.86 "
589	1.6978	2.86 "	–
591	1.6920	2.86 "	–
593	1.6863	2.86 "	3.14×10^{-2}
595	1.6807	2.86 "	3.14 "
597	1 6750	3.14 "	3.14 "
599	1.6694	3.14 "	3.14 "
601	1.6639	3.14 "	3.14 "
603	1.6584	3.14 "	3.14 "

E. DTA data

TABLE : E1 Thermal hysteresis data derived from DTA curves (figs. 4.5 or 4.6 at $x = 0$) of $RbNO_3$ for IV ⇌ III and III ⇌ II transformations.

IV ⇌ III				III ⇌ II			
Heating		Cooling		Heating		Cooling	
Temperature (oC)	Fraction transformed	Temperature (°C)	Fraction transformed	Temperature(°C)	Fraction transformed	Temperature(°C)	Fraction transformed
160.0	0.00	158.0	1.00	220.0	0.00	213.5	1.0
162.0	0.00	156.5	0.93	222.5	0.07	212.0	0.91
165.0	0.15	156.0	0.83	223.5	0.20	211.5	0.83
165.5	0.25	156.0	0.73	225.5	0.32	211.0	0.68
167.0	0.46	156.0	0.63	226.0	0.44	210.5	0.52
168.0	0.62	156.0	0.48	228.0	0.67	210.0	0.36
169.0	0.78	156.0	0.33	230.0	0.91	209.5	0.21
170.0	0.90	156.0	0.18	231.5	1.00	208.0	0.12
170.5	1.00	155.5	0.07			207.0	0.05
		154.0	0.03			204.0	0.00
		152.0	0.00				

TABLE E2 : Thermal hysteresis data derived from DTA curves (fig.4.5 at x = 0.05) of $Cs_{0.05}Rb_{0.95}NO_3$ system for IV ⇌ III and III ⇌ II transformations.

| IV ⇌ III | | | | III ⇌ II | | | |
| Heating | | Cooling | | Heating | | Cooling | |
Temperature($^\circ$C)	Fraction transformed	Temperature($^\circ$C)	Fraction transformed	Temperature($^\circ$C)	Fraction transformed	Temperature($^\circ$C)	Fraction transformed
158.0	0.00	155.0	1.00	240.0	0.00	229.5	1.00
160.0	0.015	154.5	0.92	244.0	0.06	228.0	0.88
161.0	0.10	154.5	0.83	244.5	0.15	228.0	0.73
161.5	0.20	154.5	0.70	245.5	0.31	227.5	0.57
162.5	0.30	154.0	0.55	246.0	0.49	227.0	0.41
164.0	0.50	153.5	0.42	247.0	0.64	226.0	0.25
164.0	0.60	153.0	0.28	248.0	0.82	225.0	0.10
164.5	0.745	152.0	0.15	249.5	1.00	220.0	0.00
165.5	0.84	150.0	0.05				
167.0	0.935	144.0	0.00				
169.5	1.00						

TABLE E3. Thermal hysteresis data derived from DTA curves (fig 4.5, at x = 0.10) of $Cs_{0.10}Rb_{0.90}NO_3$ system for IV $\rightleftharpoons$ III and III $\rightleftharpoons$ II transformations.

IV $\rightleftharpoons$ III				III $\rightleftharpoons$ II			
Heating		Cooling		Heating		Cooling	
Tempera-ture($^{\circ}$C)	Fraction transformed	Tempera-ture($^{\circ}$C)	Fraction transformed	Tempera-ture($^{\circ}$C)	Fraction transformed	Tempera-ture($^{\circ}$C)	Fraction transformed
154.0	0.00	152.0	1.00	258.0	0.00	244.0	1.00
157.5	0.02	150.5	0.95	260.0	0.01	242.0	0.92
159.0	0.05	150.0	0.87	261.5	0.07	242.0	0.79
160.0	0.14	150 0	0.74	262.0	0.14	241.0	0.65
161.0	0.27	149.5	0.62	262.5	0.27	240.0	0.44
162.0	0.35	149.0	0.46	263.5	0.41	238.0	0.24
162.5	0.44	148.0	0.34	264.0	0.54	236.0	0.10
163.0	0.53	147.0	0.22	265.5	0.68	233.5	0.03
163.5	0.62	145.5	0.14	267.0	0.82	230.0	0.00
164.0	0.71	144.5	0.06	269.0	0.93		
165.0	0.80	143.0	0.03	270.0	1.00		
165 5	0.88	138 0	0.00				
166.5	1.00						

F. Dilatometric data

TABLE F.1 – Dilatometric data on thermal expansion of $RbNO_3$. Length of rod specimen (l) = 1.5 cm

HEATING				COOLING			
Temperature(°C)	$\frac{\Delta l}{l} \times 10^3$	Temperature(°C)	$\frac{\Delta l}{l} \times 10^3$	Temperature(°C)	$\frac{\Delta l}{l} \times 10^3$	Temperature(°C)	$\frac{\Delta l}{l} \times 10^3$
81	2.93	211	30.58	275	76.78	199	56.76
91	3.81	213	36.30	273	76.71	197	52.36
101	4.75	215	42.90	271	76.56	195	47.52
111	5.65	217	50.16	269	76.34	193	41.14
121	6.53	219	57.49	267	75.90	191	39.60
131	7.55	221	63.14	265	75.24	189	39.38
141	8.65	223	65.78	263	74.80	181	38.13
151	9.75	225	66.66	261	74.14	171	36.30
153	10.34	227	67.10	259	73.77	161	34.54
155	11.22	233	67.98	257	73.48	155	33.29
157	12.98	239	68.71	255	72.75	153	32.96
159	15.55	245	69.45	249	71.72	151	31.90
161	18.33	251	70.18	243	71.06	149	30.36
163	19.80	257	70.77	237	70.40	147	28.45
165	20.24	263	71.65	231	69.89	145	27.35
167	20.68	265	72.53	225	69.37	141	26.55
175	21.93	267	73.55	219	68.79	131	25.52
185	23.54	269	74.21	213	68.20	121	24.49
195	25.08	271	74.95	207	67.61	111	23.61
205	26.69	273	76.12	205	67.39	101	22.73
207	27.06	275	76.56	203	64.97	91	21.85
209	27.65	277	76.78	201	61.45	81	20.90

TABLE F.2 - Dilatometric data on thermal expansion of $Cs_{0.05}Rb_{0.95}NO_3$
Length of rod specimen (ℓ) = 1.5 cm

	HEATING				COOLING		
Temperature ($^\circ$C)	$\frac{\Delta \ell}{\ell} \times 10^3$	Temperature ($^\circ$C)	$\frac{\Delta \ell}{\ell} \times 10^3$	Temperature ($^\circ$C)	$\frac{\Delta \ell}{\ell} \times 10^3$	Temperature ($^\circ$C)	$\frac{\Delta \ell}{\ell} \times 10^3$
82	3.96	206	23.83	268	69.37	206	26.11
92	4.91	216	25.37	264	69.15	200	24.49
102	5.87	226	26.77	260	68.79	190	23.03
112	6.89	230	27.57	256	68.20	180	21.41
122	7.77	232	28.75	252	67.39	170	19.95
132	8.80	234	31.60	248	66.00	160	18.43
142	9.83	236	38.13	244	64.83	152	17.30
152	10.85	238	44.15	240	64.09	150	16.72
154	11.29	240	50.60	236	63.36	148	15.62
156	12.32	242	55.00	232	62.33	146	13.20
158	13.93	244	57.49	228	60.50	144	12.03
160	15.40	246	59.25	226	59.11	142	11.66
162	17.31	250	61.60	224	57.20	140	11.29
164	17.82	254	63.21	222	54.56	130	10.34
166	18.11	258	65.19	220	51.33	122	9.61
176	19.51	262	67 03	218	47.23	112	8.73
186	20.90	266	68.49	216	41.65	102	7.99
196	22.29	270	69.30	214	35.79	92	7.19
				212	29.92	82	6.45
				210	26.55		

TABLE F.3 Dilatometric data on thermal expansion of $Cs_{0.10}Rb_{0.90}NO_3$.
Length of rod specimen (l) = 1.3 cm.

HEATING				COOLING			
Temperature (°C)	$\frac{\Delta l}{l} \times 10^3$	Temperature (°C)	$\frac{\Delta l}{l} \times 10^3$	Temperature (°C)	$\frac{\Delta l}{l} \times 10^3$	Temperature (°C)	$\frac{\Delta l}{l} \times 10^3$
80.75	2.66	184.75	21.78	260.75	67.10	222.75	24.64
90.75	3 63	194.75	23.54	256.75	66.33	212.75	22.51
100.75	4.49	204.75	25.12	254.75	65.78	202.75	20.81
110.75	5.32	214 75	26.58	252.75	64.46	192.75	18.92
120 75	6.16	224 75	28.16	250.75	63.47	182.75	17.27
130.75	7.19	234.75	29.92	248.75	61.82	172.75	15.66
140.75	8.36	244.75	31.46	246.75	59.84	162.75	14.08
144.75	8.71	246.75	32.12	244.75	57.42	150.75	12.32
148.75	9 24	248 75	34.32	242.75	55.00	146.75	10.91
150.75	12.10	250.75	43.67	240.75	52.36	144.75	9.90
152.75	12.87	252.75	47.39	238.75	49.06	142.75	7.92
154.75	14.89	254.75	48.59	236.75	44.51	140.75	6.93
156.75	16.28	256.75	7.67	230.75	33.00	134.75	5.59
160.75	17.93	258.75	58.74	228.75	29.26	130.75	5.28
164.75	18.70	260.75	61.42	226.75	26.73	120.75	4.22
174.75	20.06	262.75	66.33	224.75	25.08	110.75	3.52

TABLE : F4 – Dilatometric data on thermal expansion of Cs$_{0.20}$Rb$_{0.80}$NO$_3$. Length of rod specimen (ℓ) = 1.3 cm

HEATING				COOLING			
Temperature(°C)	$\frac{\Delta l}{l} \times 10^3$	Temperature(°C)	$\frac{\Delta l}{l} \times 10^3$	Temperature(°C)	$\frac{\Delta l}{l} \times 10^3$	Temperature(°C)	$\frac{\Delta l}{l} \times 10^3$
80.5	3.96	156.5	18.70	250.5	31.68	142.5	13.86
90.5	4.91	162.5	19.80	246.5	31.13	140.5	13.53
100.5	5.94	172.5	21.67	236.5	29.48	136.5	12.87
110.5	6.93	182.5	22.88	226.5	27.59	134.5	12.01
120.5	7.92	192.5	24.02	216.5	25.74	132.5	11.22
130.5	9.06	202.5	25.30	206.5	23.98	126.5	8.62
134.5	9.68	212.5	26.73	196.5	22.02	122.5	7.88
140.5	11.00	222.5	27.94	186.5	20.68	110.5	6.27
142.5	12.01	232.5	29.48	176.5	18.92	100.5	5.28
146.5	15.22	242.5	30.47	166.5	17.42	90.5	4.40
148.5	17.09	252.5	31.90	156.5	15.91		
152.5	18.04			146.5	14.39		

TABLE : F.5 - Dilatometric data on thermal expansion of $K_{0.02}Rb_{0.98}NO_3$.
Length of rod specimen = 1.4 cm

HEATING				COOLING			
Temperature(°C)	$\frac{\Delta l}{l}\times10^3$	Temperature(°C)	$\frac{\Delta l}{l}\times10^3$	Temperature(°C)	$\frac{\Delta l}{l}\times10^3$	Temperature(°C)	$\frac{\Delta l}{l}\times10^3$
81	3.30	207	54.34	275	72.99	175	36.61
91	4.09	209	57.35	271	72.69	173	29.48
101	4.84	211	59.55	269	72.29	171	25.52
111	5.72	213	60.81	265	71.35	167	24.05
121	6.60	215	62.06	261	70.55	159	22.95
131	7.48	217	62.92	257	69.74	153	21.85
141	8.36	219	63.71	251	68.86	151	21.56
151	9.38	221	64.24	245	68.20	149	20.46
153	10.35	223	64.59	239	67.76	147	18.48
155	11.88	225	64.90	231	67.19	145	16.94
157	14.74	227	65.21	221	66.46	143	15.84
159	18.04	235	66.02	211	65.78	141	15.40
161	19.14	239	66.88	201	64.90	135	14.61
163	19.49	247	67.76	191	64.04	129	14.08
169	20.59	255	68.86	187	63.36	121	13.20
175	21.56	261	69.74	185	62.48	111	12.32
181	22.40	263	70.25	183	60.81	101	11.31
187	23.41	265	70.55	181	56.32	91	10.34
193	24.22	267	71.06	179	51.04	81	9.46
195	25.30	269	71.72	177	44.88		
197	26.40	273	72.75				
199	27.81	275	73.26				
201	29.06	277	73.48				
203	34.89	279	73.70				
205	42.68	281	73.70				

TABLE: F 6 – Dilatometric data on thermal expansion of $K_{0.04}Rb_{.96}NO_3$. Length of rod specimen (ℓ) = 1.4 cr.

	HEATING				COOLING		
Temperature(°C)	$\frac{\Delta\ell}{\ell} \times 10^3$	Temperature(°C)	$\frac{\Delta\ell}{\ell} \times 10^3$	Temperature(°C)	$\frac{\Delta\ell}{\ell} \times 10^3$	Temperature(°C)	$\frac{\Delta\ell}{\ell} \times 10^3$
81	4.09	191	33.79	273	61.29	171	44.79
91	5.06	193	35.35	271	61.16	169	44.00
101	5.94	195	36.96	269	60.94	167	42.90
111	6.91	197	38.72	267	60.72	165	41.01
121	7.92	199	40.55	265	60.50	163	38.28
131	8.95	201	42 46	263	60.06	161	34.32
141	9.97	203	44.44	261	59.40	159	28.91
151	11.15	205	46.35	259	58.52	157	24.86
153	11.95	207	48.71	257	57.66	155	20.46
155	13 35	209	50.75	255	57.05	153	16.50
157	16.65	211	52.36	253	56.65	151	12.76
159	17.91	213	53.68	249	55.70	149	10.21
161	18 11	215	54.34	243	54.56	147	7.55
163	18 85	217	54.91	237	53.46	145	5.65
165	19 36	219	55.31	231	52.65	143	4.25
167	19.95	221	55.46	225	51.92	141	3.52
169	20 59	225	55.88	219	51.06	139	3.15
171	21.56	231	56.54	213	50.29	133	2.20
173	22 66	237	57.05	207	49.59	127	1.56
175	23 98	243	57.66	201	48.95	121	1.01
177	24.86	249	58 17	195	48 25	111	0.00
179	25 96	255	58 74	189	47.61		
181	26 71	261	59.31	183	46.86		
183	27.94	267	60.10	177	46.05		
185	29.26	269	60.50				
187	30.80	271	60 81				
189	32.21	275	61 45				

TABLE : G2 X-ray data on thermal expansion of $K_{0.04}Rb_{0.96}NO_3$

Phase IV (Hexagonal)

Temperature (°C)	$a_{IV}(A°)$	$c_{IV}(A°)$	$a_{IV}/6$ (A°)	$c_{IV}/3$ (A°)	$V^{1/3}=(V_{IV}/9)^{1/3}$ A°
29	10.47	7.44	4.27	4.30	4.28
75	10.50	7.45	4.29	4.30	4.29
91	10.51	7.46	4.29	4.31	4.30
117	10.53	7.47	4.30	4.31	4.30
137	10.55	7.48	4.31	4.32	4.31
145	10.56	7.49	4.31	4.32	4.31
150	10.60	7.48	4.33	4.32	4.33
157	10.60	7.49	4.33	4.32	4.33

Phase III		Phase II (Hexagonal)					Phase I	
Temperature (°C)	$a_{III}(A°)$	Temperature (°C)	a_{II} (A°)	c_{II} (A°)	$a_{II}/4$ (A°)	$2'(V_{II/3})^{1/3}$	Temperature (°C)	a_I (A°)
165	4.362	192	5.56	10.72	4.68	4.38 4.58	293	7.32
167	4.357	205	5.57	10.76	4.69	4.39 4.59	296	7.33
173	4.366	256	5.55	10.82	4.67	4.42 4.58	300	7.33
185	4.373	262	5.54	10.85	4.66	4.43 4.58		
195	4.377	275	5.51	10.86	4.63	4.43 4.56		
208	4.383	283	5.48	10.93	4.61	4.46 4.56		
222	4.387	288	5.45	10.87	4.58	4.44 4.53		

TABLE : G3 X-ray data on thermal expansion of $Cs_{0.05}Rb_{0.95}NO_3$
Phase IV (Hexagonal)

Temperature(°C)	$a_{IV}(A^\circ)$	$c_{IV}(A^\circ)$	$a_{IV}/6$ (A°)	$c_{IV}/3$ (A°)	$V^{1/3}=(V_{IV}/9)^{1/3}$ A°
29	10.50	7.44	4.29	4.30	4.29
56	10.52	7.45	4.29	4.30	4.28
80	10.54	7.47	4.30	4.31	4.30
100	10.56	7.47	4.31	4.31	4.31
120	10.57	7.48	4.32	4.32	4.32
132	10.59	7.49	4.32	4.33	4.32
137	10.59	7.49	4.32	4.33	4.32
145	10.60	7.51	4.33	4.34	4.33
163	10.61	7.50	4.33	4.33	4.33

Phase III		Phase II (Hexagonal)						Phase I	
Temperature(°C)	$a_{III}(A^\circ)$	Temperature(°C)	$a_{II}(A^\circ)$	$c_{II}(A^\circ)$	$\dfrac{a_{II}}{4\ 2}$ A°	$\dfrac{c_{II}}{6}$ A°	$V^{1/3}=\dfrac{(V_{II}}{3})^{1/3}$ A°	Temperature(°C)	a_I (A°)
175	4.365	244	5.52	10.77	4.64	4.40	4.56	281.5	7.31
181	4.368	248	5.52	10.75	4.64	4.39	4.56	283.0	7.32
191	4.371	255	5.51	10.77	4.63	4.40	4.55		
211	4.384	263	5.49	10.79	4.62	4.41	4.55		
224	4.398								
233	4.393								
242	4.399								